2.3 Model results and evaluation

The previous sections have described a global chemical model of the troposphere, named CHASER (CHemical AGCM for Study of atmospheric Environment and Radiative forcing). In this section, results and evaluation of the model are presented. CHASER is basically driven on-line by climatological meteorology generated by the AGCM. For simulations of a specific time period, analyzed data of wind velocities, temperature, and specific humidity as from the ECMWF are optionally used as a constraint to the AGCM. For the simulation considered in this section, horizontal wind velocities and temperature (u, v, and T) in the model are moderately nudged to those from the ECMWF with a relaxation time of one week. The model in this study adopts the horizontal resolution of T42 (approximately 2.8° longitude$\times$2.8° latitude) , with 32 layers in the vertical from the surface to about 40 km altitude.

To validate the model capability to simulate the tropospheric photochemistry, it is necessary to evaluate the model results of ozone and species related to the ozone production and destruction (i.e., peroxy radicals, NO_x, CO, NMHCs, and reservoir species). Additionally, we need to carefully evaluate aldehydes and peroxyacetylnitrate (PAN) simulated by the model, to check the simplified chemical schemes for NMHCs adopted in the model (especially of the condensed isoprene and terpenes oxidation schemes, see section 2.2.1). The model was evaluated with several observational data sets. The data set of *Emmons et al.* [2000], a compilation made from the NASA Global Tropospheric Experiment (GTE) aircraft campaigns, is mainly used to evaluate the vertical distributions of calculated chemical species. This data set is also used for evaluation of the IMAGES model [*Müller and Brasseur*, 1995] and the MOZART model [*Hauglustaine et al.*, 1998; *Emmons et al.*, 2000]. Information about the NASA GTE observations is briefly summarized in Table 2.5. For comparison with the GTE data, model results of individual species are averaged over the regions and dates as listed in Table 2.5. It should be noted that data from campaign observations like the NASA GTE are not climatological, and that there may be some differences in meteorological conditions between the campaign observations and the climatological simulations by the model. In the evaluation of ozone and surface CO, climatological data [e.g., *Logan*, 1999; *Novelli et al.*, 1992, 1994] are used in addition to the NASA GTE data.

In this study, global tropospheric budget is calculated for some species such as CO and O_3. The budget is calculated for the region below the tropopause height determined from the vertical temperature gradient (-2 K/km) in the model. Each budget shows global annual averages of values (source and sink, etc.) calculated at each time step (typically 20 min in this study) in the model.

The results and evaluation of CO and NMHCs are presented in section 2.3.1, and reactive nitrogen oxides (NO_y) such as NO, HNO_3, and PAN in section 2.3.2. The results of HO_x and related species (formaldehyde CH_2O, acetone, and peroxides) are evaluated in section 2.3.3. Section 2.3.4 presents and evaluates the simulated ozone and the global tropospheric ozone budget calculated

Table 2.5. NASA GTE Campaign Regions and Dates

Campaign	Dates	Region Name	Latitudes	Longitudes
ABLE-3A	July 7 to Aug. 17, 1988			
		Alaska	55N-75N	190E-205E
ABLE-3B	July 6 to Aug. 15, 1990			
		Ontario	45N-60N	270E-280E
		US-E-Coast	35N-45N	280E-290E
		Labrador	50N-55N	300E-315E
PEM-WEST-A	Sept. 16 to Oct. 21, 1991			
		Hawaii	15N-35N	180E-210E
		Japan	25N-40N	135E-150E
		China-Coast	20N-30N	115E-130E
PEM-WEST-B	Feb. 7 to March 14, 1994			
		Japan	25N-40N	135E-150E
		China-Coast	20N-30N	115E-130E
		Philippine-Sea	5N-20N	135E-150E
PEM-Tropics-A	Aug. 15 to Oct. 5, 1996			
		Hawaii	10N-30N	190E-210E
		Chris.-Island	0-10N	200E-220E
		Tahiti	20S-0	200E-230E
		Fiji	30S-10S	170E-190E
		Easter-Island	40S-20S	240E-260E
PEM-Tropics-B	March 6 to April 18, 1999			
		Hawaii	10N-30N	190E-210E
		Chris.-Island	0-10N	200E-220E
		Tahiti	20S-0	200E-230E
		Fiji	30S-10S	170E-190E
		Easter-Island	40S-20S	240E-260E
TRACE-A	Sept. 21 to Oct. 26, 1992			
		S-Africa	25S-5S	15E-35E
		W-Africa-Coast	25S-5S	0E-10E
		S-Atlantic	20S-0	340E-350E
		E-Brazil	15S-5S	310E-320E
		E-Brazil-Coast	35S-25S	305E-320E
TRACE-P	March 3 to April 15, 2001			
		Japan	25N-40N	135E-150E
		China-Coast	20N-30N	115E-130E

Only campaigns and regions used for the evaluation are listed.

by the model. Simulation of sulfur species (SO_2 and sulfate) in this study is also summarized in section 2.3.5.

2.3.1 CO and NMHCs

Carbon monoxide (CO) and nonmethane hydrocarbons (NMHCs) play important roles in tropospheric chemistry, reacting with OH (controlling OH concentration) and significantly enhancing the ozone production. In this section, CO and NMHCs species (mainly of ethane and propane) simulated by CHASER are evaluated.

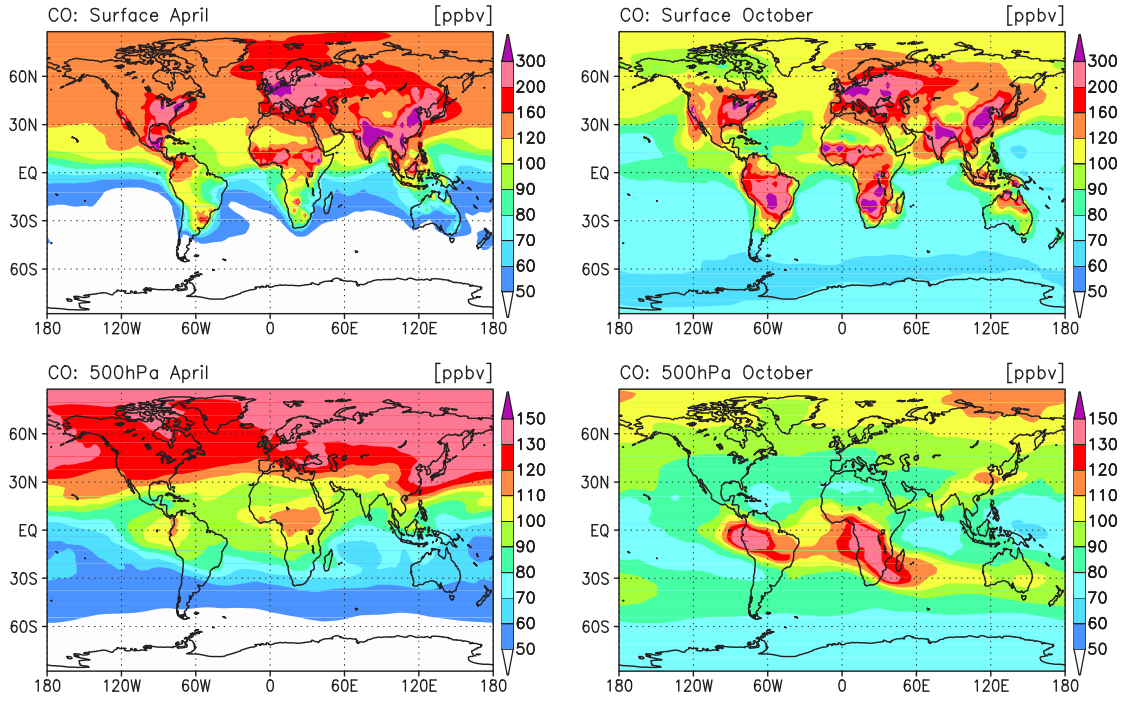

Figure 2.14. Calculated CO distributions (ppbv) at the surface and 500 hPa for April (left) and October (right).

CO

Figure 2.14 shows the calculated CO distributions at the surface and 500 hPa altitude for April and October. The CO mixing ratios calculated for April are generally higher than 100 ppbv in the northern hemisphere at both the surface and 500 hPa, with showing steep concentration gradients in the midlatitudes. At 500 hPa, two CO peaks are found in the tropics over South America and South Africa, reflecting vertical transport of CO from the surface and the CO production from oxidation of NMHCs species emitted by vegetation. The surface CO mixing ratios of 200-350 ppbv are predicted for both April and October in the industrial regions as the eastern United States, Europe, and eastern Asia. In October, high concentrations of CO ($\sim$300 ppbv) are also calculated at the surface in South America and South Africa, associated with biomass burning emissions considered in the model. The effect of biomass burning emissions on CO is clearly seen at 500 hPa. CO emitted or produced at the surface in South America and South Africa is vertically transported, resulting in high levels of CO (120-150 ppbv) at this altitude. Relatively high CO concentrations ($\sim$100 ppbv) are also extending over the South Atlantic, and over the Indian Ocean toward Australia like a plume.

Figure 2.15 compares the seasonal cycle of surface CO mixing ratios observed and calculated at several sites. The model generally well reproduces the observed CO seasonal variations. The seasonal variations of surface CO, characterized by spring-maximum, are associated with the seasonal

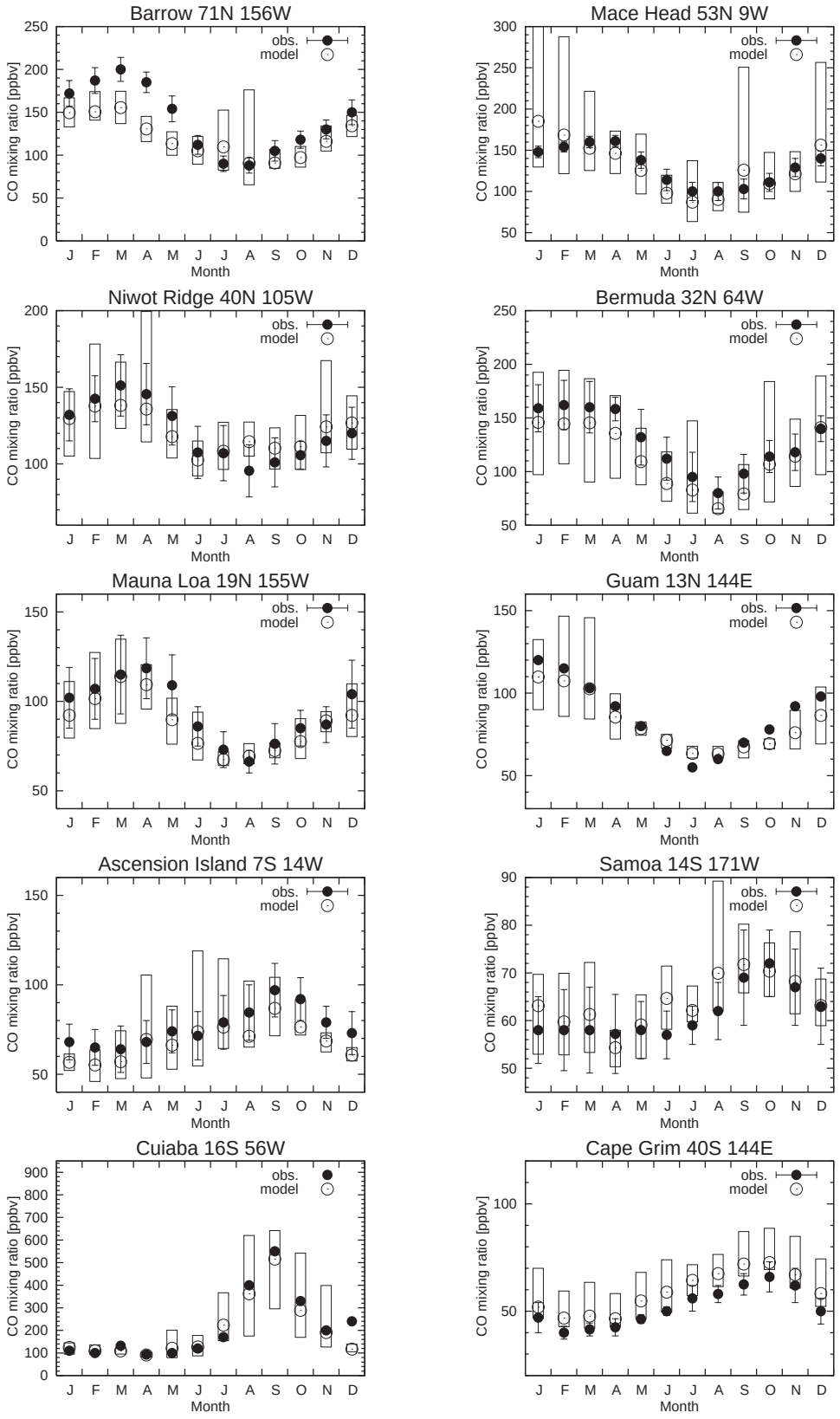

Figure 2.15. Observed (solid circles) and calculated (open circles) surface CO mixing ratios (ppbv) at several sites. Boxes indicate the range of the day-to-day variability calculated by the model. Measurements are taken from *Novelli et al.* [1992, 1994] and *Kirchhoff et al.* [1989] (for Cuiaba).

cycle of OH radical, transport of CO due to large-scale wind field and convection, and biomass burning (especially for the southern hemisphere). At Cuiaba located in the biomass burning region in South America, the seasonal cycle of surface CO has a peak in September (500-600 ppbv), much affected by biomass burning emissions. In the model, the seasonal variation of biomass burning emissions is imposed by using hot spot (fire distribution) data derived from satellites (see *Sudo et al.* [2002a] and section 2.2.2). The model appears to reproduce the observed seasonal cycle of surface CO at Cuiaba well, indicating the validity of the seasonal variation of biomass burning emissions considered in the model. A CO maximum in spring is seen at Ascension (over the tropical Atlantic) associated with biomass burning in South America and Africa, which is also captured by the model. The seasonal cycle of CO observed and simulated at Mauna Loa (spring peak) is much associated with the transport from eastern Asia (Asian outflow) as suggested by the simulation of atmospheric ^{222}Rn (see *Sudo et al.* [2002a] or Appendix 2A). At Barrow, the model underestimates the observed CO mixing ratios in spring, maybe indicating an overestimation of OH level or an underestimation of the CO surface emission in the high latitudes considered in the model.

A comparison between the calculated and the observed vertical profiles of CO over the GTE regions listed in Table 2.5 is shown in Figure 2.16. The observed CO vertical profiles are generally well reproduced by the model. In remote regions like Hawaii, Philippine-Sea, and Fiji, CO distributions are relatively uniform in the vertical with a range of 50-100 ppbv, whereas they are more variable in the source regions of biomass burning (E-Brazil and S-Africa) in the range of 100-200 ppbv. The model well captures the CO profiles observed over the Japan region during PEM-West-B, reproducing the CO increase in the lower troposphere (150-200 ppbv) due to industrial CO emissions. During TRACE-P (March to April), the observed CO profile in the China-Coast region shows increase below 5 km, owing to the combination of industrial CO emissions in China and CO transport from biomass burning in southeastern Asia (Thailand etc.). The model also calculates CO increases quite consistent with the observation in China-Coast. In the S-Atlantic region, CO levels are high in the free troposphere, especially in the upper troposphere ($>$ 8 km), much associated with transport from South Africa and South America as suggested by *Thompson et al.* [1996]. A CO plume from Africa toward South America is simulated well in 2-5 km over the W-Africa-Coast region. The model tends to overestimate CO levels in the tropical Pacific regions in some cases; Christmas-Island and Tahiti during PEM-Tropics-A. Although this may imply an underestimation of OH levels in the tropics, simulated OH concentrations in the tropical Pacific are quite consistent with the observations during the PEM-Tropics-B expedition (section 2.3.3).

Table 2.6 shows the global annual budget of tropospheric CO calculated by CHASER. The budget is calculated for the region below the tropopause height determined from the vertical temperature gradient (-2 K/km) in the model. CO has indirect sources from oxidation of CH_4 and NMHCs, as well as direct sources from surface emission (taken to be 1267 TgCO/yr in this simulation). The global chemical production of CO is estimated at 1514 TgCO/yr, showing a significant

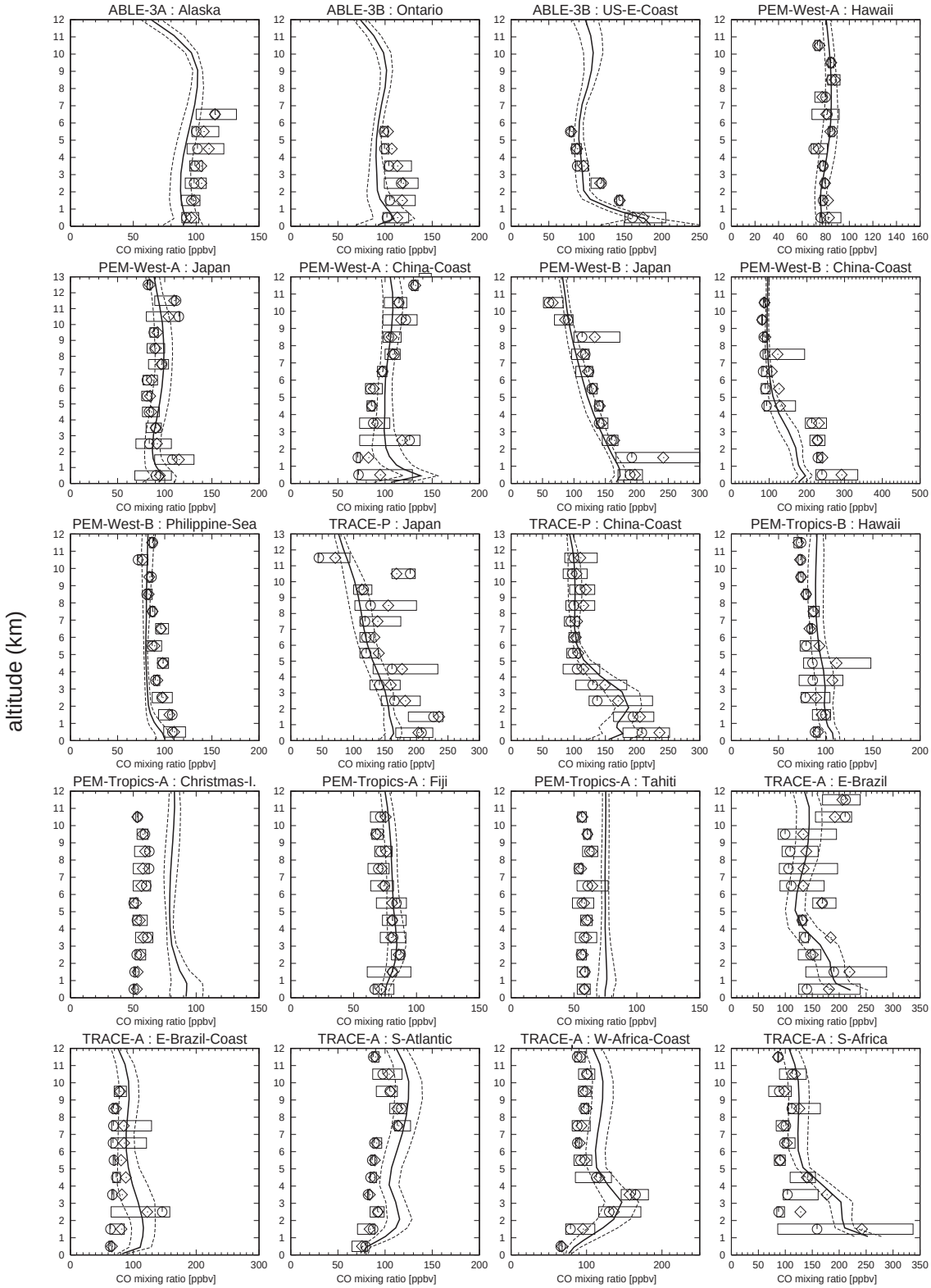

Figure 2.16. CO vertical profiles observed and calculated over the regions of GTE campaigns (listed in Table 2.5). Solid lines and dashed lines show temporal mean and $\pm 1\sigma$ of the model calculation, respectively. The observations show mean (diamonds), median (circles), and inner 50% of the data (boxes).

Table 2.6. Global Budget of Tropospheric CO Calculated by CHASER[a]

	Global	NH	SH
Sources	2781		
Surface emission	1267		
Chemical production	1514	844	670
$CH_2O + h\nu$	931	506	425
$CH_2O + OH$	397	243	154
Others [b]	186	95	91
Sinks	−2781		
STE [c]	−71		
Dry deposition	−139	−110	−29
Chemical loss (CO + OH)	−2571	−1582	−989
Chemical lifetime (days)	55	52	59
Burden (TgCO)	360	212	148

[a]Values (in TgCO/yr) are calculated for the region below the tropopause height in the model. NH, Northern Hemisphere; SH, Southern Hemisphere.
[b]Mainly from isoprene and terpenes oxidation.
[c]Stratosphere-Troposphere Exchange (CO flux to the stratosphere).

contribution from degradation of formaldehyde (CH_2O) and a contribution of ∼13% from degradation of NMHCs. Note that the CO production from CH_2O includes oxidation processes of both CH_4 and NMHCs. The reaction with OH radical is the only chemical sink for CO and is estimated at 2571 TgCO/yr in the global troposphere by the model. The chemical lifetime of CO due to this reaction is estimated at about 1.8 months in annual average by the model, with longer lifetime (59 days) in the southern hemisphere than that in the northern hemisphere (52 days), reflecting the distribution of OH radical. This estimated global lifetime of CO, 1.8 months, is slightly shorter than the value of 2.0 months estimated by *Müller and Brasseur* [1995]; *Hauglustaine et al.* [1998]. The global CO burden is calculated as 360 TgCO (59% in HN, 41% in SH), in good agreement with recent model studies [e.g., *Müller and Brasseur*, 1995; *Hauglustaine et al.*, 1998]. The distributions of net CO chemical production P(CO)-L(CO) calculated for April are shown in Figure 2.17. At the surface, high positive production rates of 6-10 ppbv/day are calculated in South America, South Africa, etc., associated with biogenic emissions of NMHCs as isoprene and terpenes. Relatively high CO production rates (1-2 ppbv/day) are also calculated at 200 hPa over South America and South Africa, reflecting convective transport of NMHCs species from the surface. In other regions, CO is slowly destroyed by OH at rates of −0.5 to −2 ppbv/day.

NMHCs

Distributions of NMHCs species are spatially and temporally variable compared to CO, because of their relatively short lifetimes (ranging from several hours to weeks). Figure 2.18 shows

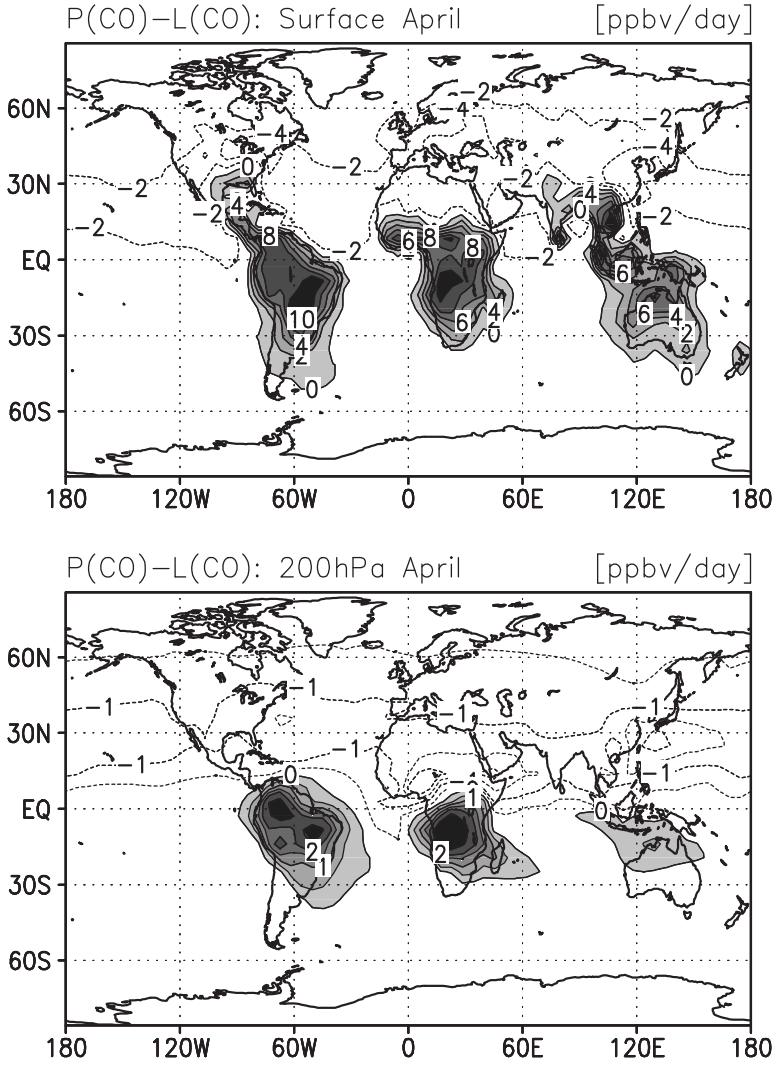

Figure 2.17. Net CO production rates (ppbv/day) calculated at the surface and 200 hPa altitude for April. Only positive areas are shaded.

the observed and the calculated seasonal cycles of surface C_2H_6 and C_3H_8. At the European site (Waldhof), the model captures the observed seasonal cycles of both C_2H_6 and C_3H_8. At Mauna Loa, the model appears to reproduce the observed C_2H_6 mixing ratios, though it slightly underestimates C_3H_8. The levels of C_2H_6 are much higher than C_3H_8 in Mauna Loa as C_2H_6 has a longer lifetime (2-3 weeks) compared to C_3H_8 (several days). The C_3H_8/C_2H_6 ratios are much less than 0.1 at Mauna Loa and 0.3-0.5 at Waldhof, indicating that the air at Mauna Loa is photochemically aged well (more than 5 days from a source region) [*Gregory et al.*, 1996] compared to Waldhof. At both sites, the calculated concentration and the temporal variability are high in winter and spring as well as CO. High temporal variabilities in winter-spring as seen in the calculated CO and NMHCs are also visible in the simulation of ^{222}Rn at the surface [*Sudo et al.*, 2002a].

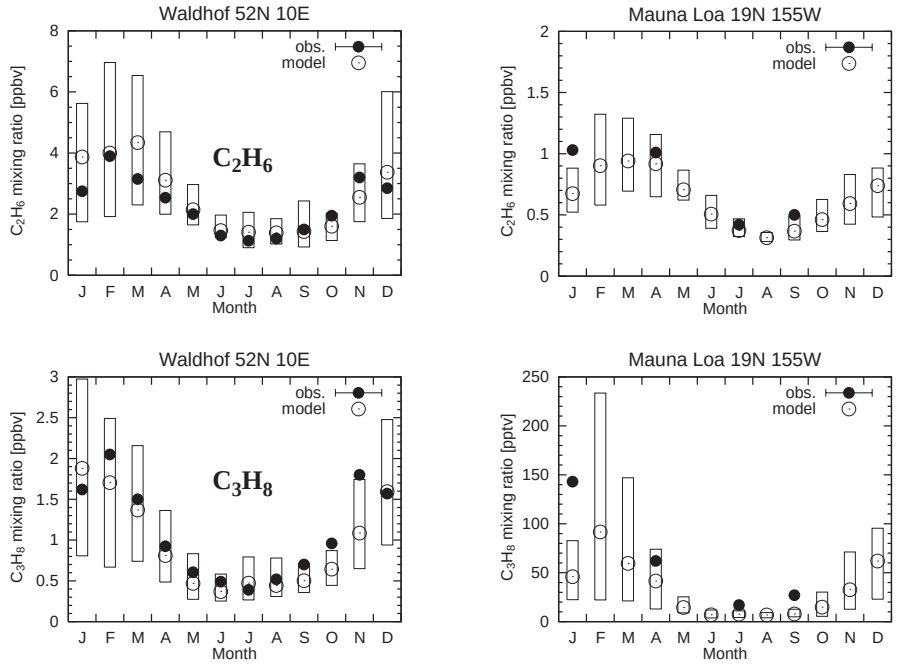

Figure 2.18. Observed (solid circles) and calculated (open circles) surface C_2H_6 (upper) and C_3H_8 (lower) mixing ratios (ppbv). Boxes indicate the range of the day-to-day variability calculated by the model. Measurements are taken from *Solberg et al.* [1996] and *Greenberg et al.* [1996] (for Mauna Loa).

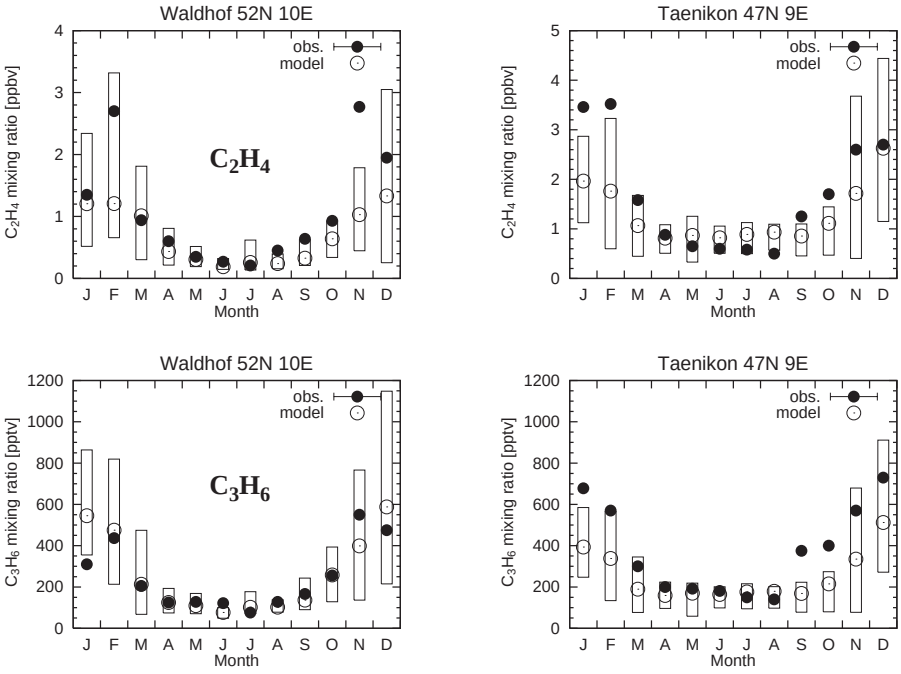

Figure 2.19. Observed (solid circles) and calculated (open circles) surface C_2H_4 (upper) and C_3H_6 (lower) mixing ratios (ppbv). Boxes indicate the range of the day-to-day variability calculated by the model. Measurements are taken from *Solberg et al.* [1996].

In Figure 2.19, the calculated and the observed seasonal cycles of surface C_2H_4 and C_3H_6 are shown for two European sites. Alkenes such as C_2H_4, C_3H_6 are destroyed by the reaction with OH radical with a lifetime of $\sim$1 day, and also by the reaction with O_3 with a lifetime of a day or several days. The model captures the observed seasonal variations of C_2H_4 and C_3H_6, reproducing well the winter maxima as with C_2H_6 and C_3H_8.

The observed and the calculated vertical profiles of C_2H_6 and C_3H_8 are compared in Figure 2.20 and Figure 2.21, respectively. In the US-E-Coast region (ABLE-3B), the model does not capture the observed levels of C_2H_6 (1-2 ppbv) and C_3H_8 (0.7-0.8 ppbv) in the lower troposphere, probably indicating an underestimation of surface emissions around this region. In the Japan and the China-Coast regions (PEM-West-B), C_2H_6 and C_3H_8 levels are higher near the surface ($C_2H_6\sim$2 ppbv, $C_3H_8\sim$0.8 ppbv), associated with considerable emission sources around these regions. In these regions, the model appears to underestimate slightly C_3H_8 near the surface, though it reproduces the profiles of C_2H_6 observed there well. During PEM-West-A (September to October), C_2H_6 and C_3H_8 levels below 5 km in the Japan and China-Coast regions are lower by a factor of 2 compared to PEM-West-B (February to March). These seasonal variations in C_2H_6 and C_3H_8 are well simulated by the model. During TRACE-P, the model well simulates the C_2H_6 profiles as well as CO (Figure 2.16). In these tropical remote regions C_2H_6 distributions are relatively uniform in the vertical ranging from 200 to 400 pptv , while C_3H_8 is more variable and shows relatively low mixing ratios (5-100 pptv) due to its short chemical lifetime. For the observations in the tropical Pacific regions (PEM-Tropics-A and B), the model tends to overestimate C_2H_6 levels, whereas it appears to reproduce generally the observed C_3H_8 profiles. The overestimation of C_2H_6 in the tropical Pacific, coinciding with the CO overestimation as described above (Figure 2.16), may indicate large transport from source regions. In the biomass burning regions (TRACE-A), the model appears to successfully simulate the vertical distributions of both C_2H_6 and C_3H_8. In the E-Brazil region, the model captures the observed positive vertical gradient in the middle-upper troposphere associated with convective transport in this region (as revealed by *Fishman et al.* [1996]). The modeled increase in C_2H_6 in the upper troposphere appears to be somewhat smaller than that by the previous CHASER version [*Sudo et al.*, 2002b], probably indicating reduced convection over South America in the model. This may come from the differences in the base AGCM version and adopted horizontal resolution between this work and the previous [*Sudo et al.*, 2002b]. The CHASER model in this study uses the CCSR/NIES version 5.6 AGCM with the T42 horizontal resolution ($\sim 2.8^\circ \times 2.8^\circ$), while the previous CHASER uses the version 5.4 AGCM with the T21 resolution ($\sim 5.6^\circ \times 5.6^\circ$). In the S-Atlantic region, levels of C_2H_6 and C_3H_8 are higher ($C_2H_6\sim$800 pptv, $C_3H_8\sim$100 ppbv) in the upper troposphere as for CO (Figure 2.16). The observed increase in C_2H_6 and C_3H_8 with altitude over the S-Atlantic region is well reproduced by the model, though the discontinuous jumping at $\sim$7 km is not represented clearly. Although the model appears to overestimate the C_2H_6 and C_3H_8 profiles observed over the W-Africa-Coast region, it simulates the increases in 2-5 km due to

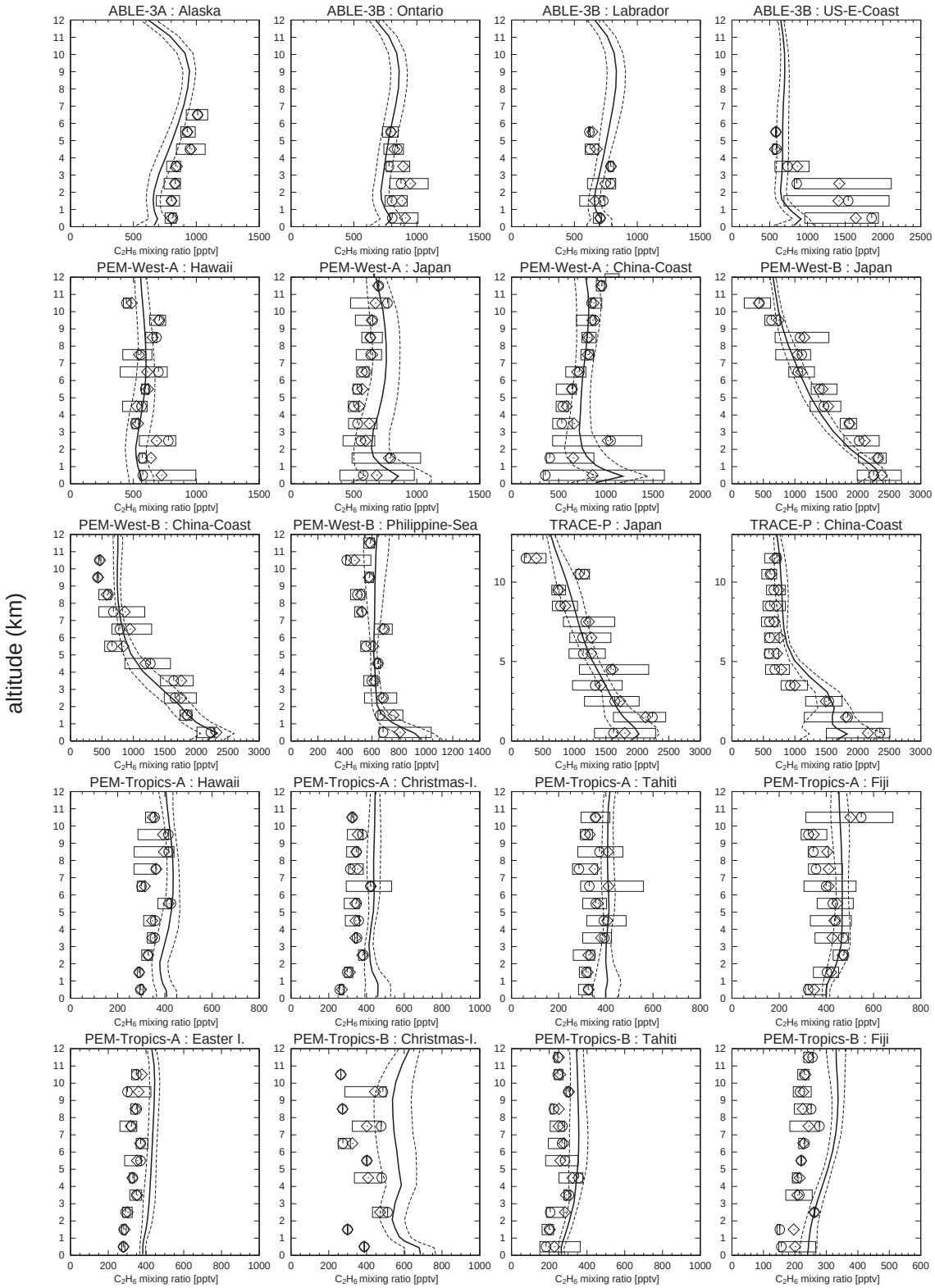

Figure 2.20. C_2H_6 vertical profiles observed and calculated over the regions of GTE campaigns (listed in Table 2.5). Solid lines and dashed lines show temporal mean and $\pm 1\sigma$ of the model calculation, respectively. The observations show mean (diamonds), median (circles), and inner 50% of the data (boxes).

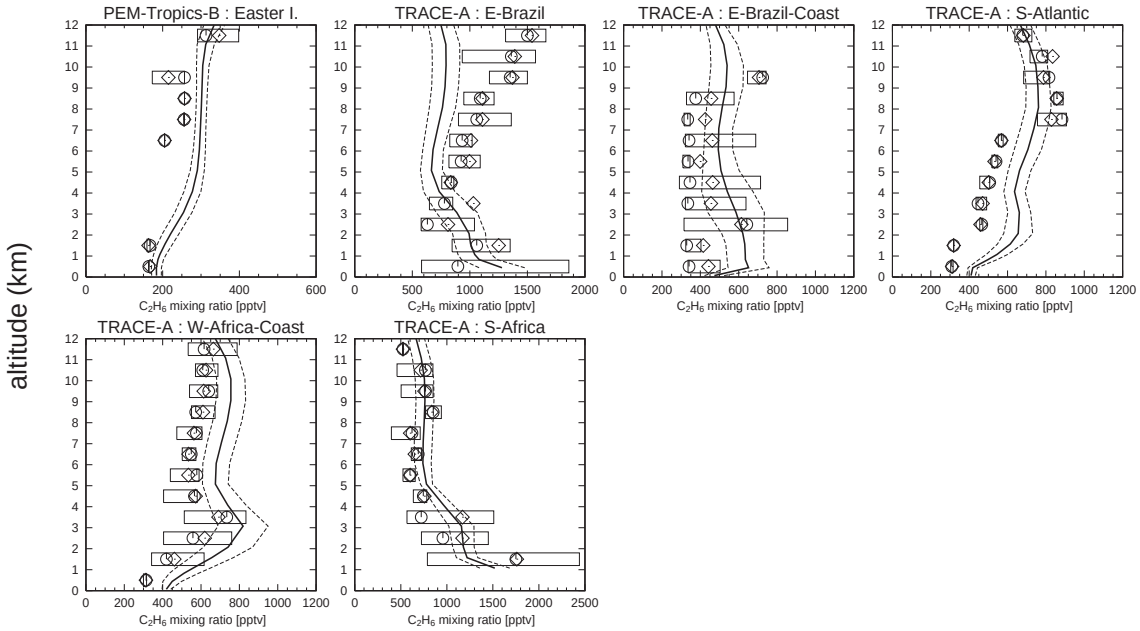

Figure 2.20. (continued).

African outflow as well as CO.

As isoprene and terpenes rapidly react with OH, O_3, and NO_3, they have much shorter lifetimes (hours), and the calculated distributions of these two NMHCs species are limited near source regions (i.e., vegetation) in the continental boundary layer. Figure 2.22 shows the distributions of isoprene calculated at the surface for January and July (24-hour average). The 24-hour averaged isoprene mixing ratios calculated in the boundary layer range from 1 ppbv to 8 ppbv in the tropical rain forests like the Amazon, in agreement with *Zimmerman et al.* [1988]. In July, the calculated mixing ratios of isoprene are 0.5-2 ppbv in temperate (deciduous) forests in the northern hemisphere, in agreement with measurements [e.g., *Martin et al.*, 1991; *Montzka et al.*, 1995]. Similarly, the terpenes distribution calculated near the surface has peaks in the tropical rain forests (1-2 ppbv), and shows high levels (0.2-1.5 ppbv) in cold-deciduous, needle-leaved forests in the northern high latitudes in July (not shown). In the model, the chemical lifetimes of isoprene and terpenes are estimated at 1.9 hour and 1.0 hour, respectively, in the annual and global average. The isoprene and terpenes mixing ratios calculated over the ocean are very low (generally equal to zero), due to their short chemical lifetimes.

2.3.2 Nitrogen species

Nitrogen oxides NO_x (= NO + NO_2) have a critical importance for ozone production and the HO_2/OH ratio in the troposphere. We must carefully evaluate the model results of NO_x and its reservoir species. Figure 2.23 shows the simulated NO_x distributions at the surface and 500

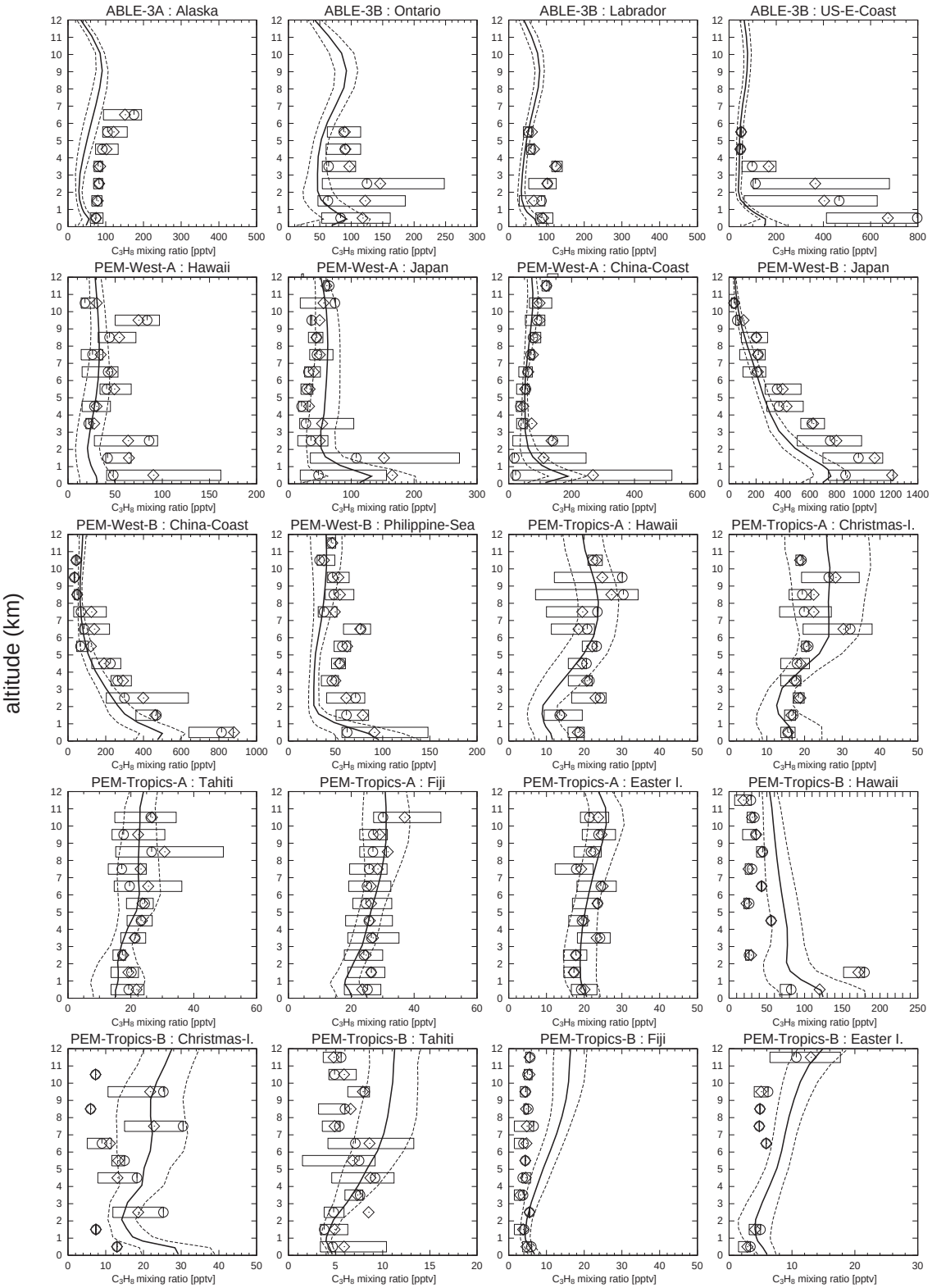

Figure 2.21. C_3H_8 vertical profiles observed and calculated over the regions of GTE campaigns (listed in Table 2.5). Solid lines and dashed lines show temporal mean and $\pm 1\sigma$ of the model calculation, respectively. The observations show mean (diamonds), median (circles), and inner 50% of the data (boxes).

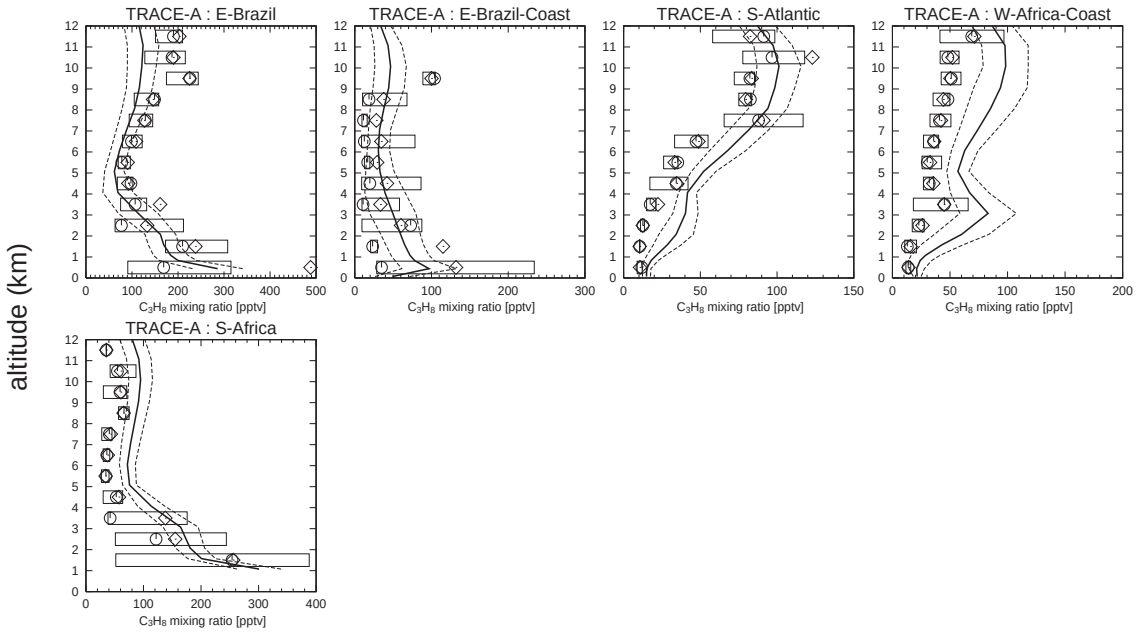

Figure 2.21. (continued).

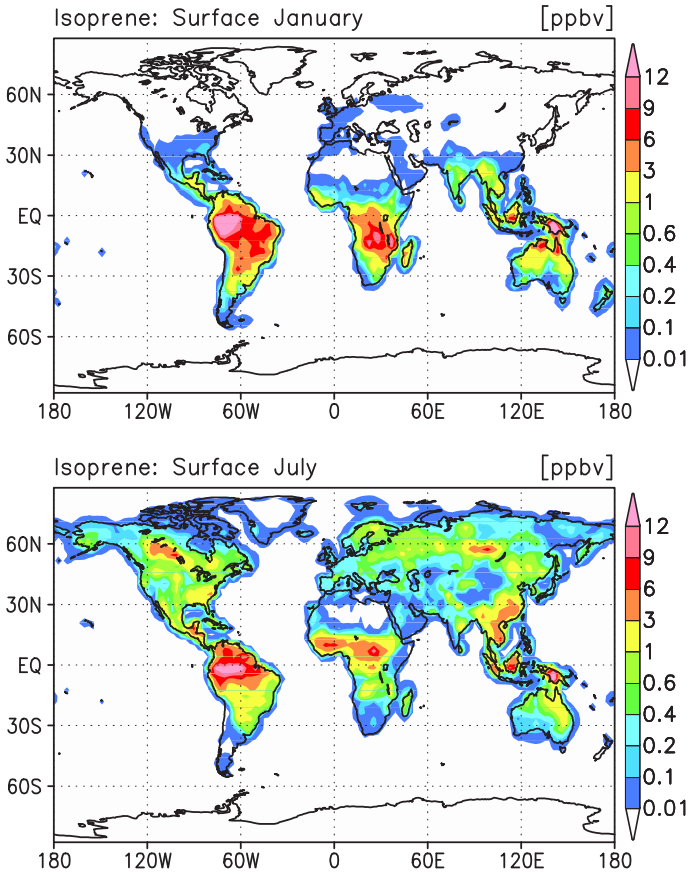

Figure 2.22. Calculated isoprene distributions (ppbv) at the surface for January and July.

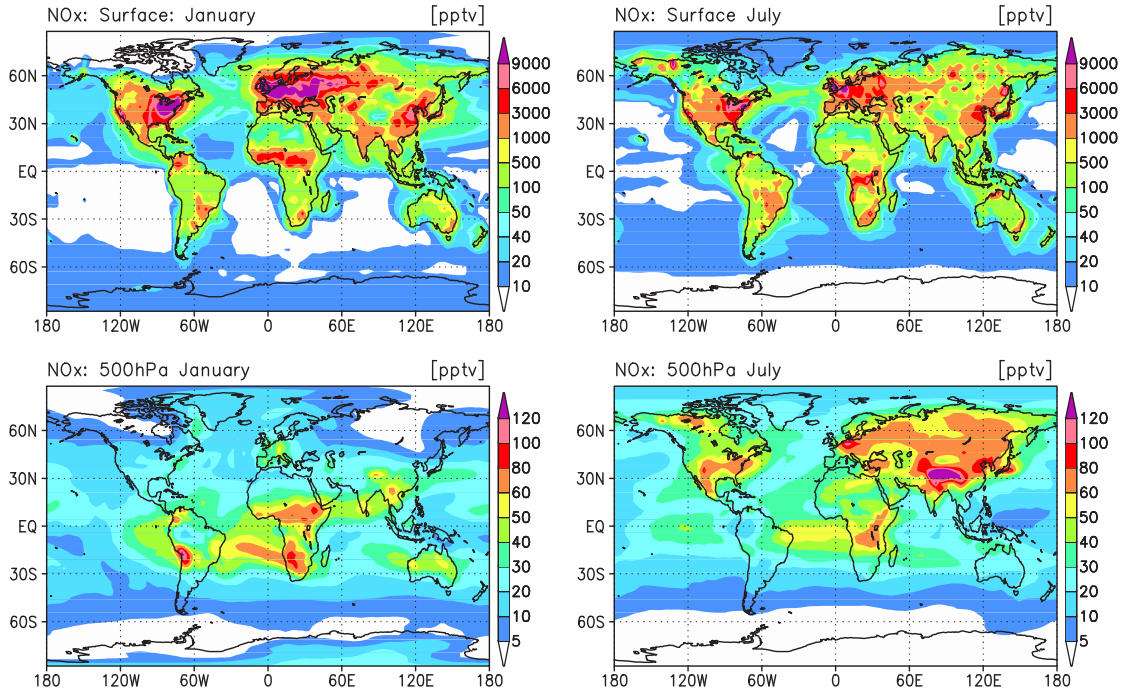

Figure 2.23. Calculated NO_x distributions (pptv) at the surface and 500hPa for January (left) and July (right).

hPa altitude for January and July. As NO_x is converted to HNO_3 by the reaction with OH on a timescale of a day near the surface, the NO_x distribution is highly limited near the continental source regions, especially in summer. Surface NO_x levels over the ocean are in the range of 10-80 pptv in winter and generally lower than 20 pptv near the surface. In July, the model calculates the NO_x mixing ratios of $\sim$3 ppbv over the eastern United States, somewhat higher than the simulation of *Horowitz et al.* [1998]. In January, the high NO_x concentrations of 5-10 ppbv are calculated in the eastern United States and Europe, reflecting a longer lifetime of NO_x. NO_x levels in those polluted regions are reduced by 30-50% compared to the previous version [*Sudo et al.*, 2002b] due to the heterogeneous reaction of N_2O_5 on aerosols (mainly sulfate in this study) which is not included in the previous version. At 500 hPa, NO_x peaks (60-100 pptv) are calculated over Africa and the Atlantic in January, associated with biomass burning in North Africa and with the lightning NO_x production. High NO_x concentration ($\sim$60 pptv) calculated over the Atlantic is also owing in the model to export from Africa and the in-situ NO_x recycling from HNO_3 and PAN. In the model, the positive net production of NO_x of 5-20 pptv/day is found in 6-12 km altitudes over the Atlantic, indicating the recycling process of NO_x. The calculation also shows a NO_x minimum (10-30 pptv) over South America (Brazil), reflecting rapid removal of HNO_3 by wet scavenging over this region during this season, and formation of PAN by the oxidation of biogenic NMHCs (mainly isoprene and terpenes). However, this NO_x minimum can be caused also by the overestimation of PAN formation by the chemical scheme of the model as described in the following. In July, the

model predicts high NO_x concentrations ($>$ 60 pptv) over continents in the northern hemisphere centered around the southeastern United States and eastern Asia (60-100 pptv). These are attributed to convective transport of NO_x from the surface and to the lightning NO_x production, though the effect of the lightning NO_x may be less visible at this altitude.

The observed and calculated vertical profiles of NO over the GTE regions listed in Table 2.5 are shown in Figure 2.24. Since the data includes only measurements in daytime (solar zenith angle $< 90^{\circ}$), the model results show average value of NO in daytime. In all cases, distributions of NO increase with altitude in the upper troposphere, due to the transport of stratospheric NO_x and HNO_3, the lightning NO_x production and the transport of surface emissions in convectively active regions, and increase in the lifetime of NO_x. Both the observations and calculations show high variability in the upper troposphere, reflecting the influence of stratospheric $NO_x$and lightning NO_x. The model simulates NO profiles well consistent with those observed during ABLE-3A (Alaska) and ABLE-3B (Ontario, US-E-Coast), calculating a rapid increase in the upper troposphere ($>$ 6 km) affected by stratospheric NO_x and HNO_3. The NO distributions over the polluted regions show "C-shaped" profiles. The model well simulates the observed "C-shaped" NO profile in the US-E-Coast (ABLE-3B), the China-Coast (PEM-West-B), the E-Brazil and the S-Africa (TRACE-A) regions. The model, however, overestimates the NO profiles in the Japan and China-Coast regions during TRACE-P. In the remote Pacific regions during PEM-Tropics-A and B, the model generally simulates the observed monotonic increase in NO with altitude. The NO profiles in the Hawaii region are, however, overestimated during both PEM-Tropics-A and B, due probably to the overestimation of PAN (see Figure 2.28), or possibly to overestimation of stratospheric influx of NO_y species such as NO_x, HNO_3, and N_2O_5. On the contrary, the model appears to underestimate NO above 8 km in Fiji and Tahiti during PEM-Tropics-A. The underestimations of NO in the upper troposphere over these regions may indicate the underestimation of lightning NO_x and/or biomass burning emission of NO_x in Australia. In the source regions of biomass burning (TRACE-A: E-Brazil, W-Africa-Coast, and S-Africa), the observations show "C-shaped" NO profiles, showing increase in the upper troposphere. The model appears to underestimate slightly NO levels in the upper troposphere (higher than 10 km) in these regions, with calculating NO profiles close to the observations in the lower-middle troposphere (below 10 km). Although this discrepancy appears to be caused by the underestimation of the flux of stratospheric NO_x, it can be attributed to the underestimation of lightning NO_x in the upper troposphere or the overestimation of PAN in the upper troposphere (the PAN/NO_x ratio is overestimated by a factor of 2-3 in the upper troposphere over these regions, Figure 2.29) , or possibly to the recycling of NO_x from HNO_3 on aerosols as tested in *Wang et al.* [1998b]. In the S-Atlantic region, both the observation and the calculation show a monotonic increase of NO with altitude, with the model slightly underestimating NO in the upper troposphere. The increase in the upper troposphere over S-Atlantic is related in the model to the gas-phase recycling of NO_x from HNO_3 and PAN, as well as the transport of NO_x from the

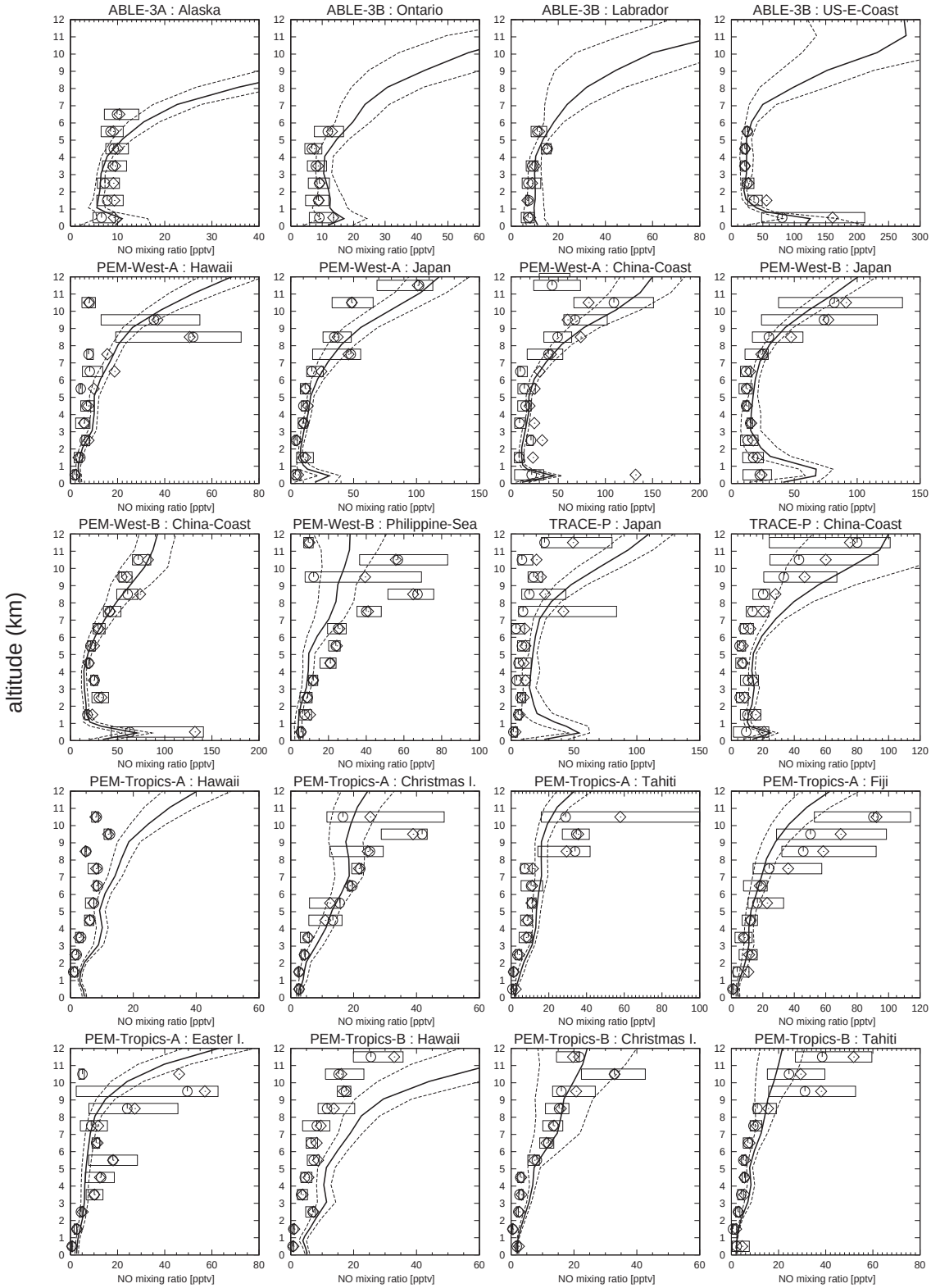

Figure 2.24. NO vertical profiles (in daytime) observed and calculated over the regions of GTE campaigns (listed in Table 2.5). Solid lines and dashed lines show temporal mean and $\pm 1\sigma$ of the model calculation, respectively. The observations show mean (diamonds), median (circles), and inner 50% of the data (boxes).

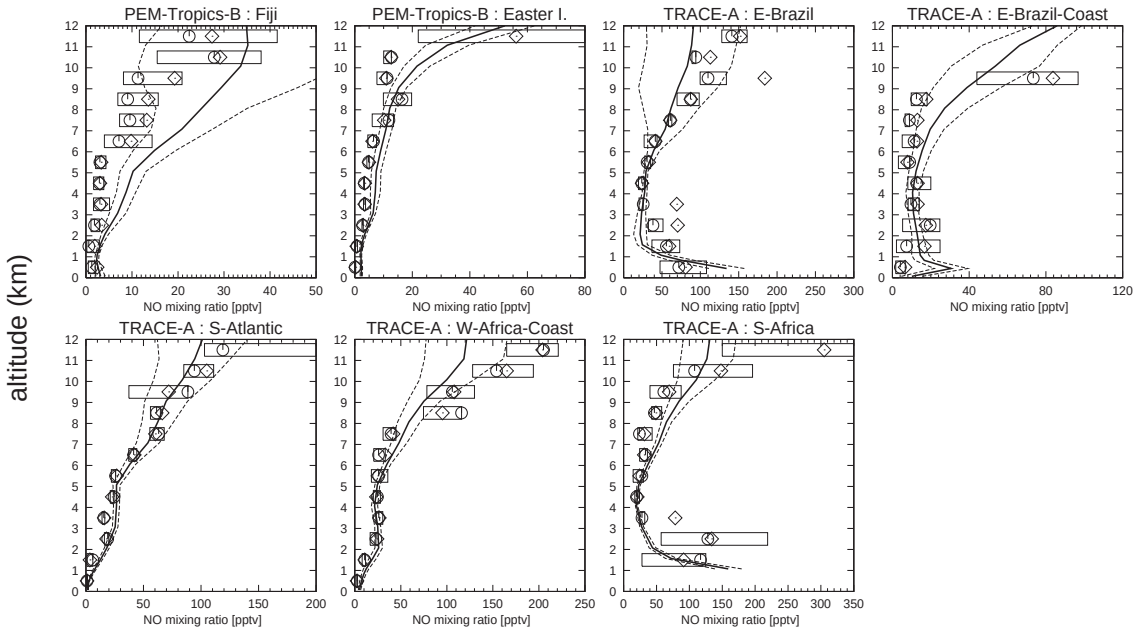

Figure 2.24. (continued).

source regions (South America and Africa). In the model, positive net production of NO_x (5-30 pptv/day) is calculated above 7 km over the Atlantic in September-October, indicating the recycling from HNO_3 and PAN exported from South America and Africa.

Figure 2.25 shows the calculated distributions of HNO_3 at the surface and 500 hPa altitude for January and July. Peaks of HNO_3 mixing ratio (higher than 2 ppbv) are calculated at the surface in the polluted areas as the eastern United States (also including California), Europe, India, China, and the biomass burning regions in both seasons. In July, the calculated HNO_3 mixing ratios in the eastern United States reach the range of 2-5 ppbv, higher than the measurements reported by *Parrish et al.* [1993] (1-2 ppbv). It should be noted that the model does not account for the conversion of HNO_3 to NO_x on aerosols (like soot) [*Hauglustaine et al.*, 1996; *Aumont et al.*, 1999; *Velders and Granier*, 2001, etc.] and particulate nitrates (NO_3^-) [e.g., *Singh et al.*, 1996] which would reduce gas-phase HNO_3. At 500 hPa, a clear maximum of HNO_3 (200-400 pptv) is calculated over the South Atlantic in January, due to the export from South America and Africa, and to sparse precipitation over this region. Low HNO_3 levels are calculated over South America (less than 40 pptv) at both the surface and 500 hPa in January. In the model, these low HNO_3 levels appear to be associated with convective precipitation during this season, and also with low NO_x levels due to strong PAN formation in the oxidation process of NMHCs emitted from vegetation. In July, a maximum of HNO_3 in the range of 400-500 pptv are calculated over the Eurasian Continent and the southern United States, associated with the lightning NO_x production and the convective transport of surface NO_x emission. A significant outflow of HNO_3 is visible over the eastern North Pacific

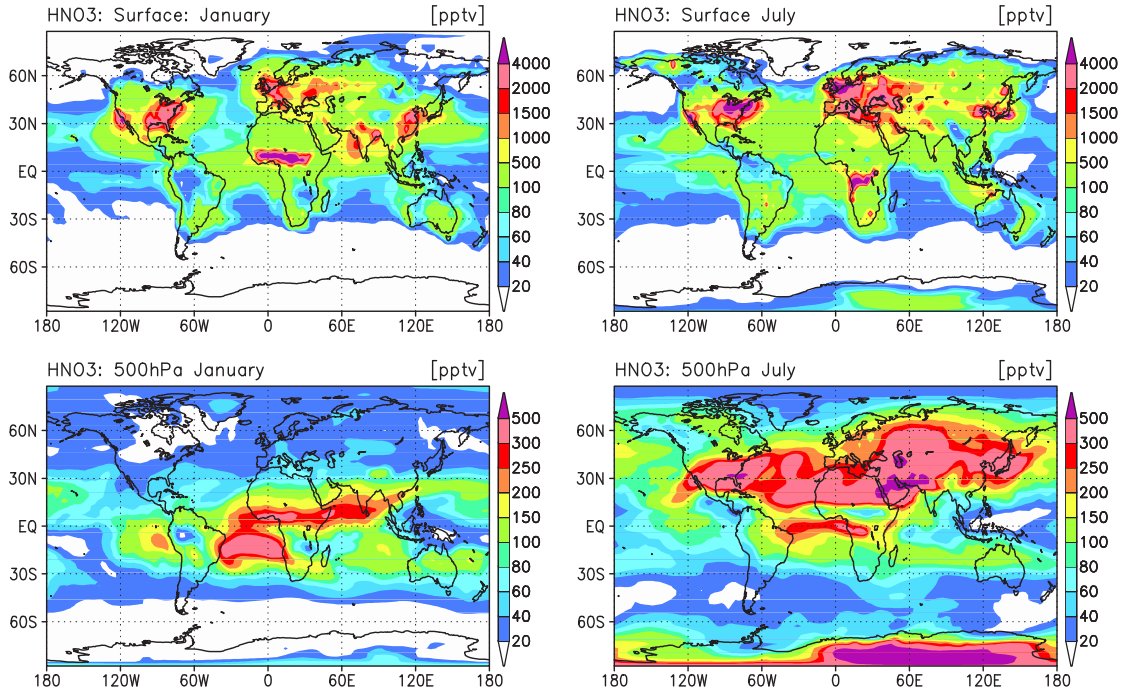

Figure 2.25. Calculated HNO_3 distributions (pptv) at the surface and 500hPa for January (left) and July (right).

including Hawaii from the western United States. This outflow, however, seems to be somewhat overestimated. HNO_3 and HNO_3/NO_x calculated at Mauna Loa are 1.5-2 times higher than the measurements by the Mauna Loa Observatory Photochemistry Experiment (MLOPEX) 1 and 2 [*Ridley and Robinson*, 1992; *Atlas and Ridley*, 1996]. High HNO_3 levels are also seen over the Antarctic continent in July, owing in the model to HNO_3 flux from the lower stratosphere associated with HNO_3 deposition due to ice particle sedimentation.

A comparison between the calculated and the observed vertical profiles of HNO_3 over the GTE regions listed in Table 2.5 is shown in Figure 2.26. In ABLE-3B (July-August), the calculated HNO_3 profiles show increase in the upper troposphere, reflecting the effect of stratospheric HNO_3. In comparison with the previous version of CHASER [*Sudo et al.*, 2002b], the model in this study calculates relatively low HNO_3 mixing ratios in the middle and upper troposphere over the Ontario, Labrador, and US-E-Coast regions, due to the improved wet deposition scheme considering deposition on ice cloud particles (see section 2.2.3). Similarly, the HNO_3 profile over the Japan region during PEM-West-B (February), which was overestimated by the previous CHASER, is well simulated in this study. A detailed evaluation of HNO_3 wet deposition flux is presented in section 2.2.3. In the tropical Pacific regions, the model generally reproduces the observed HNO_3 profiles (PEM-Tropics-A and B). The model, however, tends to overestimate lower tropospheric HNO_3 in the Hawaii region (PEM-Tropics-A and B) and the Christmas-Island and Tahiti regions

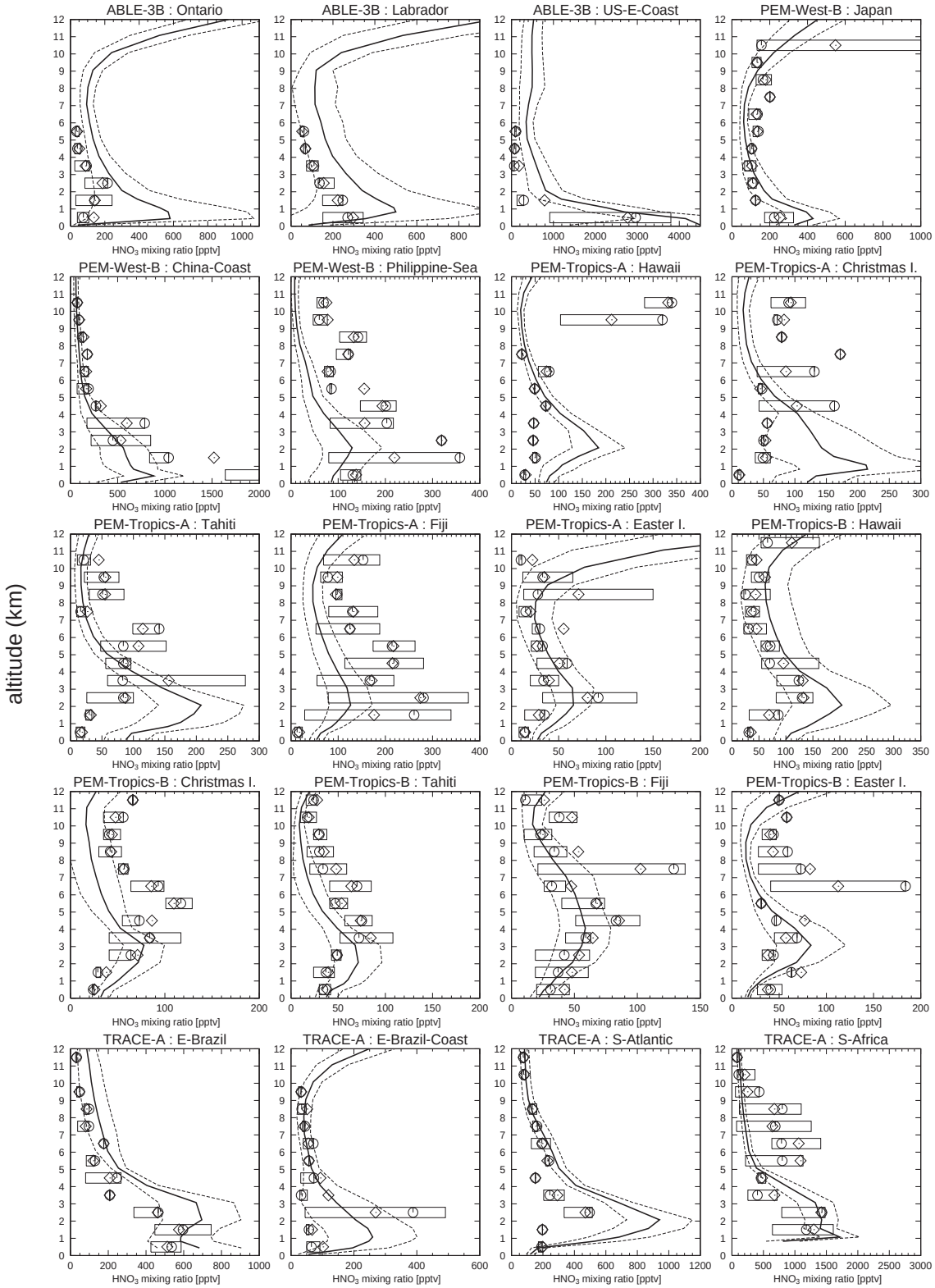

Figure 2.26. HNO_3 vertical profiles observed and calculated over the regions of GTE campaigns (listed in Table 2.5). Solid lines and dashed lines show temporal mean and $\pm 1\sigma$ of the model calculation, respectively. The observations show mean (diamonds), median (circles), and inner 50% of the data (boxes).

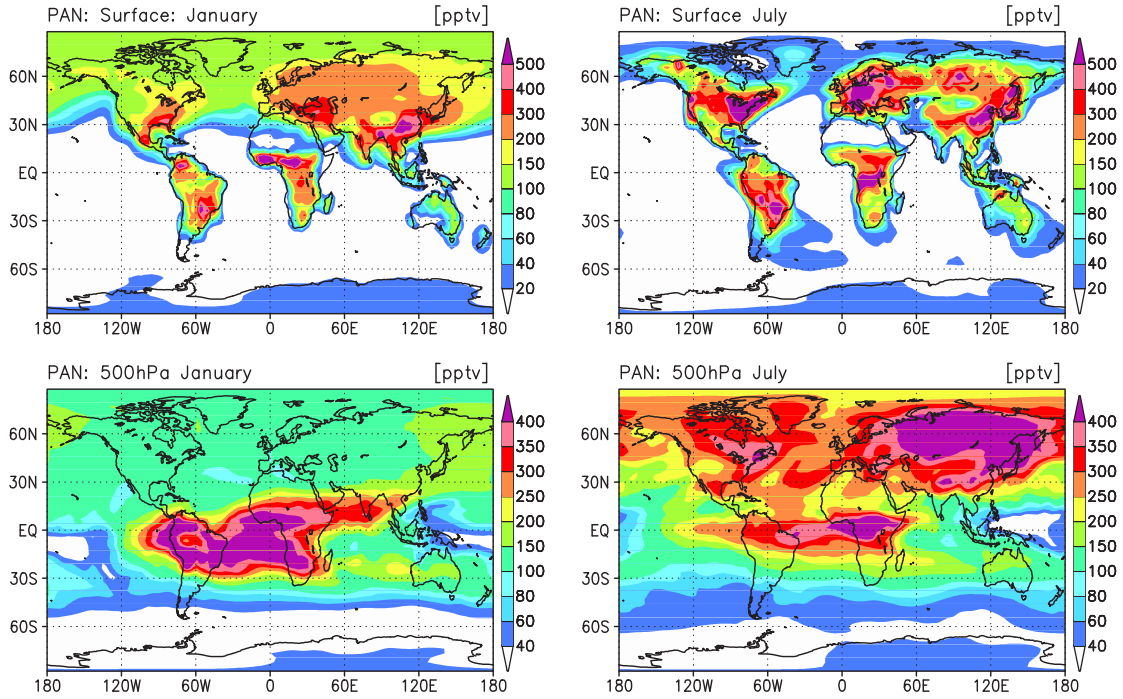

Figure 2.27. Calculated PAN distributions (pptv) at the surface and 500hPa for January (left) and July (right).

(PEM-Tropics-A). The overestimation in the Hawaii region appears to be related to too large outflow from the United States in the model. Also, HNO_3 outflow from the biomass burning regions in South America seems to result in the overestimation in the Tahiti region during PEM-Tropics-A. However, such overestimation may imply the existence of aerosol nitrates (NO_3^-) as revealed by *Singh et al.* [1996] which the model does not account for. In TRACE-A (September-October), an overestimation is found in 1-4 km over the S-Atlantic region as previous model simulations [e.g. *Wang et al.*, 1998b; *Lawrence et al.*, 1999]. The model results show that the calculated peak at about 2 km is much associated with the transport from Africa and hence the overestimation over the S-Atlantic (1-4 km) region is probably caused by the overestimation of HNO_3 in Africa as can be seen in the S-Africa region (Figure 2.26). The conversion of HNO_3 to NO on soot [*Hauglustaine et al.*, 1996; *Aumont et al.*, 1999; *Velders and Granier*, 2001, etc.] can be also a possible reason for this discrepancy. Consequently, the model results of HNO_3 and NO_x may indicate the necessity of consideration of particulate nitrates (NO_3^-) and reactions on soot affecting the HNO_3/NO_x ratio.

Peroxyacetyl nitrate (PAN) is also an important nitrogen species that acts as a source for NO_x in the remote atmosphere [*Fan et al.*, 1994; *Moxim et al.*, 1996]. PAN is formed by the reaction of NO_2 with peroxyacetyl radical and decomposes principally by thermolysis (slightly by photolysis). As peroxyacetyl radical is produced from the oxidation of NMHCs (ethane, propane, propene, acetone, isoprene, and terpenes in the model), we can validate the simplified scheme for NMHCs oxidation

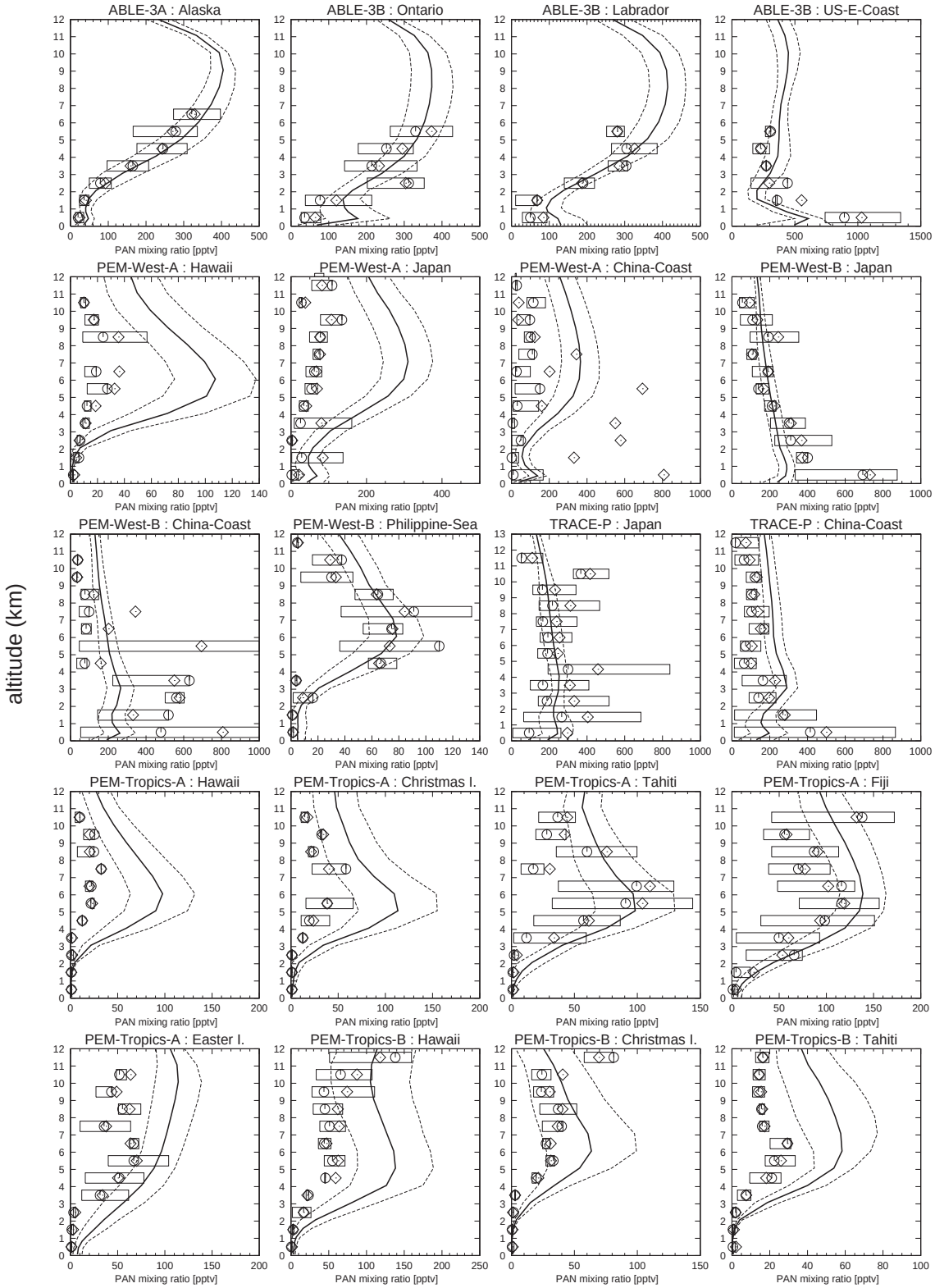

Figure 2.28. PAN vertical profiles observed and calculated over the regions of GTE campaigns (listed in Table 2.5). Solid lines and dashed lines show temporal mean and $\pm 1\sigma$ of the model calculation, respectively. The observations show mean (diamonds), median (circles), and inner 50% of the data (boxes).

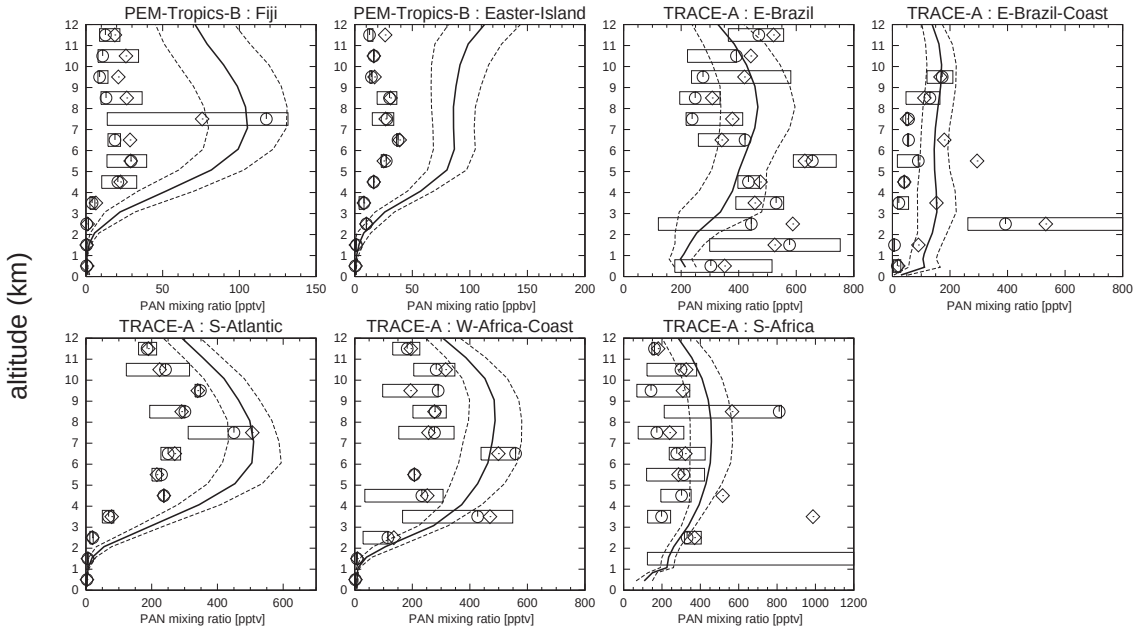

Figure 2.28. (continued).

adopted in the model by evaluating the simulation of PAN. Figure 2.27 shows the calculated PAN distributions at the surface and 500 hPa for January and July. At the surface in January, high levels of PAN (300-500 pptv) are calculated in South America and Africa associated with biogenic emissions of NMHCs over these regions. The model calculates the PAN concentrations of 150-300 pptv in the mid-high latitudes with a maximum (400-600 pptv) around India and China. In July, high concentrations of PAN (above 500 pptv) are predicted at the surface in the polluted areas (United States, Europe, eastern Asia including Japan). The model results for the eastern United States in summer are consistent with the observation of *Parrish et al.* [1993] (0.5-1.5 ppbv). At 500 hPa in January, the model calculates high levels of PAN (300-450 pptv) over South America, Africa, and the South Atlantic, associated with NMHCs emissions by vegetation and lightning NO_x over South America and Africa. The calculated high concentrations of PAN over the Atlantic contribute to the positive net production (recycling) of NO_x (5-20 pptv/day) calculated in the middle-upper troposphere over the Atlantic during this season as described above. In July, high concentrations of PAN (above 300 pptv) are calculated over continents in the northern hemisphere with a maximum (above 400 pptv) over the eastern Eurasian Continent, due to the lightning NO_x production and surface emissions of NO_x and NMHCs.

Figure 2.28 shows the calculated and the observed vertical profiles of PAN over the GTE regions. In the Alaska region during ABLE-3A (July-August), the model calculates increase of PAN with height with showing mixing ratios of 300-400 pptv in the upper troposphere, in excellent agreement with the observation. The calculated PAN profiles over the Ontario, Labrador, and US-E

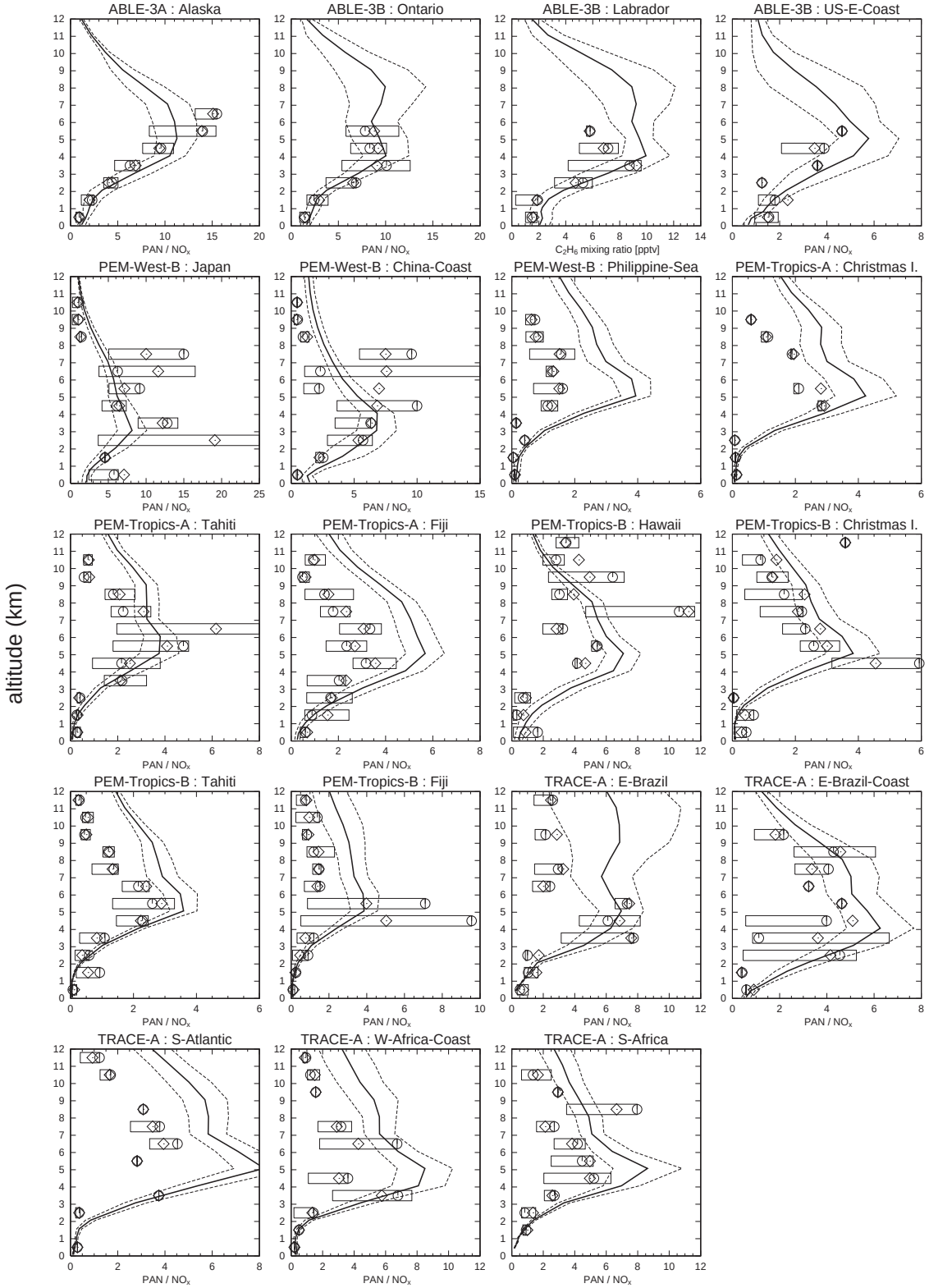

Figure 2.29. PAN/NO_x ratio vertical profiles observed and calculated over the regions of GTE campaigns (listed in Table 2.5). Solid lines and dashed lines show temporal mean and $\pm 1\sigma$ of the model calculation, respectively. The observations show mean (diamonds), median (circles), and inner 50% of the data (boxes).

regions (ABLE-3B) are also consistent with the observations. In the Japan and the China-Coast regions during PEM-West-B and TRACE-P, PAN levels increase near the surface (400-800 pptv), reflecting the abundance of NMHCs (e.g., Figure 2.20, Figure 2.21) and NO_x (Figure 2.24). In the Japan region, the model well simulates the observed PAN profiles for PEM-West-B and TRACE-P, but overestimates significantly for PEM-West-A especially in the upper troposphere. The same kind of overestimation by the model appears in the Hawaii region during PEM-West-A and PEM-Tropics-A and B. The overestimation in the Hawaii region is attributed to transport from eastern Asia and the United States. For Fiji and Tahiti (PEM-Tropics-A), both the observation and the model show a peak of PAN (80-150 pptv) in 4-8 km, associated with the transport of PAN from South America, Africa, and Australia. The model, however, overestimates the PAN profiles in 4-10 km over the tropical Pacific regions during PEM-Tropics-B (March-April) by a factor of 1.5-3, maybe indicating that the condensed isoprene and terpenes oxidation scheme [*Pöschl et al.*, 2000] (see *Sudo et al.* [2002a]) or the lumped NMHCs species (ONMV, see *Sudo et al.* [2002a]) in the model produces too much peroxyacetyl radical and hence too much PAN. Similar overestimation of PAN in the tropical Pacific is seen in the simulation by the MOZART model [*Horowitz et al.*, 2002]. In the biomass burning regions (TRACE-A), the model appears to reproduce the observed profiles of PAN, simulating the rapid decrease in PAN below 3 km (nearly zero) over the S-Atlantic region and the W-Africa-Coast region, and the increase in the middle troposphere (300-500 pptv). The model, however, tends to overestimate PAN levels in the middle-upper troposphere, indicating too strong PAN formation again. Figure 2.29 shows the calculated and the observed vertical profiles of PAN/NO_x ratio over the GTE regions. The ratio is calculated in each time step in the model. The model generally reproduces the observed PAN/NO_x ratios well, calculating a peak in the middle troposphere for individual cases. The observed and calculated peaks in the middle troposphere are generally in the range of 5-10 in the polluted areas, and lower than 5 in the remote regions. An overestimation of the PAN/NO_x ratio in the Philippine-Sea region is associated with the underestimation of NO_x in this region (Figure 2.24). The calculated PAN/NO_x profile in the Hawaii region (PEM-Tropics-B) is relatively consistent with the observation, while both NO_x and PAN in this region are overestimated by the model (Figure 2.24 and 2.28). For the regions of TRACE-A, the model overestimates the PAN/NO_x ratio in the upper troposphere by a factor of 2-3, due to the underestimation of NO_x and the overestimation of PAN in these regions as described above.

The seasonal cycle of PAN calculated at the surface is also compared with the observational data for several sites [*Bottenheim et al.*, 1994; *Houweling et al.*, 1998; *Ridley et al.*, 1998] (not shown). It was found that the model overestimates PAN at Mauna Loa by a factor of 2, compared to the data of the MLOPEX [*Ridley et al.*, 1998]. For other sites, the calculated seasonal variations of PAN are consistent with observations.

The overestimation of PAN by the model in some instances may be attributed primarily to overestimation of peroxy acetyl radical (CH_3COO_2) by the simplified chemical mechanism for

Table 2.7. Global budget of NO_y species (TgN/yr) Calculated by CHASER.

	Global	NH	SH
Sources	44.3		
Surface Emission	38.8		
Lightning NO_x	5.0	2.93	2.07
Aircraft NO_x	0.55		
Sinks	−45.1	−35.5	−9.6
Wet deposition	−25.8	−19.8	−6.0
HNO_3	−25.2	−19.4	−5.8
HNO_4	−0.57	−0.39	−0.18
Dry deposition	−19.4	−15.7	−3.7
HNO_3	−13.8	−11.5	−2.3
HNO_4	−0.03	−0.023	−0.007
NO_x	−3.85	−3.05	−0.8
PANs [a]	−1.28	−0.86	−0.42
ISON [b]	−0.35	−0.21	−0.14
NALD	−0.04	−0.023	−0.017

$NO_y = NO + NO_2 + NO_3 + 2\,N_2O_5 + HNO_3 + HNO_4 + PAN + MPAN + ISON + NALD$ in the model (NALD = nitroxy acet aldehyde).

[a]PAN (peroxyacetyl nitrate) + MPAN (higher peroxyacetyl nitrates).

[b]Isoprene nitrates.

NMHCs used in the model, as mentioned above. The simulation with the previous CHASER version [*Sudo et al.*, 2002b] has suggested heterogeneous loss of some peroxy radicals (RO_2) including CH_3COO_2 on aerosols [*Jacob*, 2000] for another possibility, as RO_2 radicals formed by isoprene and terpenes oxidation are precursors of CH_3COO_2 radical. Although such heterogeneous reactions are included in this study (see section 2.2.1), there do not seem to be significant differences between this work and the previous one [*Sudo et al.*, 2002b]. Further investigation is needed to validate the uptake coefficients (γ values) for the heterogeneous reactions of RO_2 and products from those heterogeneous reactions (assumed to be peroxides ROOH) in the model (section 2.2.1).

The budget of total nitrogen species (NO_y) calculated by CHASER is shown in Table 2.7. In this simulation, the NO_y sources amount to 44.3 TgN/yr (87.5%, surface emission; 11.3%, lightning; 1.2%, aircraft). They are balanced primarily with the wet and dry deposition of HNO_3 ($\sim$88% of the source) in the model. About 60% of the global lightning NO_x emission is calculated in the northern hemisphere. The calculated global wet deposition of HNO_3 reaches a maximum in August-September. About 80% of the global deposition loss of HNO_3 is calculated in the northern hemisphere (20% in the southern hemisphere). A slight imbalance between the total source and the total sink for NO_y (0.8 TgN/yr) is attributed to transport from the stratosphere.

2.3.3 HO_x and related species

OH radical plays a central role in the oxidation of chemical compounds (the oxidizing power of the atmosphere) and the production and destruction of ozone. OH is converted to HO_2 by the reactions with O_3, peroxides, and CO, and reversely HO_2 is converted to OH by the reactions with O_3 and NO on a timescale of minutes. HO_x (= OH + HO_2) is produced by the reaction of $O(^1D)$ with water vapor (H_2O) [*Levy*, 1971] and also by the oxidation of CH_4 and NMHCs. Decomposition of peroxides can be also a HO_x source in the upper troposphere [e.g., *Jaeglé et al.*, 1997; *Folkins et al.*, 1998; *Cohan et al.*, 1999]. The sinks for HO_x are the reactions of OH with CH_4, NMHCs, and HO_2, and the reactions of HO_2 with peroxy radicals to form peroxides (e.g., H_2O_2, CH_3OOH).

HO_x

Figure 2.30 shows the zonal mean concentrations (molecules cm^{-3}) of OH calculated for January and July. In January, the calculated OH distribution shows a maximum ($\sim 2.0\times10^6$ molecules cm^{-3}) in 10°S-30°S, reflecting the distributions of O_3, water vapor (H_2O), and UV radiation. This OH maximum is calculated at 2-4 km altitude, indicating the significant OH destruction by NMHCs and CO near the surface. We conducted a simulation without NMHCs chemistry. The simulation suggests that inclusion of NMHCs in the model reduces OH concentrations by a factor of 30-60% near the surface over land, as indicated by previous studies [e.g., *Wang et al.*, 1998c; *Roelofs and Lelieveld*, 2000]. In July, high concentrations of OH (2.5-3.0$\times10^6$ molecules cm^{-3}) are calculated in the northern midlatitudes in spite of the OH depletion by CO and NMHCs, as a result of high NO_x levels and enhanced O_3 over continents [*Thompson*, 1992]. Although the zonal mean OH distributions calculated for January and July are similar to those calculated by previous studies [e.g., *Müller and Brasseur*, 1995; *Wang et al.*, 1998b; *Hauglustaine et al.*, 1998], the maximum values of OH concentrations calculated in this simulation appear to be somewhat (10-30%) higher than them, probably indicating the differences in O_3 and NO_x levels. The tropospheric OH distribution presented here results in a global annual average of 1.06 $\times10^6$ molecules cm^{-3} (below 200 hPa), in good agreement with the simulations of *Spivakovsky et al.* [2000] (1.16 $\times10^6$ molecules cm^{-3}) and *Roelofs and Lelieveld* [2000] (1.00 $\times10^6$ molecules cm^{-3}). The annual and zonal mean HO_2/OH ratios calculated in the low-mid latitudes (45°S-45°N) are in the range of 50-100, and 100-600 in the high latitudes in both hemispheres below 200 hPa, much associated with the distribution of CO, O_3, and NO (not shown).

Data available for evaluation of OH and HO_2 are quite limited because of the difficulty of measuring them. We made use of the data obtained during the NASA GTE campaigns (PEM-Tropics-B and TRACE-P) for evaluation of the HO_x distribution. The PEM-Tropics-B mission provided the first extensive measurements of the OH radical in the tropical troposphere. In Figure 2.31, the OH and HO_2 vertical profiles observed and calculated for the regions of the PEM-Tropics-B and

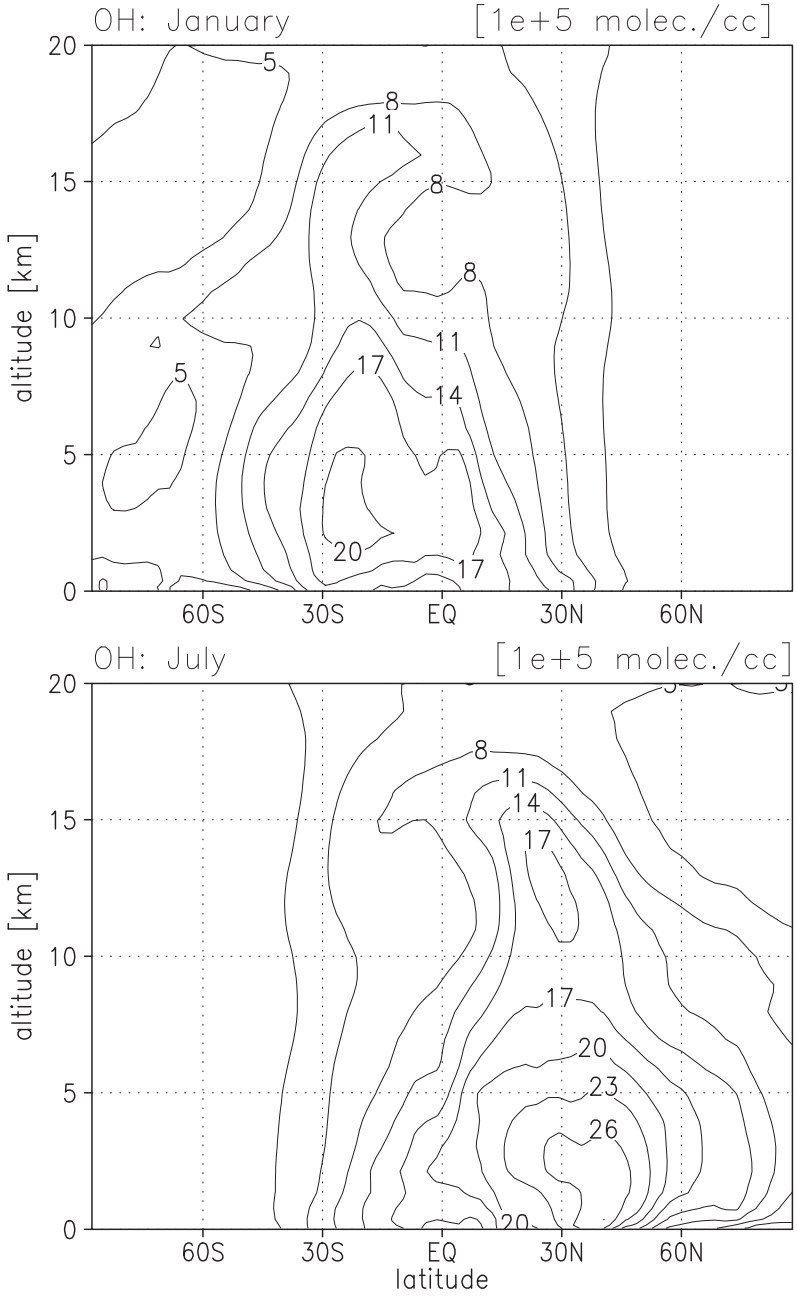

Figure 2.30. Zonal mean OH distributions (10^5 molecules cm^{-3}) calculated for January and July. Contour interval is 3 (10^5 molecules cm^{-3}).

TRACE-P expeditions are shown. The model results are again averaged over the regions in Table 2.5 and dates during the expeditions (March 6 to April 18 for PEM-Tropics-B, March 3 to April 15 for TRACE-P). Since most of the GTE flights were taken place in daytime, we display the calculated mixing ratios of OH and HO_2 in the daytime average except for the Easter-Island region during PEM-Tropics-B where the mission includes nighttime flights after sunset (We compare the 24-hour averaged model results for the Easter-Island region). In this comparison, we must

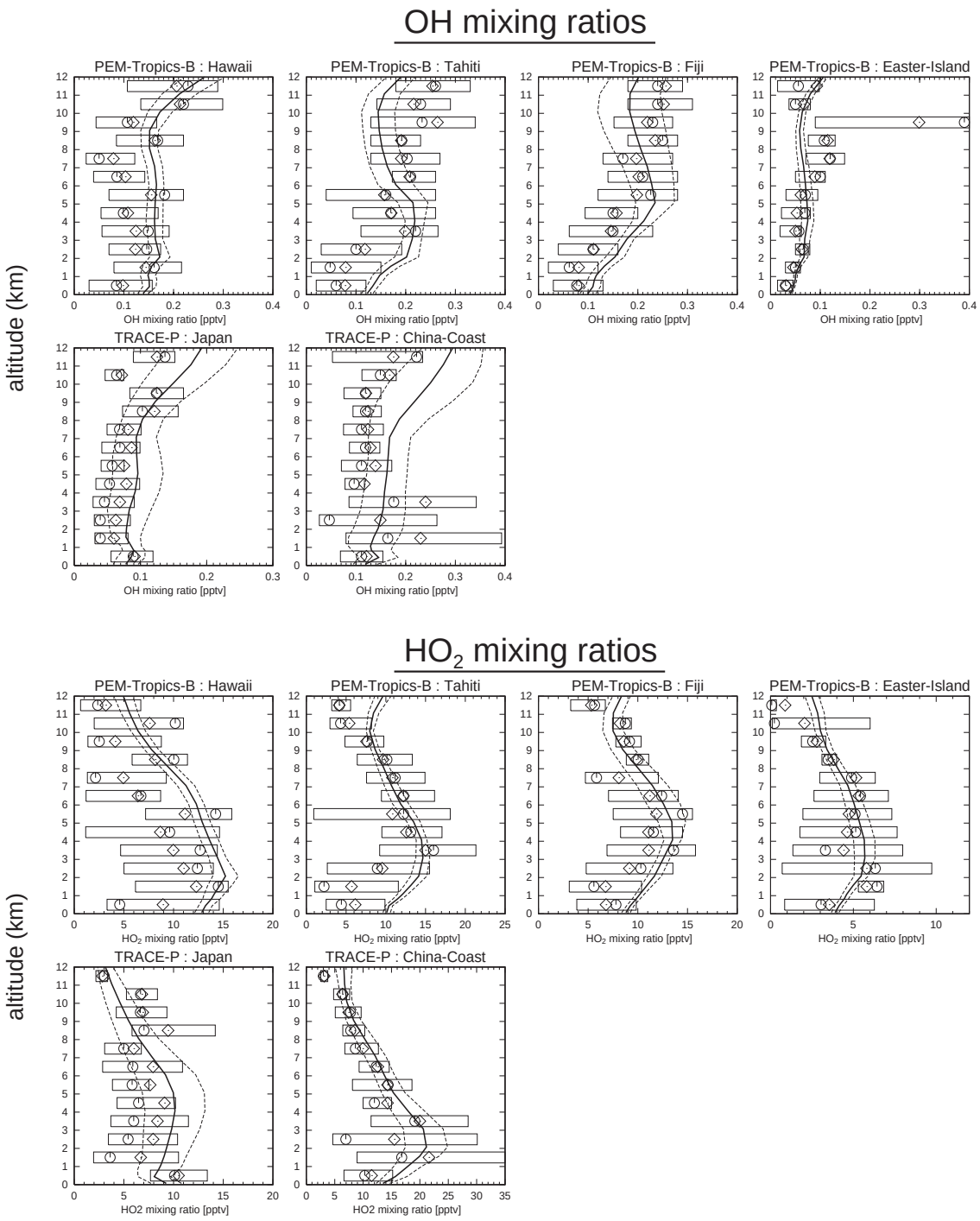

Figure 2.31. OH (upper) and HO_2 (lower) vertical profiles observed and calculated over the regions of GTE campaigns (listed in Table 2.5). The model results show mixing ratios of OH and HO_2 in the daytime average except for Easter-Island in the 24-hour average. Solid lines and dashed lines show temporal mean and $\pm 1\sigma$ of the model calculation, respectively. The observations show mean (diamonds), median (circles), and inner 50% of the data (boxes).

note again that values measured by a flight campaign are fragmentary with respect to time and space for individual altitudes, and there may be discrepancies in representation of time and space between measurements and model calculations especially for short-lived radicals such as OH and HO_2. The comparison appears to show that the calculated HO_x species are generally consistent with the measurements. Daytime mixing ratios of OH and HO_2 are in the ranges of 0.05-0.3 pptv and 5-20 pptv, respectively. In the China-Coast region during TRACE-P, the model well captures the observed HO_2 increase ($\sim$20 pptv) in 1-4 km altitudes. This HO_2 enhancement over the China-Coast region appears to be coinciding with the increase in CH_2O and acetone (Figure 2.34 and 2.35) associated with industrial emissions in China and transport from the biomass burning regions in southeastern Asia. The HO_2/OH ratio decreases in the upper troposphere, due to the increase in O_3 and NO. In the Fiji and Tahiti regions during PEM-Tropics-B, OH mixing ratios in the upper troposphere are considered to be underestimated by 20-40%. This discrepancy may be attributed to the slight overestimation of CO and the underestimation of NO in the upper troposphere over the tropical Pacific. The calculated profiles of water vapor, ozone, acetone, CH_2O (see Figure 2.34) and CH_3OOH (Figure 2.40) over Fiji and Tahiti are generally consistent with the measurements during the PEM-Tropics-B, and the HO_x production rate calculated in the upper troposphere (8-12 km) over Fiji ranges from 500 to 2000 pptv/day, in good agreement with the box model calculation for the flight 10 around Fiji during the PEM-Tropics-B experiment [*Mari et al.*, 2001]. In the Japan and China-Coast regions (TRACE-P), the modeled OH levels are 1.5-2 times higher than the observation especially in the middle-upper troposphere. This appears to originate from the overestimation of NO_x (NO) in these regions during TRACE-P as shown in Figure 2.24.

The global OH field calculated by the model is also evaluated by comparing lifetime of CH_4 (methane) and CH_3CCl_3 (metylchloroform) in the model with measurements. *Prinn et al.* [1995] derived a global lifetime of 4.9$\pm$0.3 years for CH_3CCl_3 below 200 hPa regarding OH oxidation, and obtained a global methane lifetime of 8.9$\pm$0.6 years, based on observed CH_3CCl_3 concentrations. In this simulation, the calculated global OH concentrations (below 200 hPa) lead to a global CH_3CCl_3 lifetime of 5.0 years (4.5 years in the northern hemisphere, 5.6 years in the southern hemisphere), in excellent agreement with the CH_3CCl_3 lifetime suggested by *Prinn et al.* [1995] (4.9$\pm$0.3 years). The global methane lifetime, defined as (global methane burden)/(OH destruction within the troposphere), is calculated as 9.4 years in this simulation. This estimated methane lifetime against tropospheric OH is well within the range suggested by *Prinn et al.* [1995] (0.89$\pm$0.6 years), and is also close to the recent IPCC estimate (9.6 years) [*Prather et al.*, 2001].

Figure 2.32 shows the 24-hour average distributions of HO_x production rate (pptv/day) calculated in the upper troposphere (8-13km) for January and July. As can be expected, the HO_x production in the upper troposphere is anomalously high in regions of high NMHCs level in the low latitudes. The HO_x production is high (3000-6000 pptv/day) over the tropical rainforests associated with biogenic emissions of NMHCs, being also high in July over the eastern United States and

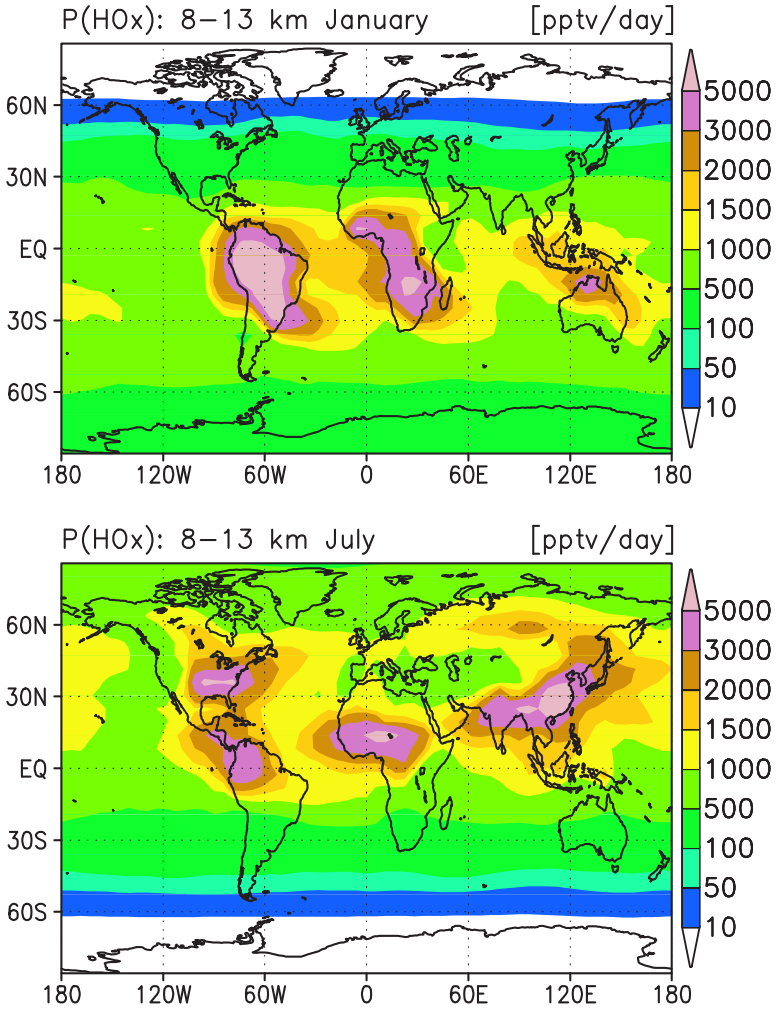

Figure 2.32. Distributions of the HO_x production term $P(HO_x)$ (pptv/day) in the upper troposphere (averaged over 8-13 km altitude) calculated for January and July.

eastern Asia (India, China) (above 3000 pptv/day). Over the ocean in the low latitudes, the calculated production rate is in the range of 500-1500 pptv/day off continents, and 1500-3000 pptv/day in the vicinity of continents (e.g., over the South Atlantic in January and over the western Pacific including Japan in July).

The global HO_x production and the mean lifetime of HO_x calculated by the model below the tropopause are presented in Table 2.8. The model calculates a global HO_x production of 215 TgH/yr corresponding to 1.3×10^{38} molecules/yr (58% in the northern hemisphere), and a global mean lifetime of 4.5 min. The differences in the production and the lifetime between the northern hemisphere and the southern hemisphere are owing to differences in the abundance of O_3 and NMHCs.

Table 2.8. Chemical Production and Lifetime of HO_x Calculated by CHASER.

	Global	NH	SH
Chemical production (TgH/yr)	214.7	124.2	90.5
Chemical lifetime (min)	4.5	3.7	5.7

TgH/yr corresponds to 6.02×10^{35} molecules/yr.

Formaldehyde and acetone

The primary source for HO_x is the photolysis of ozone followed by the reaction of $O(^1D)$ with water vapor (H_2O). In dry regions as in the upper troposphere, acetone (CH_3COCH_3) [*Singh et al.*, 1995; *Arnold et al.*, 1997; *McKeen et al.*, 1997; *Wennberg et al.*, 1998], and formaldehyde and other aldehydes produced in the oxidation of methane and NMHCs [*Müller and Brasseur*, 1999] become important HO_x sources. Figure 2.33 shows the calculated distributions of formaldehyde (CH_2O) and acetone in the upper troposphere (8-13 km average) for January and July. CH_2O decomposes by photolysis on a timescale of hours in summer and hence effectively produces HO_x. In Figure 2.33, high concentrations (100-400 pptv) of CH_2O are calculated over the regions where NMHCs are abundant (i.e., tropical rainforests, the eastern United States, eastern Asia), well correlated with the

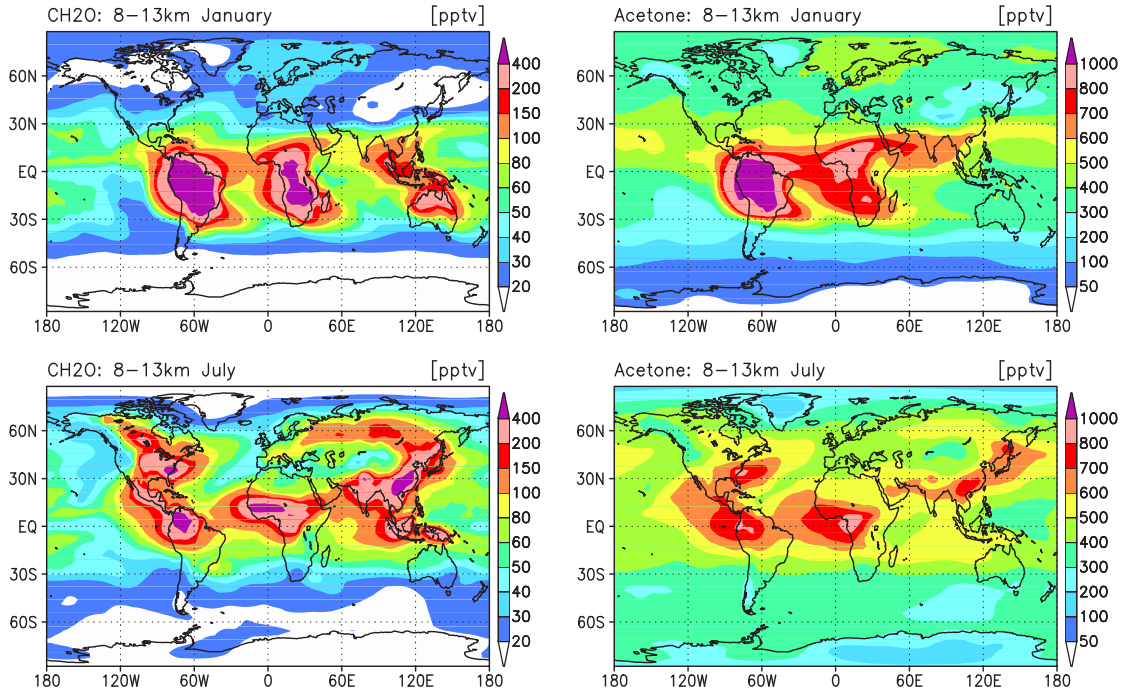

Figure 2.33. Calculated CH_2O (left) and acetone (right) distributions (pptv) in the upper troposphere (averaged over 8-13 km) for January and July.

HO_x production in the upper troposphere in Figure 2.32. Acetone similarly produces HO_x in the upper troposphere by its photolysis. As the lifetime of acetone against photolysis and OH oxidation is much longer than CH_2O (calculated global mean lifetime of acetone is 27 days), acetone can be an important source for HO_x in remote regions as well as in source regions. The distributions of acetone (Figure 2.33) indicate the contribution of acetone to the HO_x production in the upper troposphere. In this simulation, the model includes acetone emission sources of 1.02 TgC/yr from industry, 4.88 TgC/yr from biomass burning, 11.2 TgC/yr from vegetation, and 12.0 TgC/yr from ocean. The model secondarily considers the acetone source from oxidation of NMHCs (propane C_3H_8 and terpenes in this simulation, see section 2.2.1). The calculated acetone in 8-13 km is high (700-1200 pptv) over South America and Africa including the South Atlantic in January, reflecting the emissions of acetone by vegetation and biomass burning, and the photochemical production of acetone by the oxidation of propane and terpenes. A long range transport of acetone from eastern Asia and North Africa to the North Pacific is visible in January associated with the long chemical lifetime of acetone in winter ($>$ 1 month). In July, the calculated distribution of acetone in the upper troposphere (8-13 km) is somewhat similar to that of CH_2O, showing peaks ($>$ 600 pptv) over the eastern United States, eastern Asia, and the tropical rain forests.

Simulated vertical profiles of CH_2O and acetone are compared with the observations of the NASA GTE campaign in Figure 2.34 and 2.35, respectively. In Figure 2.34, the model simulates the CH_2O vertical profiles very well in the tropics observed during PEM-Tropics-B, though underestimating CH_2O in the upper troposphere over the Tahiti region. In these tropical regions, both the observation and the calculation show the CH_2O mixing ratios of 300-400 pptv near the surface and lower than 100 pptv in the upper troposphere (above 6 km). In the source regions of biomass burning (E-Brazil, S-Africa in TRACE-A), the model tends to overestimate CH_2O near the surface. In the west of African coast (W-Africa-Coast), CH_2O distribution is overestimated by the model at all altitudes, though the observed increase in the lower troposphere is simulated qualitatively. Our evaluation shows also a large overestimation of CH_2O in the South Atlantic region during the TRACE-A (not shown here). The overestimation of CH_2O over these regions may suggest that the chemical scheme for oxidation of isoprene, terpenes, and a lumped NMHCs species (ONMV, see section 2.2.1) adopted in the model produces too much CH_2O and hence too much HO_x. The CH_2O profiles observed in the Japan and China-Coast regions during TRACE-P are well reproduced by the model. In Figure 2.35 showing acetone vertical profiles, the calculated vertical distributions of acetone are well within the range of the observations. Acetone mixing ratios are in the range of 500-1000 pptv near the source regions (Japan, China-Coast in PEM-West-B and TRACE-P), and 300-500 pptv over the remote ocean as Philippine-Sea (PEM-West-B) and the central Pacific (PEM-Tropics-B). In the simulation with the previous CHASER version [*Sudo et al.*, 2002b], acetone levels in the tropical Pacific regions during PEM-Tropics-B were underestimated by a factor of 2, but are simulated relatively well in this study with including oceanic acetone emission of 12.0

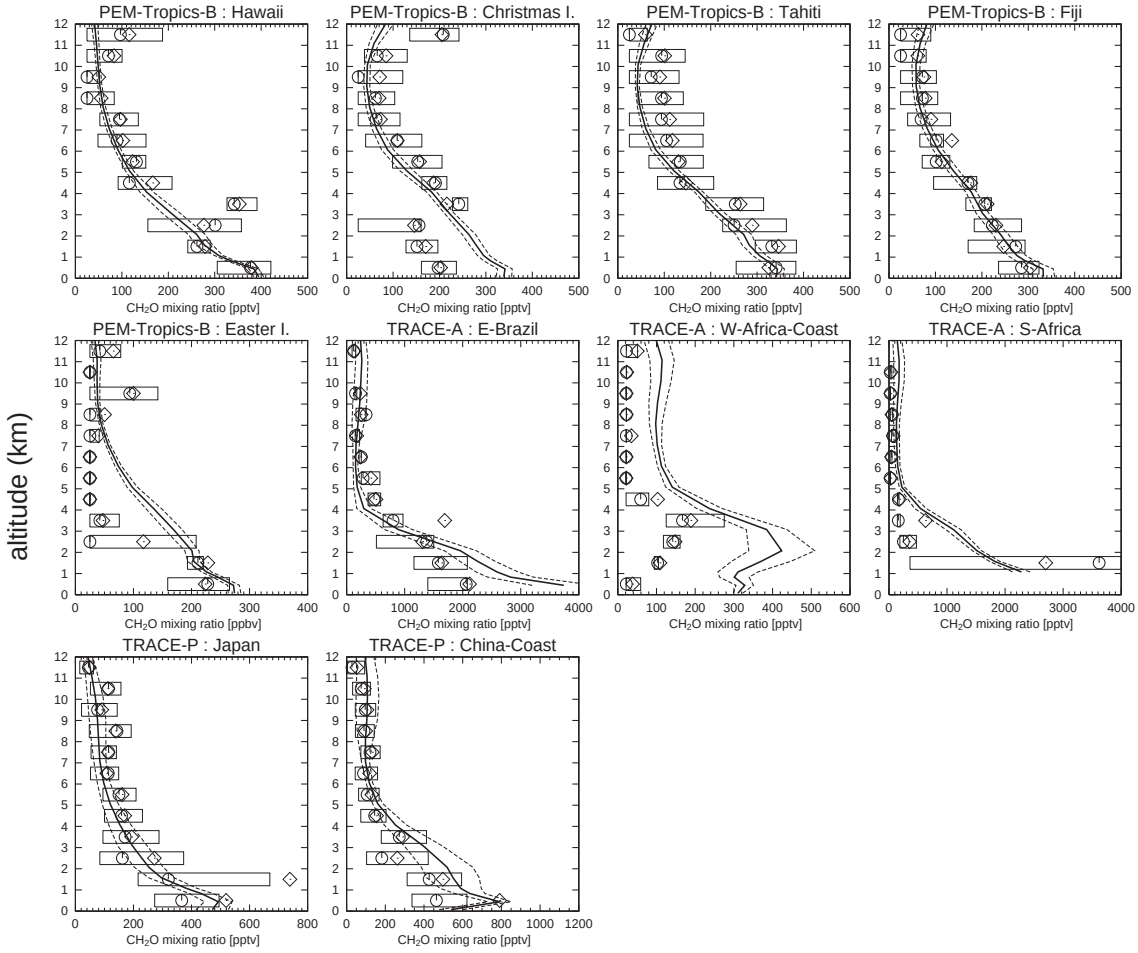

Figure 2.34. CH_2O vertical profiles observed and calculated over the regions of GTE campaigns (listed in Table 2.5). Solid lines and dashed lines show temporal mean and $\pm 1\sigma$ of the model calculation, respectively. The observations show mean (diamonds), median (circles), and inner 50% of the data (boxes).

TgC/yr. The simulated acetone mixing ratio reaches about 1500-2500 pptv in the source regions of biomass burning (E-Brazil and S-Africa). In the E-Brazil region, both the observation and the model show an increase in the upper troposphere, resulting from convective transport [*Fishman et al.*, 1996]. For the TRACE-P expedition, the model reproduces the acetone profiles observed in the Japan and China-Coast regions, simulating the increase below 5 km in China-Coast as with CO (Figure 2.16) and C_2H_6 (Figure 2.20).

To evaluate the seasonal variation of CH_2O and acetone calculated by the model, we display a comparison of seasonal cycle of CH_2O and acetone observed and calculated at the surface for an European site in Figure 2.36. The model appears to reproduce the observed seasonal variation of CH_2O, well simulating the enhancement of CH_2O ($\sim$1.5 ppbv) in summer due to production by the oxidation of methane and NMHCs. The simulated acetone at the surface is also consistent with the observation (1-1.5 ppbv), though the model somewhat underestimates acetone in summer.

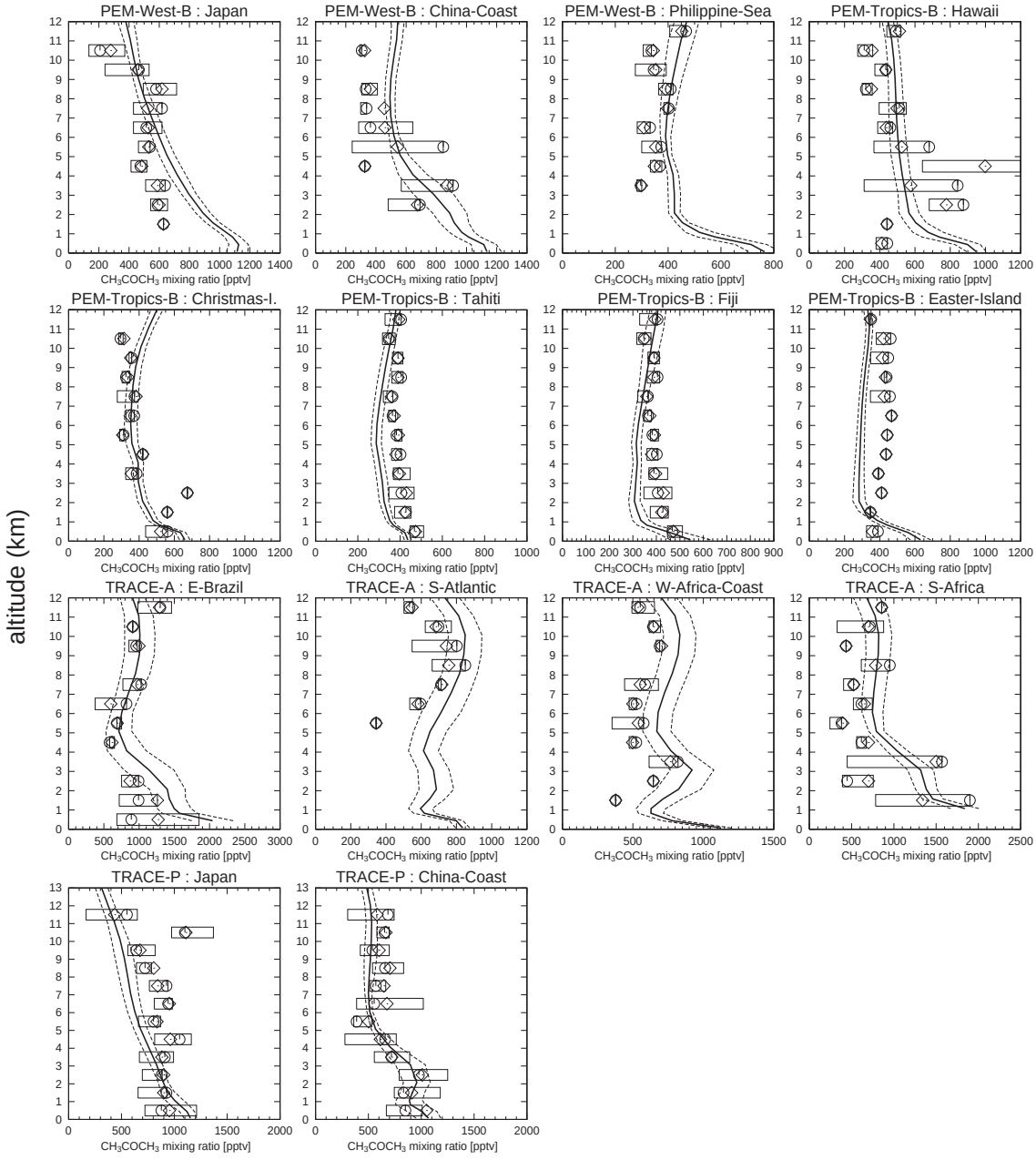

Figure 2.35. Acetone CH_3COCH_3 vertical profiles observed and calculated over the regions of GTE campaigns (listed in Table 2.5). Solid lines and dashed lines show temporal mean and $\pm 1\sigma$ of the model calculation, respectively. The observations show mean (diamonds), median (circles), and inner 50% of the data (boxes).

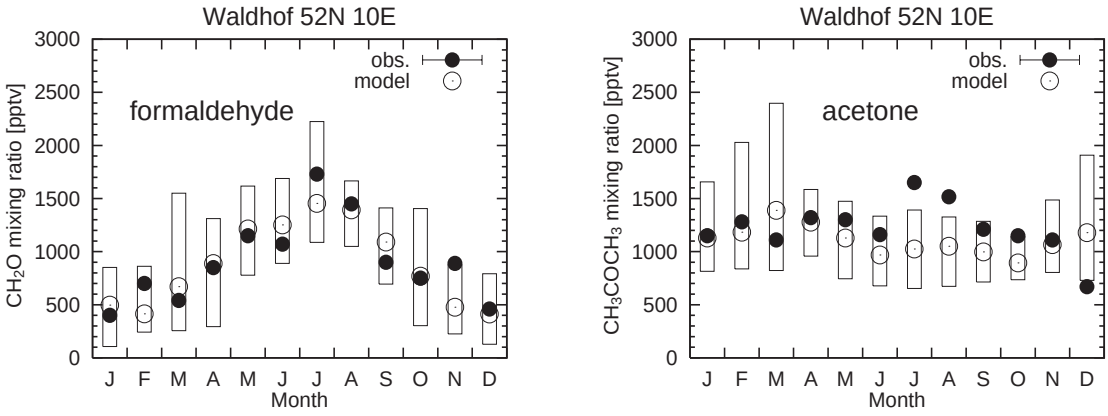

Figure 2.36. Observed (solid circles) and calculated (open circles) surface mixing ratios (pptv) of CH_2O (left) and acetone (right). Boxes indicate the range of the day-to-day variability calculated by the model. Measurements are taken from *Solberg et al.* [1996].

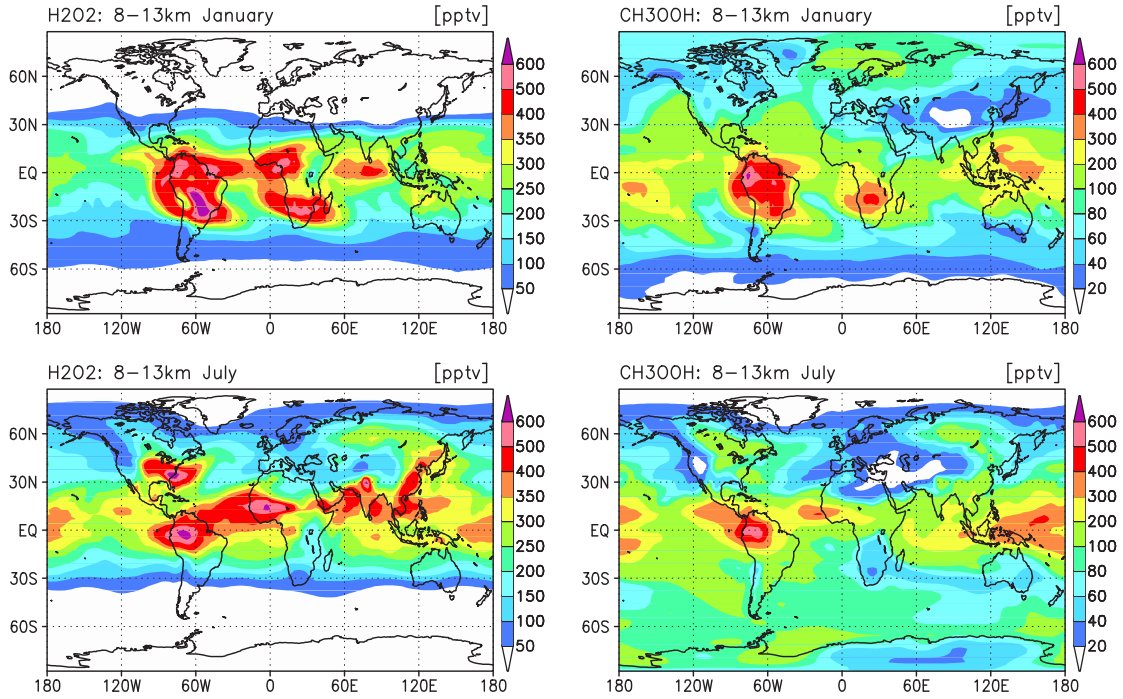

Figure 2.37. Calculated H_2O_2 (left) and CH_3OOH (right) distributions (pptv) in the upper troposphere (averaged over 8-13 km) for January and July.

Peroxides

Peroxides are produced by the reactions of HO_2 with peroxy radicals and decompose by photolysis and OH reaction. Photolysis of peroxides transported to the upper troposphere are considered to be an important HO_x source [*Jaeglé et al.*, 1997; *Folkins et al.*, 1998; *Cohan et al.*, 1999]. Peroxides are, therefore, milestones for simulating the HO_x chemistry. Additionally, H_2O_2 plays a central role in the liquid-phase oxidation of SO_2 to form sulfate (SO_4^{2-}). We focus our attention here on H_2O_2 and CH_3OOH. Figure 2.37 shows the calculated distributions of H_2O_2 and CH_3OOH in the upper troposphere (8-13 km average) for January and July. H_2O_2 and CH_3OOH in the upper troposphere are much more abundant in the tropics (100-600 pptv) than in the extra-tropics (below 100 pptv). The distributions of both H_2O_2 and CH_3OOH show correlation to the distributions of HO_x production in Figure 2.32 as CH_2O and acetone, since H_2O_2 and CH_3OOH, formed by the HO_2 reactions, produce HO_x in the upper troposphere. The high levels of H_2O_2 and CH_3OOH calculated over South America and Africa (higher than 500 pptv) are owing to in-situ production of peroxides in the upper troposphere and convective transport of H_2O_2 and CH_3OOH overcoming wet deposition of them.

Figure 2.38 shows the calculated zonal mean distributions of H_2O_2 and CH_3OOH in the annual

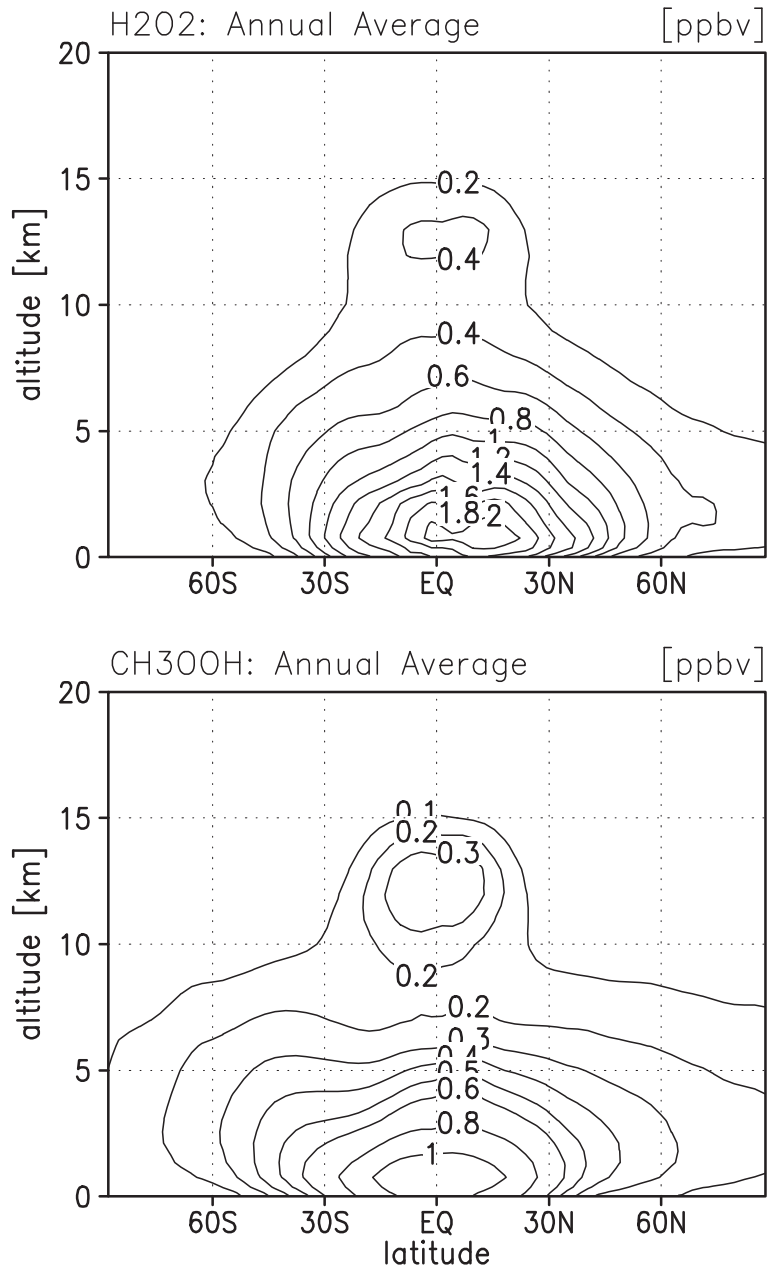

Figure 2.38. Zonal mean distributions (ppbv) of H_2O_2 and CH_3OOH in the annual average.

average. Though H_2O_2 is removed by wet deposition more efficiently than CH_3OOH, the calculated H_2O_2 concentration is generally higher than CH_3OOH as suggested by measurements [e.g., *Talbot et al.*, 1996; *Heikes et al.*, 1996]. The distributions of both H_2O_2 and CH_3OOH show a peak near the surface ($\sim$1 km) in the tropics ($H_2O_2\sim$ 2 ppbv, $CH_3OOH\sim$1 ppbv). Peaks of H_2O_2 and CH_3OOH are also calculated in the tropical upper troposphere. Although these peaks seem to be consistent with convective transport of H_2O_2 and CH_3OOH in the tropics, they may be overestimated by the model because the model probably overestimates the HO_2/HO ratio due to underestimation of NO

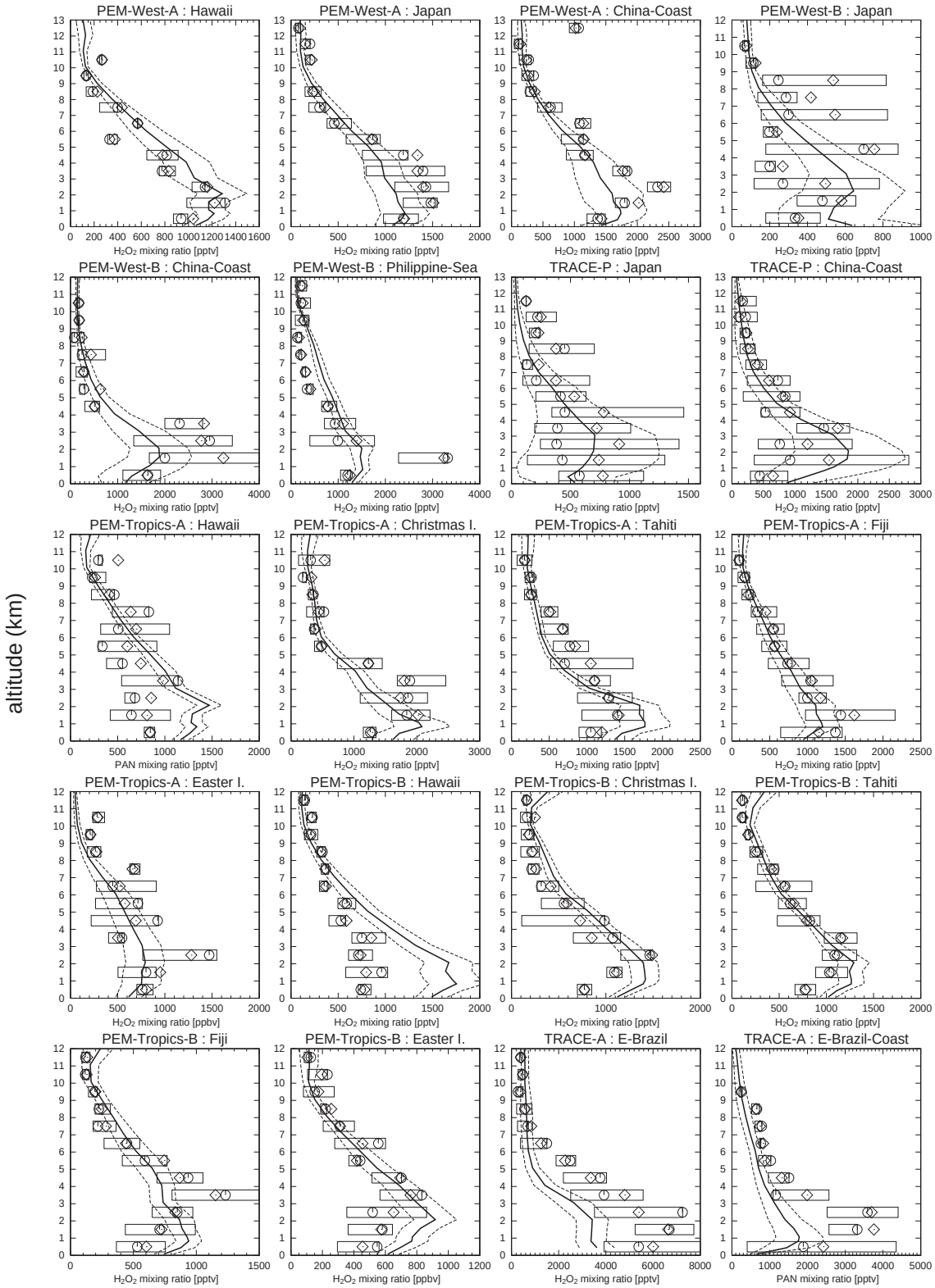

Figure 2.39. H_2O_2 vertical profiles observed and calculated over the regions of GTE campaigns (listed in Table 2.5). Solid lines and dashed lines show temporal mean and $\pm 1\sigma$ of the model calculation, respectively. The observations show mean (diamonds), median (circles), and inner 50% of the data (boxes).

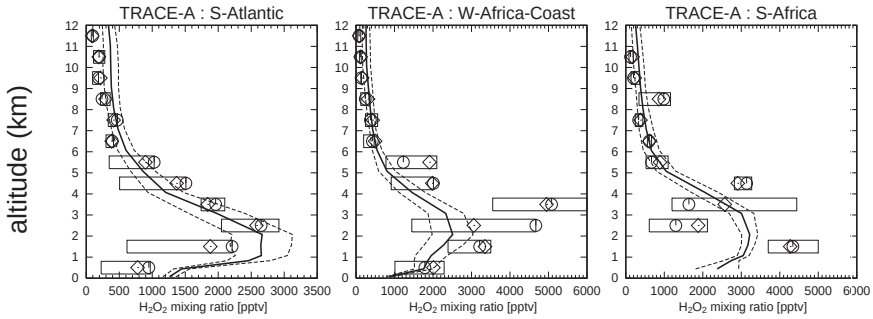

Figure 2.39. (continued).

in the tropical upper troposphere.

In Figure 2.39, the observed and the calculated vertical profiles of H_2O_2 are compared. The model reproduces the observed H_2O_2 profiles very well in most cases. In the Japan region during both PEM-West-B and TRACE-P, the observation shows high variabilities of H_2O_2 (ranging from 100 to 1000 pptv) below 9 km. The model also shows large standard deviations ($\pm 1\sigma$) over this region, calculating H_2O_2 levels well consistent with the observation. The H_2O_2 increase in 1-5 km altitudes in the China-Coast region during TRACE-P is well reproduced by the model and is resulting from the abundant HO_2 in the region (Figure 2.31). The previous CHASER version [*Sudo et al.*, 2002b] tends to overestimate H_2O_2 in the upper troposphere above 9 km in the tropical regions for PEM-Tropics-A and B. Such an overestimation appears to be reduced in this simulation by including H_2O_2 deposition on ice particles in cirrus clouds (see section 2.2.3). In the biomass burning regions in South America (E-Brazil in TRACE-A), the model underestimates the observed H_2O_2 by a factor of 2 below 5 km. This discrepancy would be reduced by considering methanol emissions from vegetation and biomass burning as suggested by *Horowitz et al.* [2002]. In the S-Atlantic region, both the observation and the model show high level of H_2O_2 ($\sim$2000 pptv) in 1-4 km altitudes, associated with the African outflow. Figure 2.40 is the same as Figure 2.39 but for CH_3OOH profiles. CH_3OOH profiles are captured well by the model as well as H_2O_2. Over the China-Coast and the Philippine-Sea regions during PEM-West-B, the model overestimates CH_3OOH in the middle-upper troposphere by a factor of $\sim$2, with showing good agreement with the observations for H_2O_2 (Figure 2.39). This may indicate overestimation of methyl peroxy radical (CH_3O_2) and hence too strong formation of CH_3O_2 by the oxidation of NMHCs around these regions. In the tropical regions (PEM-Tropics), the simulated profiles of CH_3OOH are well consistent with the observations, calculating mixing ratios of $\sim$1 ppbv near the surface and 100-300 pptv in the upper troposphere. In the biomass burning regions (TRACE-A), CH_3OOH in the upper troposphere is somewhat overestimated, though CH_3OOH in the lower-middle troposphere (500-1000 pptv) is well simulated.

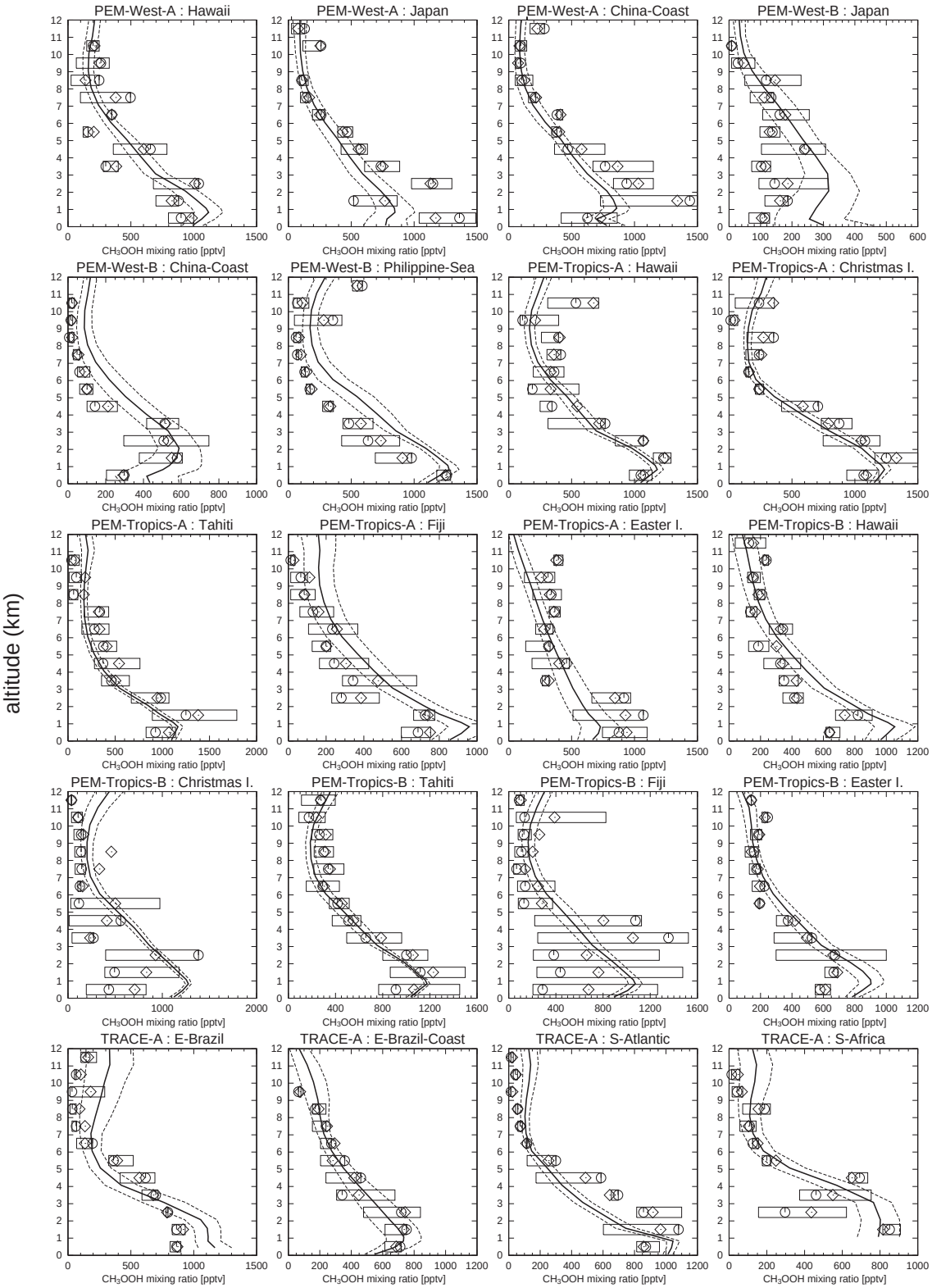

Figure 2.40. CH_3OOH vertical profiles observed and calculated over the regions of GTE campaigns (listed in Table 2.5). Solid lines and dashed lines show temporal mean and $\pm 1\sigma$ of the model calculation, respectively. The observations show mean (diamonds), median (circles), and inner 50% of the data (boxes).

2.3.4 Ozone

Distributions

Figure 2.41 shows the surface O_3 distributions calculated for 4 different seasons. In January, high concentration of O_3 (50-60 ppbv) is calculated in India, owing to industrial emissions of O_3 precursors. High O_3 levels ($\sim$60 ppbv) are also seen in the biomass burning region in North Africa. O_3 concentration in the midlatitudes ranges from 30 to 40 ppbv over the ocean in the northern hemisphere, as a result of longer chemical lifetime of O_3 in winter and transport from the stratosphere. The calculated stratospheric ozone distribution at the surface indicates a 40-50% contribution by stratospheric ozone to the surface O_3 abundance in the northern midlatitudes in January. In April, the O_3 chemistry is activated in the northern hemisphere. High O_3 levels (50-65 ppbv) are predicted in eastern Asia as India, China, and Japan, affected by intense UV radiation and surface emissions by industry and biomass burning. Ozone produced in eastern Asia and Japan is transported to the western Pacific. In July, O_3 is much abundant in the United States and in the central Eurasia including Europe, ranging from 50 to 70 ppbv. High O_3 level associated with biomass burning is seen in the western edge of Africa. The effect of biomass burning on the surface O_3 is clearly visible in October over South America and Africa (50-60 ppbv). The model calculates low concentrations of O_3 (10-15 ppbv) in Amazonia through a year, resulting from strong ozone destruction by biogenic NMHCs and from strong dry deposition (deposition velocities of $\sim$1 cm s^{-1} in the model).

Similar features are also visible in the distributions of tropospheric column ozone TCO (Figure 2.42). TCO calculated by the model shows the ozone column integrated from the surface to the physically defined tropopause in the model (defined as the lowest altitude at which the vertical temperature gradient is greater than -2 K/km). Abundant tropospheric ozone in the range of 35-50 DU is calculated in the low to midlatitudes in both hemisphere due to industrial and biomass burning emissions. In July, the model calculates an O_3 peak of 45-50 DU around the Middle East, arising from transport of pollutants from the northern midlatitudes and eastern Asia and NO_x emissions from lightning as suggested by *Li et al.* [2001]. A large O_3 enhancement (>40 DU) is seen over the South Atlantic in October in accordance with biomass burning emissions in South America and Africa. The O_3 enhancement is also extending over the Indian Ocean ($\sim$40 DU) as a plume toward Australia. For all seasons, the model calculates an O_3 peak over the Atlantic with a minimum around the western Pacific (the wave 1 pattern) in the tropical latitudes, associated with the large-scale Walker circulation, lightning NO_x emissions, and biomass burning in the tropics. The wave 1 like pattern in zonal ozone distribution declines rapidly with latitude in the extratropics. This feature of tropical tropospheric ozone distribution is derived also by many satellite-based observations [e.g., *Fishman and Larsen*, 1987; *Fishman et al.*, 1996; *Ziemke et al.*, 1998] (see chapter 4). The model, however, tends to overestimate O_3 abundance around the North Atlantic, North Africa, and India compared to the satellite observations, especially in January to April.

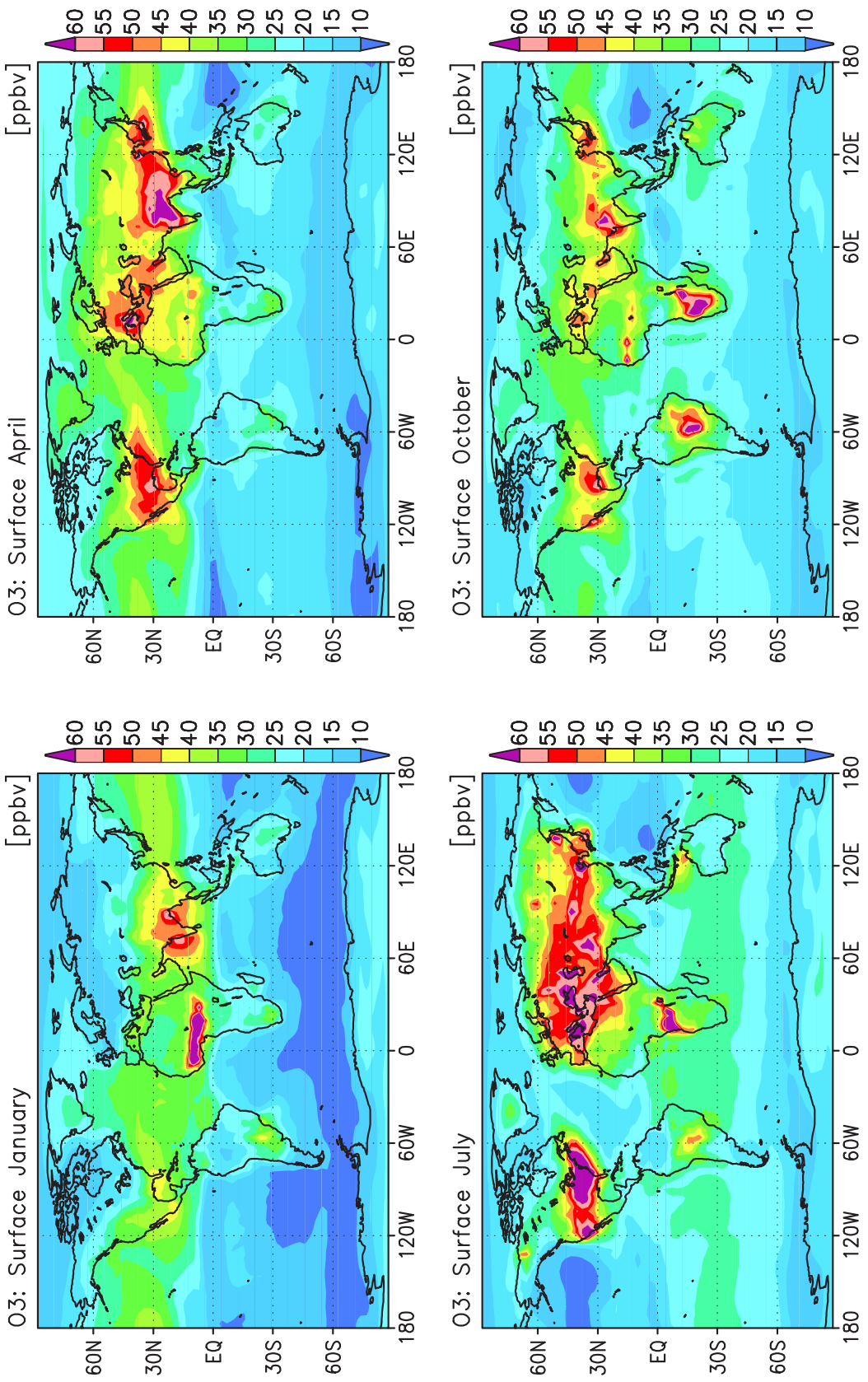

Figure 2.41. Calculated O_3 distributions (ppbv) at the surface for 4 distinct seasons (indicated).

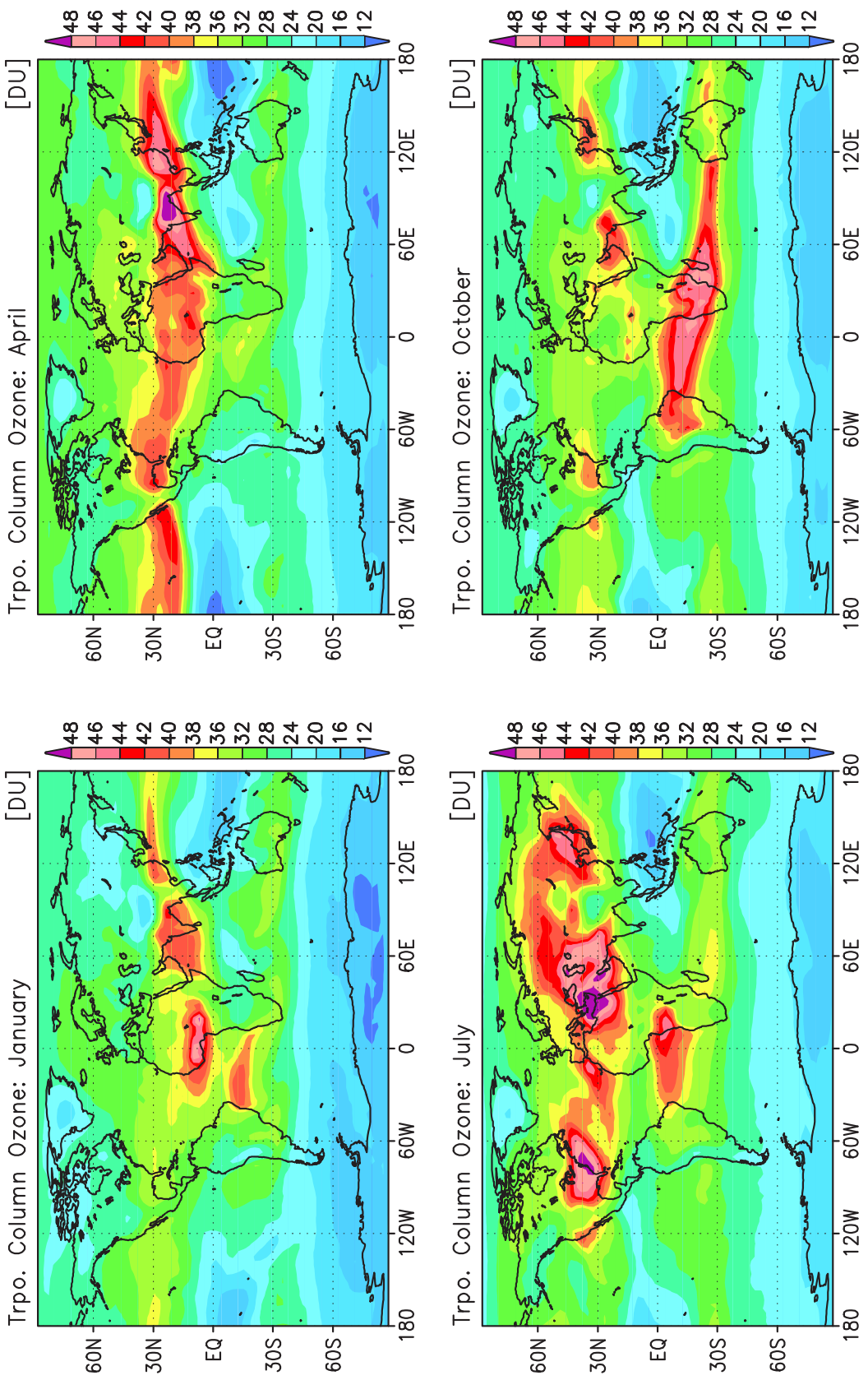

Figure 2.42. Tropospheric column ozone (TCO in Dobson Units) calculated for 4 distinct seasons (indicated).

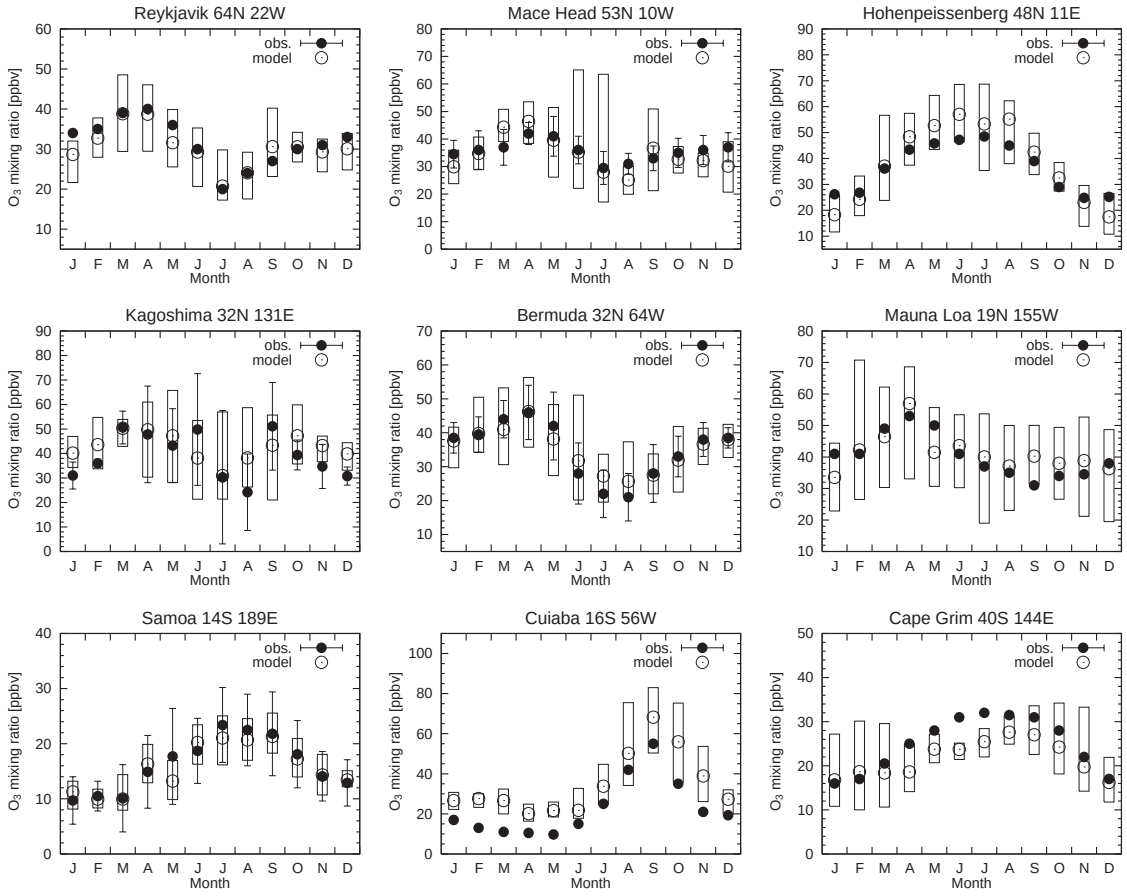

Figure 2.43. O_3 seasonal variations observed (solid circles) and calculated (open circles with boxes showing the range) at the surface for several sites. Measurements are from *Oltmans and Levy* [1994], *Kirchhoff et al.* [1989] (for Cuiaba) , and *Logan* [1999] (for Kagoshima).

Figure 2.43 compares the calculated seasonal cycle of surface O_3 with observations. The observations are mainly from *Oltmans and Levy* [1994]. The model well simulates the observed seasonal cycle of surface O_3 characterized by spring-maximum in the remote regions (Reykjavik, Mace Head, Bermuda, Mauna Loa, Samoa, Cape Grim) and summer-maximum in the polluted source regions (Höhenpeissenberg). The spring ozone peak at Bermuda is closely associated with the outflow from the United States in the model. Similarly, the peak in April at Mauna Loa is much related to the Asian outflow and to the transport of stratospheric ozone. For Cuiaba in the biomass burning region in South America, the model well reproduces the observed seasonal cycle (September maximum) associated with biomass burning as well as CO (Figure 2.15). The simulated O_3 levels in Cuiaba are, however, somewhat higher than the observation through a year, maybe indicating the underestimation of O_3 deposition velocity, or the overestimation of soil NO_x emission around Cuiaba. Similar overestimation at this site is also found in a previous modeling study [*Roelofs and Lelieveld*, 2000]. For Samoa and Cape Grim, the model reproduces the observed seasonal varia-

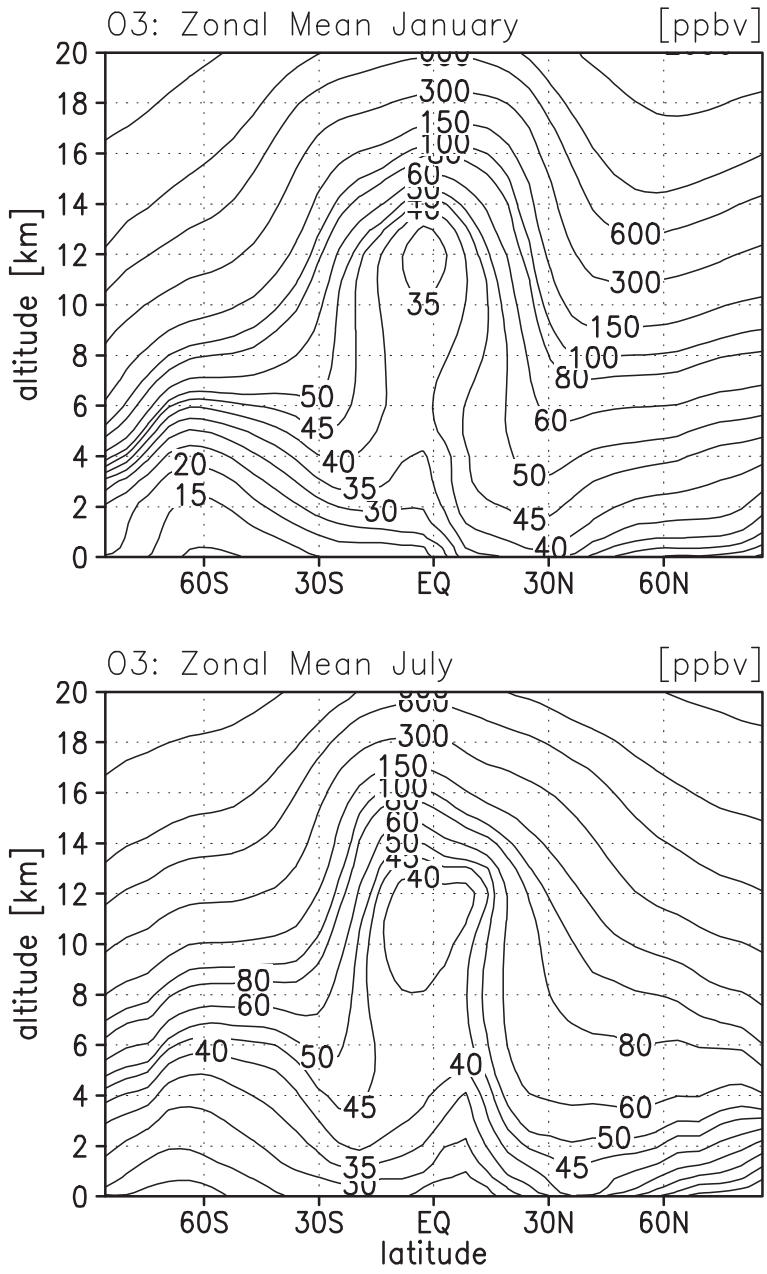

Figure 2.44. Zonally averaged ozone mixing ratios (ppbv) calculated for January and July.

tions associated with chemical lifetime of O_3 and transport from the stratosphere, though it slightly underestimates O_3 in June and July for Cape Grim.

Figure 2.44 shows the zonal mean O_3 distributions calculated for January and July. In both seasons, the model calculates low O_3 levels (30-40 ppbv) in the tropics due to short chemical lifetime of O_3 and convective activity. In January, O_3 concentration is high in the middle-upper troposphere in the northern midlatitudes, associated with transport from the stratosphere. In July, the model calculates high O_3 concentrations in the northern hemisphere through much of the troposphere, reflecting

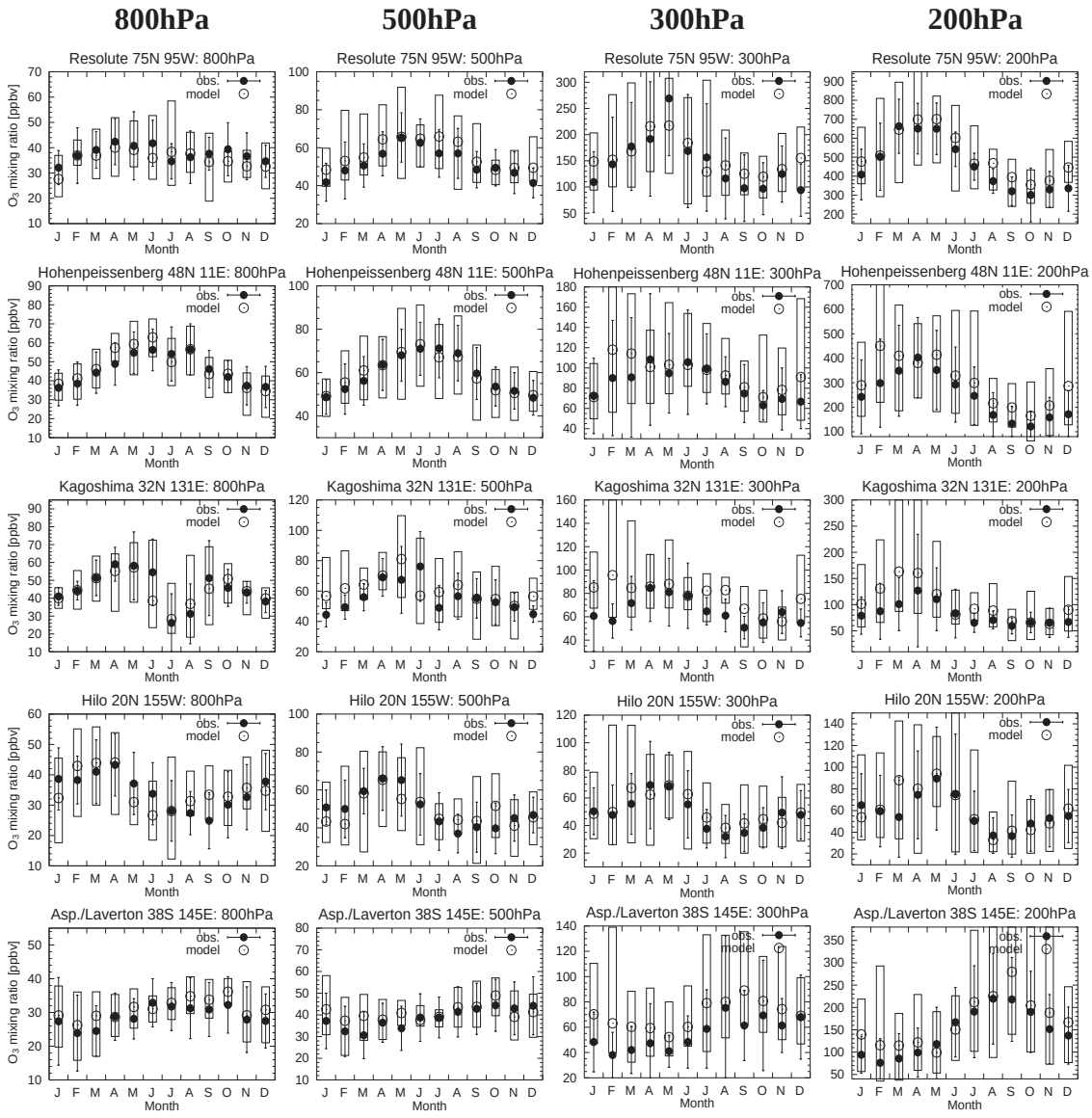

Figure 2.45. O_3 seasonal variations observed (solid circles) and calculated (open circles with boxes showing the range) at different elevations. Observations are taken from *Logan* [1999].

intensive photochemical production of O_3 in summer. In the southern hemisphere, the model calculates low mixing ratios of ozone (10-20 ppbv) near the surface in January, and calculates higher ozone concentrations (25-35 ppbv) in July associated with transport from the stratosphere.

In Figure 2.45, the seasonal variations of O_3 calculated at distinct altitudes are compared with the ozonesonde data compiled by *Logan* [1999]. The model generally well reproduces the observed seasonal cycles of O_3 at individual altitudes. At Resolute, the observed and the calculated O_3 at 200 hPa reach a peak (600-700 ppbv) in spring, associated with the stratospheric O_3 transport. Similar spring maximum is observed at 200 hPa over Höhenpeissenberg, overestimated slightly by the model, though. O_3 seasonal variation at Höhenpeissenberg shows a summer maximum from

800 hPa to 300 hPa, indicating considerable chemical production of O_3 over Europe in summer. At Kagoshima in the southern Japan, the model well captures the summertime minimum (rapid decrease in July and August) observed at 800 hPa. This minimum is associated with the shift in the airmass origin. The airmass at Kagoshima is maritime in summer and is continental in winter-spring, much influenced by the Asian outflow. At 300 and 200 hPa over Kagoshima, the model overestimates O_3 in winter by a factor of 2, indicating too much transport from the stratosphere. At Hilo, the model well reproduces the observed seasonal variations at individual altitudes, capturing spring O_3 peaks. At Laverton in the southern hemisphere, the model captures the seasonal variation of ozone observed at 200 hPa, well reproducing the ozone peak (200-250 ppbv) in spring associated with the stratospheric ozone transport, though the model overestimates the observed ozone levels at 300 hPa through a year. In winter-spring, the model tends to overestimate O_3 in the upper troposphere in the midlatitudes in both hemispheres, probably resulting from overestimation of O_3 transport from the stratosphere.

Additionally, calculated vertical profiles of O_3 are compared with the observational data [*Logan*, 1999] in Figure 2.46. The calculated profiles are generally well consistent with the observations. At Hilo, the model tends to overestimate O_3 in the upper troposphere especially in December-January-February (DJF) and March-April-May (MAM). We note that both the observation and the model show high temporal variabilities (indicated by the standard deviations) in the upper troposphere at Hilo, in winter-spring (DJF and MAM). At Natal located in the eastern coast of Brazil, the model reproduces the increase in O_3 ($\sim$70 ppbv) in 800-300 hPa in September-October-November (SON) associated with biomass burning. The model, however, appears to slightly overestimate O_3 in the middle troposphere at Natal in MAM and JJA. At Samoa, the observed seasonal cycle of ozone profile showing maximum in spring (SON) is well simulated by the model. The model well captures also the decrease of O_3 observed in the tropical lower troposphere (Naha, Hilo, Natal, and Samoa) related to the trade wind inversion in the tropics [*Heikes et al.*, 1996; *Logan*, 1999].

The calculated O_3 vertical profiles are also evaluated with the NASA GTE campaign data (Table 2.5) in Figure 2.47. In the Alaska (ABLE-3A), Ontario, and US-E-Coast regions, the calculated profiles are well consistent with the campaign measurements. The O_3 profile in the Japan region is well simulated by the model during PEM-West-A (September-October), but is overestimated significantly in the middle-upper troposphere during PEM-West-B (February-March) due to the overestimation of transport of stratospheric O_3 in the midlatitudes. A similar overestimation is also found during TRACE-P in the region. A slight overestimation of ozone is also found in the middle troposphere over the China-Coast region (PEM-West-B). This overestimation by the model can be also attributed to the overestimation of the stratospheric ozone transport, since the photochemical production rates of ozone calculated for this region during PEM-West-B are well consistent with the box model calculation constrained by the observation (see Figure 2.49). In the tropical regions (PEM-Tropics-A and B), the model well simulates the observed profiles of O_3, capturing

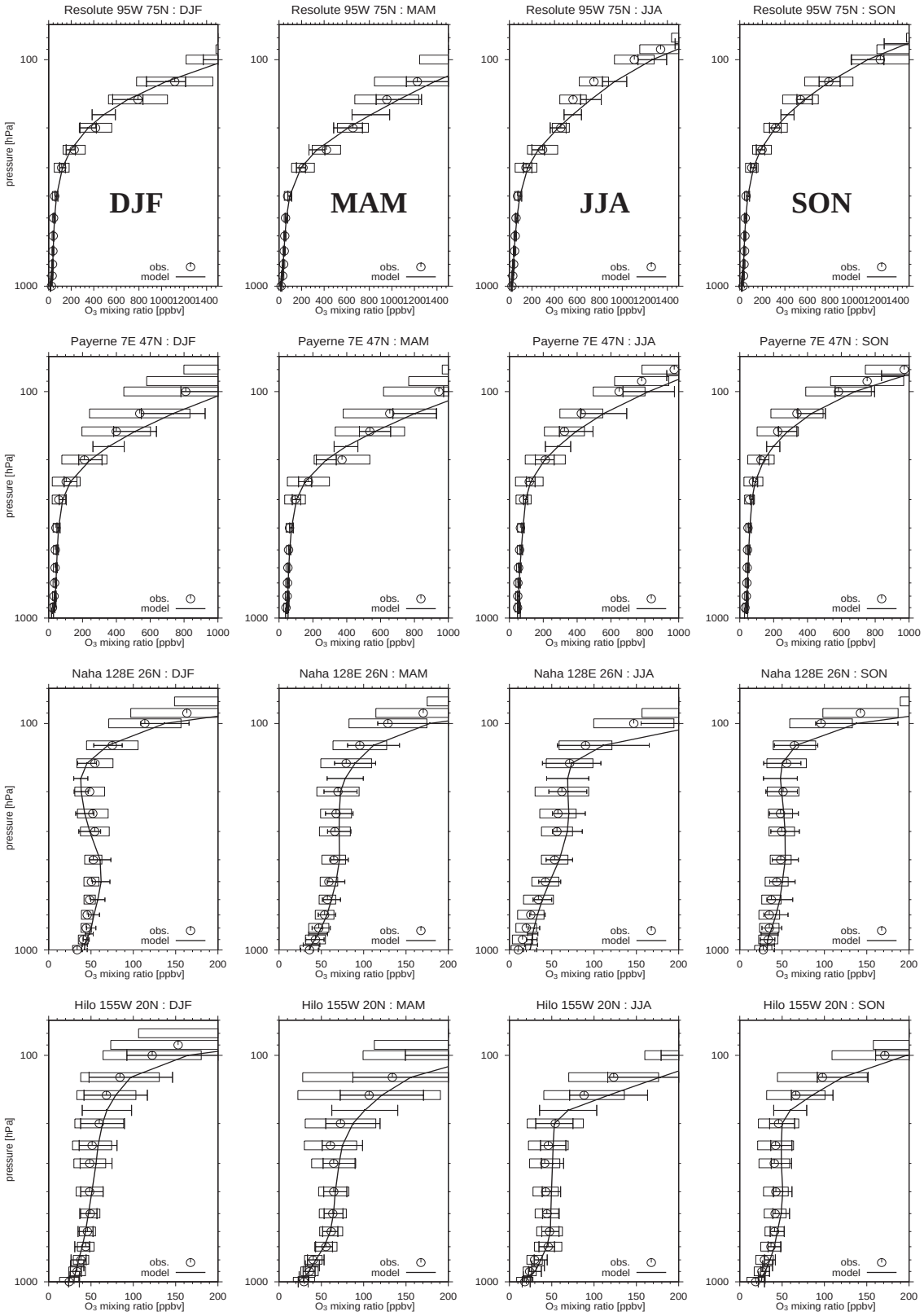

Figure 2.46. O_3 vertical profiles observed (open circles) and calculated (solid lines with $\pm\sigma$ bars) at several stations for 4 different seasons. Boxes show the standard deviations of observations. Observations are taken from *Logan* [1999].

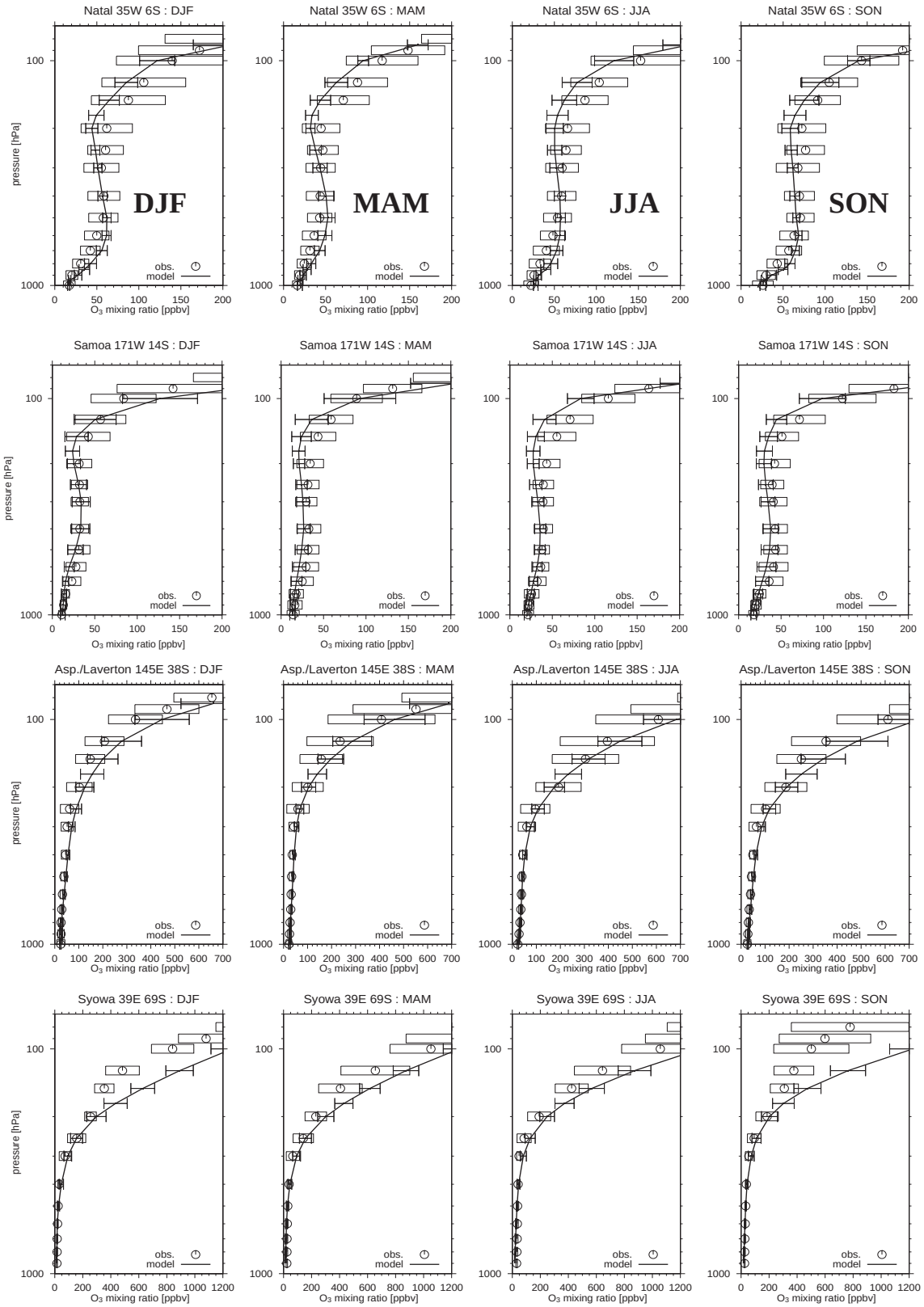

Figure 2.46. (continued).

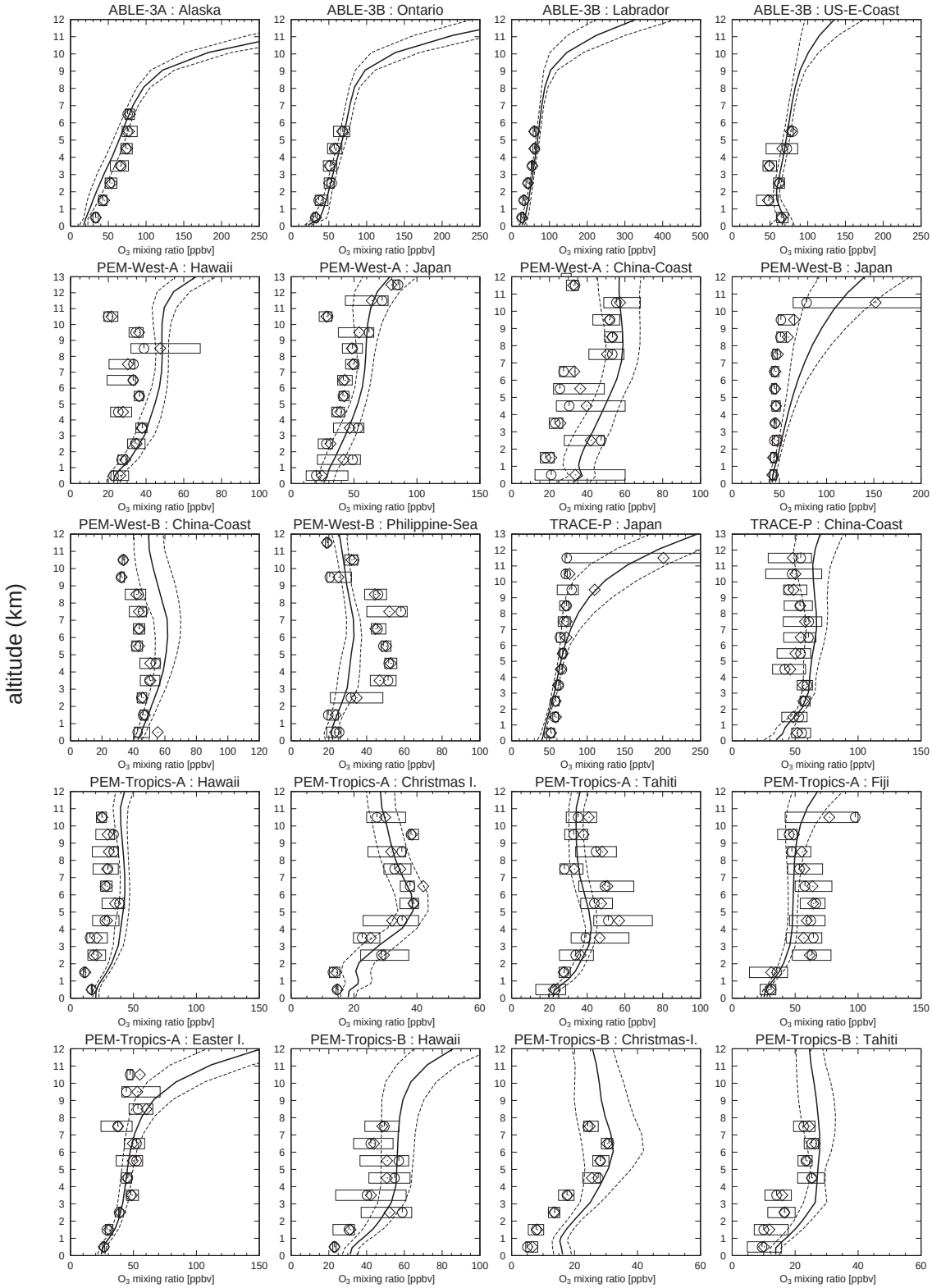

Figure 2.47. O_3 vertical profiles observed and calculated over the regions of GTE campaigns (listed in Table 2.5). Solid lines and dashed lines show temporal mean and $\pm 1\sigma$ of the model calculation, respectively. The observations show mean (diamonds), median (circles), and inner 50% of the data (boxes).

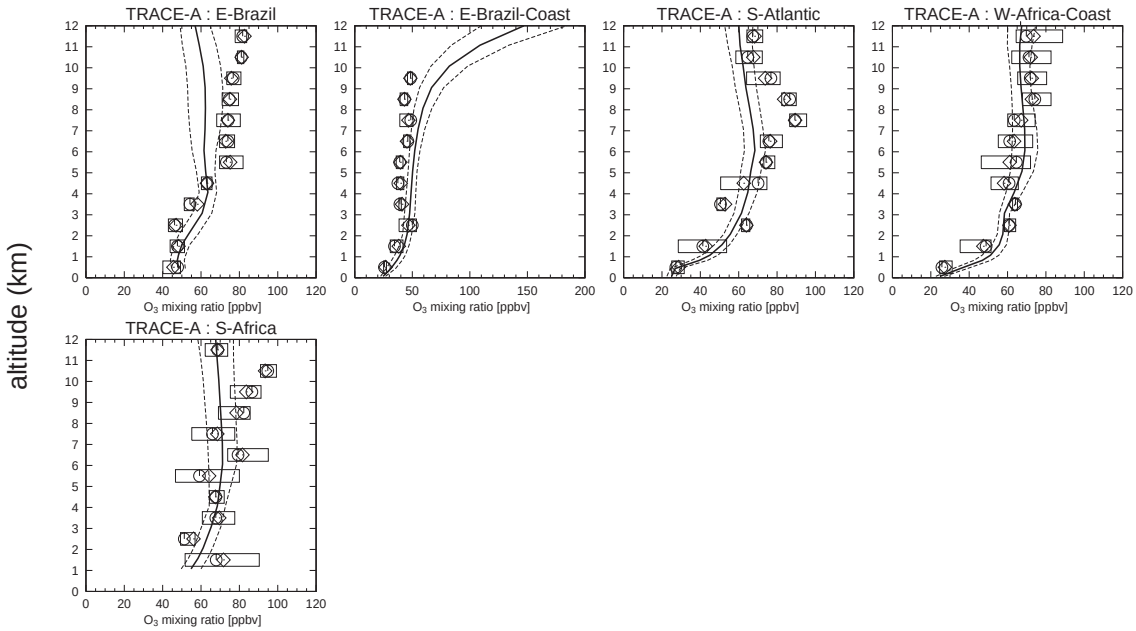

Figure 2.47. (continued).

the rapid decrease in 0-5 km. For TRACE-A, the model reproduces the enhanced O_3 levels in the middle-upper troposphere due to biomass burning in South America and Africa. The model, however, underestimates the O_3 increase above 5 km over the E-Brazil region, probably caused by the underestimation of NO_x in the upper troposphere over this region (Figure 2.24). A rapid decrease in O_3 concentrations near the surface ($\sim$20 ppbv at the surface) is also well simulated by the model for the S-Atlantic region and the W-Africa-Coast region.

Budget

There are two kind of sources for tropospheric ozone. One is the transport of ozone associated with the stratosphere-troposphere exchange (STE), and the other is the in-situ photochemical production in the troposphere due to the reaction of NO with peroxy radicals and the subsequent photolysis of NO_2. Loss of tropospheric ozone is mainly by photochemical destruction due to the reaction of atomic oxygen (singlet) $O(^1D)$ with water vapor ($O(^1D)$ + H_2O) and the subsequent reactions (i.e., O_3 + OH and O_3 + HO_2), and by dry deposition at the surface. Transport of ozone to the stratosphere associated with the STE is also loss of tropospheric ozone.

Figure 2.48 shows the distributions of the 24-hour averaged net chemical production $P(O_y)-L(O_y)$ calculated at the surface and in the upper troposphere (8-13km average) for January and July. O_y is the conventionally defined odd oxygen family and indicates $O_3 + O(^1D) + NO_2 + 2NO_3 + 3N_2O_5 + PAN + MPAN + 2HNO_3 + HNO_4 + ISON + NALD$ in this simulation (ISON=isoprene nitrates, NALD=nitrooxy acetaldehyde, see section 2.2.1). The budget of O_y is

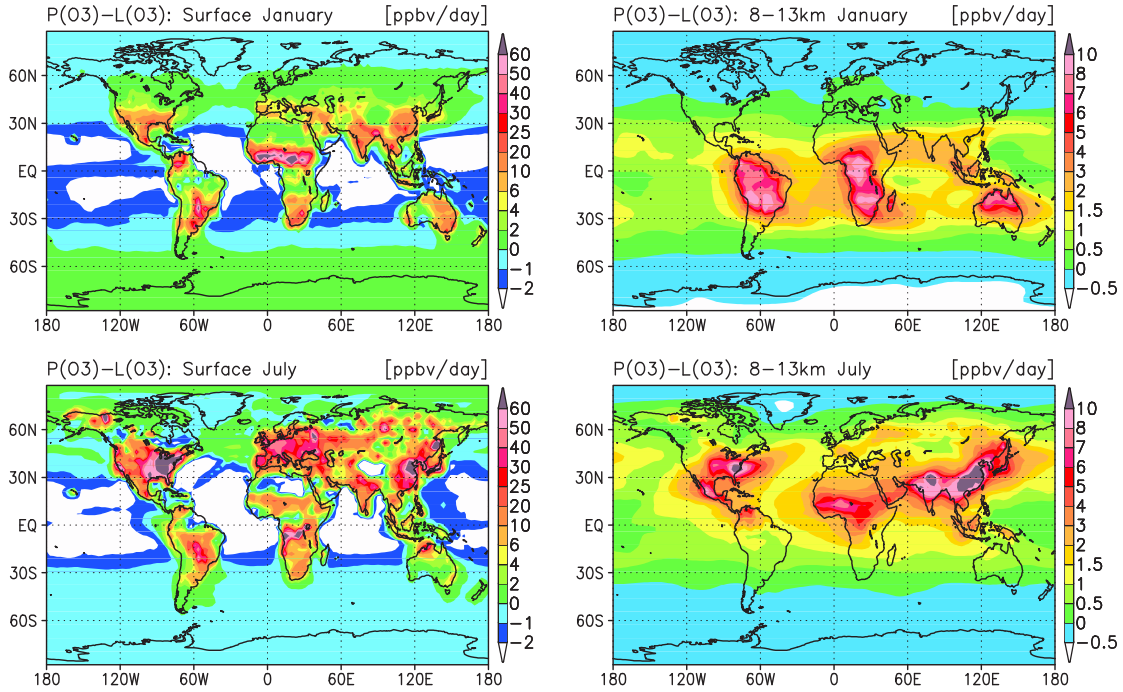

Figure 2.48. Calculated distributions of the net chemical production of ozone (ppbv/day) at the surface (left) and in the upper troposphere (8-13 km) (right) for January and July.

almost identical to that of ozone. The model calculates intensive ozone production in the polluted areas at the surface for both seasons. In January, ozone production rates of 30-50 ppbv/day are calculated over North Africa, associated with biomass burning. The model predicts relatively strong ozone production (6-15 ppbv/day) in the southern United States and eastern Asia, and also calculates positive production (0-2 ppbv/day) in the northern high latitudes (45-60°N) in spite of reduced UV radiation. In July, the net ozone production at the surface is most intense in the eastern United States, Europe, and eastern Asia (30-70 ppbv/day) owing to industrial emissions of ozone precursors. The net ozone production over the ocean is generally negative (ozone destruction). In the upper troposphere, the model calculates positive net ozone production through much of the low-mid latitudes. In January, high ozone production rates (3-8 ppbv/day) are calculated over South America, Africa, and the northern Australia, due to lightning NO_x and convective transport of biogenic emissions of NMHCs. Strong ozone production ($\sim$8 ppbv/day) over North Africa is associated with convective transport of biomass burning emissions. The net ozone production calculated for July also displays the effect of surface emissions, convective transport, and lightning NO_x on the ozone budget in the upper troposphere. Intensive ozone production (8-10 ppbv/day) is calculated over the southern United States and eastern Asia extending over the western Pacific including Japan (2-5 ppbv/day).

Ozone production and loss rates have been calculated for several of the aircraft campaigns, us-

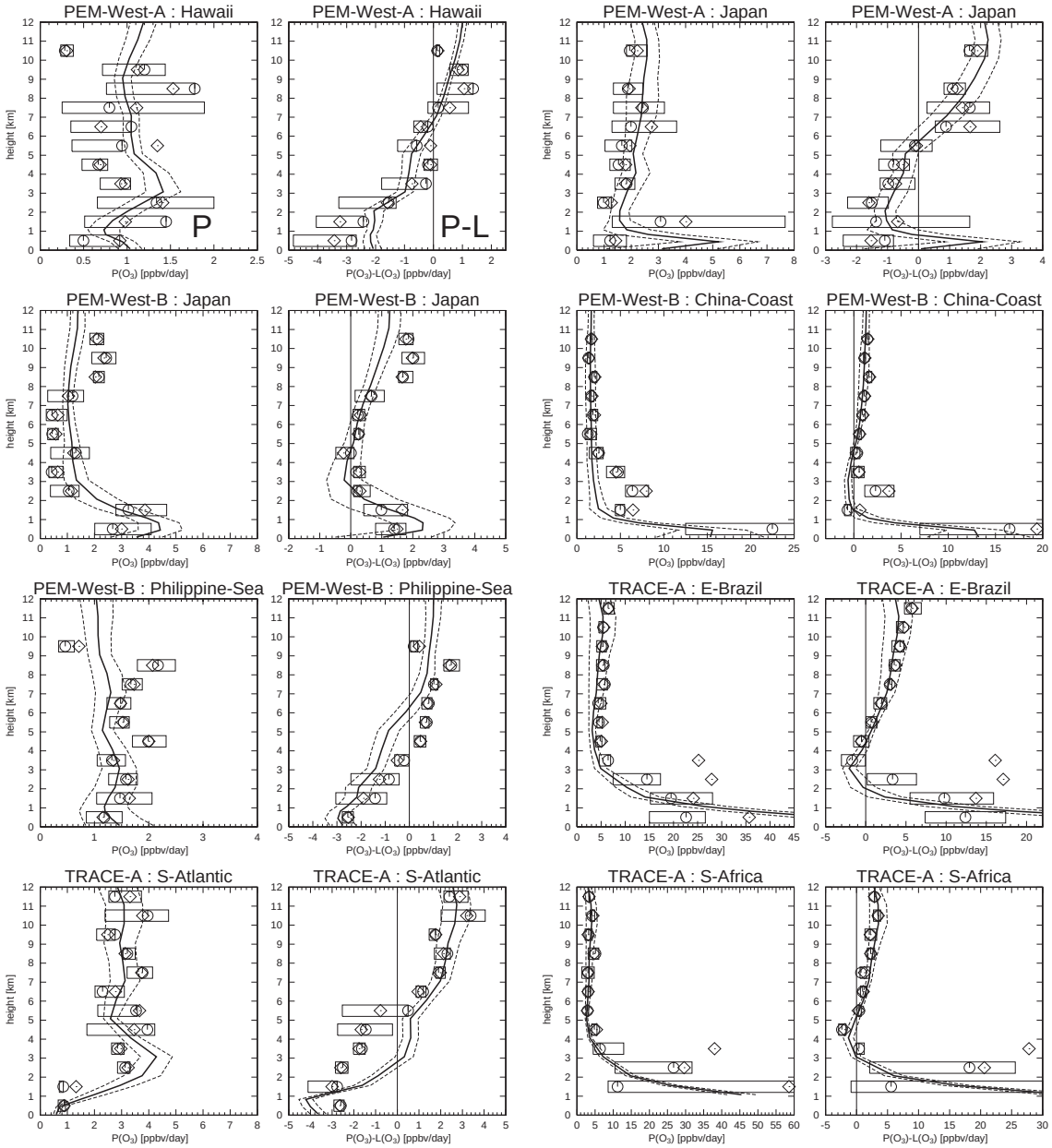

Figure 2.49. Vertical profiles of the ozone production $P(O_3)$ and the net production $P(O_3)$-$L(O_3)$ derived from observations and calculated by CHASER over the regions of GTE campaigns (listed in Table 2.5). Solid lines and dashed lines show temporal mean and $\pm 1\sigma$ of the model calculation, respectively. The observations show mean (diamonds), median (circles), and inner 50% of the data (boxes).

ing photochemical box (0-dimensional) models constrained by observations [e.g., *Crawford et al.*, 1996, 1997; *Schultz et al.*, 1999]. We compare the calculated ozone production rates with these observation-derived ozone production rates. Figure 2.49 shows the vertical profiles of the ozone chemical production $P(O_y)$ and the net chemical production $P(O_y)$-$L(O_y)$ derived from the GTE campaign measurements [*Crawford et al.*, 1996, 1997] and calculated by CHASER. The values

show the 24-hour averaged ozone production and net production. In Hawaii (PEM-West-A), the calculated $P(O_y)$ ranges from 0.5-1.5 ppbv/day, well within the range of the constrained box model calculation (BMC, hereafter). The calculated net ozone production $P(O_y)$-$L(O_y)$ is also consistent with the BMC, well reproducing the net ozone production (0-1.5 ppbv/day) above $\sim$7 km. In the Japan region during PEM-West-A (September-October), the model well simulates the ozone production (1.5-3 ppbv/day) in the free troposphere, and also reproduces the decrease in the net production below 7 km (net ozone destruction) reflecting the shorter lifetime of ozone in the lower troposphere. The ozone production near the surface is, however, overestimated by a factor of 5. During the PEM-West-B expedition (February-March), the model calculates vertical profiles consistent with the BMC over the Japan region below 8 km for both $P(O_y)$ and $P(O_y)$-$L(O_y)$. The model does not capture the high rates of ozone production and net production ($\sim$2 ppbv/day) in the upper troposphere above 8 km. In the China-Coast region, the model well simulates profiles of $P(O_y)$ and $P(O_y)$-$L(O_y)$, calculating high net ozone production rates ($\sim$2 ppbv/day) in the upper troposphere. Intense ozone production near the surface (15-20 ppbv/day) is also reproduced. In the Philippine-Sea region, the net ozone production appears to be underestimated by 1-2 ppbv/day, though the calculated ozone production $P(O_y)$ is well consistent with the BMC (1-2 ppbv/day). This may indicate the overestimation of water vapor leading to overestimation of ozone loss over this region. Over the source regions of biomass burning (E-Brazil and the S-Africa), the high production rates (3-5 ppbv/day) in the upper troposphere derived by the BMC are also reproduced by CHASER. The profiles of ozone production $P(O_y)$ show almost constant rates (3-5 ppbv/day) in the free troposphere above 3 km with high rates in the boundary layer (15-50 ppbv/day). Both the BMC and CHASER calculations display steep decrease in the net ozone production with altitude in the boundary layer and increase in the free troposphere, with showing slight negative rates above the top of boundary layer (3-5 km). Over the S-Atlantic region, ozone production rates calculated in the upper troposphere ($\sim$2 ppbv/day) are consistent with the BMC. The net ozone production rates in 2-6 km altitudes are, however, overestimated by CHASER by 1-2 ppbv/day, caused partly by the overestimation of ozone production in 2-4 km, and also by the underestimation of water vapor over the South Atlantic (not verified).

In Table 2.9, the global annual budget of tropospheric ozone (O_y) calculated by the model is presented. The model calculates a global ozone chemical production of 4746 TgO_3/yr (62% in the northern hemisphere). The reactions of NO with HO_2 and CH_3O_2 are main production , contributing to the total ozone production for 64% and 22%, respectively. The remainder (14% of the total ozone production) is due to the reactions of NO with peroxy radicals formed by the oxidation of NMHCs. The reaction of HO_2 with CH_3COO_2 also makes a slight contribution to the ozone production in the model. The simulation with the previous version of CHASER [*Sudo et al.*, 2002b] suggested that heterogeneous reactions (uptake) of HO_2 and peroxy radicals (RO_2) formed by oxidation of isoprene and terpenes [e.g., *Walcek et al.*, 1997; *Horowitz et al.*, 1998; *Jacob*, 2000]

Table 2.9. Global Budget of Tropospheric O_y Calculated by CHASER.

	Global	NH	SH
Sources	5277.4		
Net STE [a]	531.4		
Chemical production	4746.0	2925.2	1820.8
HO_2 + NO	3045.6		
CH_3O_2 + NO	1051.4		
$C_2H_5O_2$ + NO	29.7		
$C_3H_7O_2$ + NO	7.1		
$CH_3COCH_2O_2$ + NO	18.0		
$HOC_2H_4O_2$ + NO	31.4		
$HOC_3H_6O_2$ + NO	8.6		
CH_3COO_2 + NO	206.8		
CH_3COO_2 + HO_2	54.4		
ISO_2 [b] + NO	138.4		
$MACRO_2$ [c] + NO	149.1		
Sinks	−5277.4	−3155.5	− 2121.9
Dry deposition	−898.6	−583.3	−315.3
Chemical loss	−4378.8	−2572.2	−1806.6
$O(^1D)$ + H_2O	−2497.0		
O_3 + HO_2	−1236.4		
O_3 + OH	−558.2		
CH_4 + $O(^1D)$	−1.0		
C_2H_4 + O_3	−4.9		
C_3H_6 + O_3	−3.7		
C_5H_8 + O_3	−38.2		
MACR + O_3	−17.3		
$C_{10}H_{16}$ + O_3	−20.5		
Net chemical production	367.2	353.0	14.2
O_y chemical lifetime (days)	25	24	27
Burden (TgO_3)	323	171	152

Budgets (in TgO_3/yr) are calculated for the region below the tropopause height in the model.
[a]Stratosphere-Troposphere Exchange (net O_3 flux from the stratosphere).
[b]Peroxy radicals from isoprene (C_5H_8) + OH
[c]Peroxy radicals from methacrolein (MACR) + OH

Table 2.10. Net Ozone Production in the Boundary Layers and the Free Troposphere[a]

	Global	NH	SH	Tropics[b]
Free troposphere	357.2	216.3	140.9	171.6
Boundary Layer	10.0	137.1	−127.1	−136.6

Values are calculated in TgO_3/yr.
[a]Vertical regions of the boundary layers are defined as the five lowermost layers in the model (surface to approximately 750 hPa).
[b]15°S to 15°N.

may reduce the O_3 production in polluted areas and hence the global O_3 production. However, this study, including such heterogeneous reactions (section 2.2.1), does not seem to display significant differences in the global ozone budget from the previous CHASER simulation. The ozone chemical production calculated in this simulation, 4746 TgO_3/yr, is on the higher side of the range suggested by many of the previous modeling studies (4550 TgO_3/yr, *Müller and Brasseur* [1995]; 3609 TgO_3/yr, *Lelieveld and van Dorland* [1995]; 3206 TgO_3/yr, *Roelofs and Lelieveld* [1995]; 3415 TgO_3/yr, *Roelofs et al.* [1997]; 4300 TgO_3/yr, *Wang et al.* [1998b]; 3018 TgO_3/yr, *Hauglustaine et al.* [1998]; 4375 TgO_3/yr, *Roelofs and Lelieveld* [2000]). However, much larger ozone production (5258 TgO_3/yr) is estimated by the updated version of the MOZART model [*Horowitz et al.*, 2002]. The global chemical loss of tropospheric ozone is calculated as 4379 TgO_3/yr (59% in the northern hemisphere), contributing for 83% to the total ozone sink (5277 TgO_3/yr). The chemical loss of ozone is mainly by $O(^1D) + H_2O$ (55%), $O_3 + HO_2$ (28%), and $O_3 + OH$ (14%) in the model. The ozone loss by the reactions with NMHCs (as C_2H_4, C_3H_6, isoprene, and terpenes) is important for the ozone budget in the boundary layer over the tropical rain forest (especially in Amazonia and Africa) where biogenic emissions of NMHCs are abundant. Consequently, the calculated net ozone chemical production (difference between the production and the loss) is 367.2 TgO_3/yr (96% in the northern hemisphere). The net ozone production is also highly variable according to individual studies, ranging from 73 TgO_3/yr [*Roelofs and Lelieveld*, 2000] to 550 TgO_3/yr *Müller and Brasseur* [1995]. Although the reason for this variability is unclear, it is attributed partly to the difference in the model domain (i.e., tropopause height) considered for the budget analysis in the models. The net ozone production calculated for the northern hemisphere shows two peaks in late spring (April-May, reaching 500 TgO_3/yr) and late summer (August-September, 400-500 TgO_3/yr). In the southern hemisphere, the calculated net ozone production is positive during the dry season including the biomass burning season (June-October, 100-200 TgO_3/yr). Dry deposition at the surface is also a sink for tropospheric ozone and calculated as 899 TgO_3/yr (65% in the northern hemisphere) by the model, in good agreement with the recent studies (890 TgO_3/yr [*Wang et al.*, 1998b], 898 TgO_3/yr [*Hauglustaine et al.*, 1998], 857 TgO_3/yr [*Horowitz et al.*, 2002]), The net ozone flux associated with the Stratosphere-Troposphere Exchange (STE) is estimated at 531.4 TgO_3/yr in this simulation, contributing for 10% to the total ozone source. This value is in the middle of the range of previous studies (ranging from 391 TgO_3/yr [*Hauglustaine et al.*, 1998] to 846 TgO_3/yr [*Berntsen and Isaksen*, 1997a]) and is relatively close to the simulation of *McLinden et al.* [2000] with their developed Synoz (synthetic ozone) method (475 TgO_3/yr). The tropospheric ozone burden is calculated as 323 TgO_3 (53% in the northern hemisphere). The photochemical lifetime of ozone is estimated at 25 days in the global and annual average. Slightly longer lifetime is found in the southern hemisphere (27 days), reflecting less abundant HO_x concentration in the southern hemisphere (see Section 2.3.3). In both hemispheres, the averaged photochemical lifetime of ozone is about 40 days in winter and about 15 days in summer. The photochemical lifetime of

ozone calculated in the tropical boundary layer is generally in the range of 6-15 days, with showing anomalously short lifetimes of 2-3 days over the tropical rain forests like Amazonia associated with the strong ozone destruction by the reactions with NMHCs.

Table 2.10 shows the calculated net ozone production in the free troposphere and the boundary layers in the model. In the global total, ozone production is much more efficient in the free troposphere, indicating 97% contribution to the total net ozone production. In the northern hemisphere, ozone production within the boundary layer also contributes significantly ($\sim$ 40%), reflecting intense industrial emissions in the midlatitudes. On the contrary, ozone destruction (-127 TgO_3/yr) is calculated in the southern hemispheric boundary layer, canceling the ozone production in the free troposphere (141 TgO_3/yr). The calculated net ozone production in the tropics is much similar to that in the southern hemisphere.

2.3.5 SO_2 and sulfate

In this study, SO_2 oxidation to form sulfate is also simulated by CHASER and is used for the heterogeneous reactions in the model. The model calculates the sulfate formation process using the distributions of H_2O_2, O_3, and OH computed on-line in the chemistry component of CHASER. Figure 2.50 shows the annually averaged distributions of SO_2 and sulfate calculated at the surface. The model calculates high SO_2 mixing ratios ($\sim$10 ppbv) around the industrial regions in the northern midlatitudes (United States, Europe, and eastern Asia). Relatively high SO_2 levels ($\sim$1 ppbv) are also visible in South America and Africa, due partly to biomass burning. In accordance with SO_2, sulfate concentrations are high in the United States, Europe, and China, reaching 5-10 μg m^{-3}.

Figure 2.51 and 2.52 compare seasonal variations observed and calculated at European sites (the EMEP network) for SO_2 and sulfate, respectively. The model generally appears to reproduce the observed SO_2 levels well for most cases. Both the observation and calculation show winter maxima with minima in summer, reflecting the OH seasonality. The model calculation, however, tends to overestimate SO_2 levels in summer by 50-100%. It should be noted here that this study does not account for seasonal variation of residential SO_2 emissions as from stoves, using constant emissions through a year. Inclusion of such seasonal variation of SO_2 emission would reduce surface SO_2 levels in summer. In the case of sulfate, the model generally captures the observed levels, but appears to overestimate the observation in some cases, calculating summer maxima inconsistent with the observation. This model defect may be related to the SO_2 overestimation in summer coming from lack of seasonal variation of residential SO_2 emissions in the model as described above. Additionally, it is also possible that the liquid-phase reactions with H_2O_2 and O_3 are underestimated due in the model to low pH values (i.e., high $[H^+]$ levels) in cloud drops around Europe. Since dissolution of SO_2 into cloud drops and subsequent liquid-phase oxidation by aqueous-phase O_3 are much controlled by the pH values in cloud drops, it is necessary to evaluate further the simulated pH in clouds. Figure 2.53 shows a comparison between the observed and

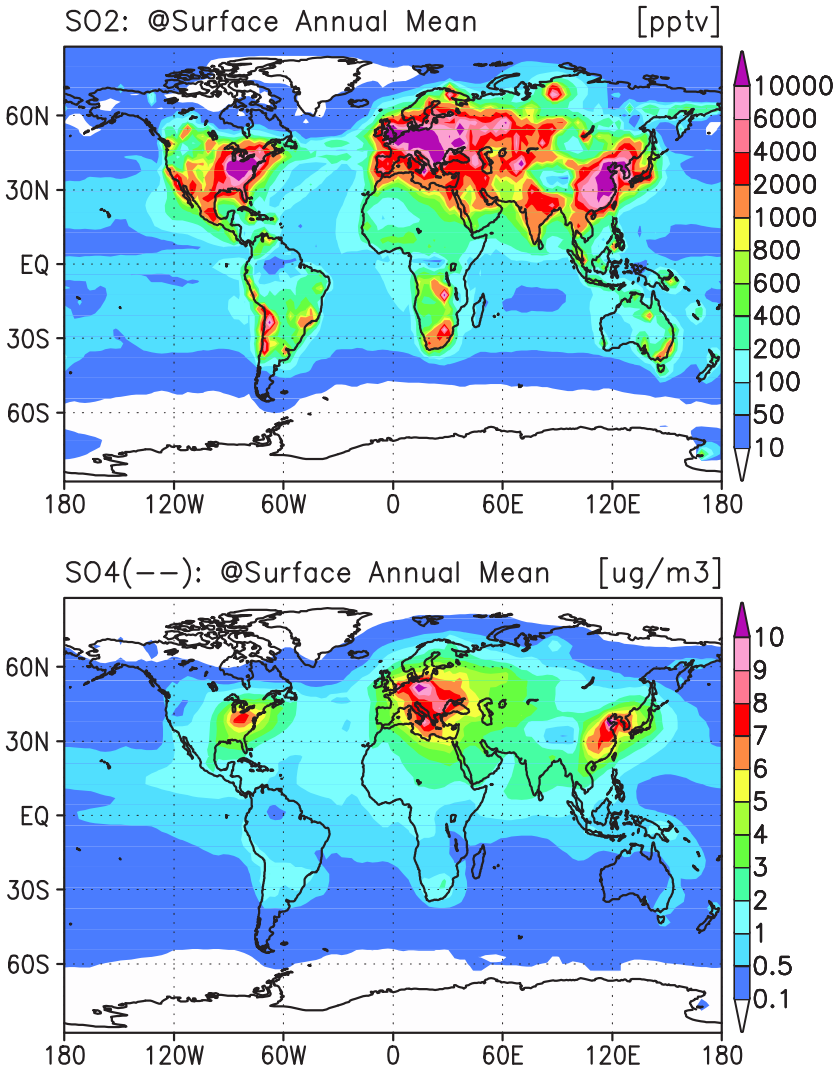

Figure 2.50. SO_2 and sulfate (SO_4^{2-}) distributions calculated at the surface (in annual means).

calculated sulfate mixing ratios for several remote sites. The calculations are well consistent with the observations, reproducing summer sulfate maxima associated with the seasonal variation of SO_2 oxidation with OH and DMS emissions in the remote ocean. However, the model overestimates sulfate levels at Cape Grim (42°S,145°E) by a factor of 2-3 through the year. Since Cape Grim is generally downwind of cities in eastern Australia, this may suggest that the model overestimates SO_2 oxidation and/or underestimates sulfate deposition around the area.

The calculated SO_2 and sulfate vertical distributions are also compared to the NASA GTE observations. Figure 2.54 shows a comparison with the TRACE-P expedition (March-April) as an example. In this Figure, the modeled profiles appear to be consistent with the observation, well simulating the observed increases near the surface due to considerable SO_2 emissions in China.

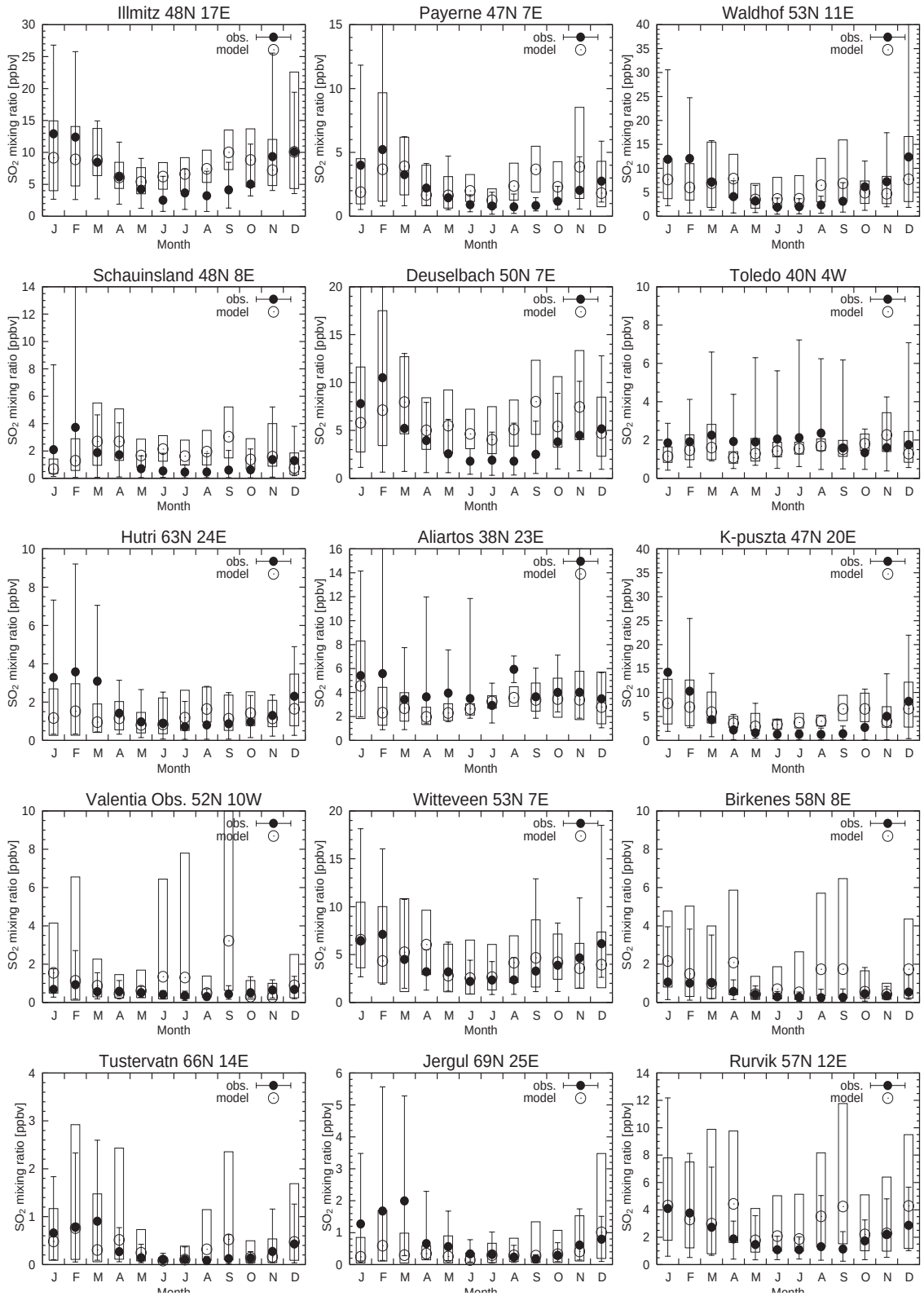

Figure 2.51. SO_2 seasonal variations observed (solid circles) and calculated (open circles) at the surface. Boxes indicate the standard deviations of day-to-day calculations. The ranges of annual variation of the observation (during 1978-1995) are also shown with error bars. The observations are taken from the EMEP network.

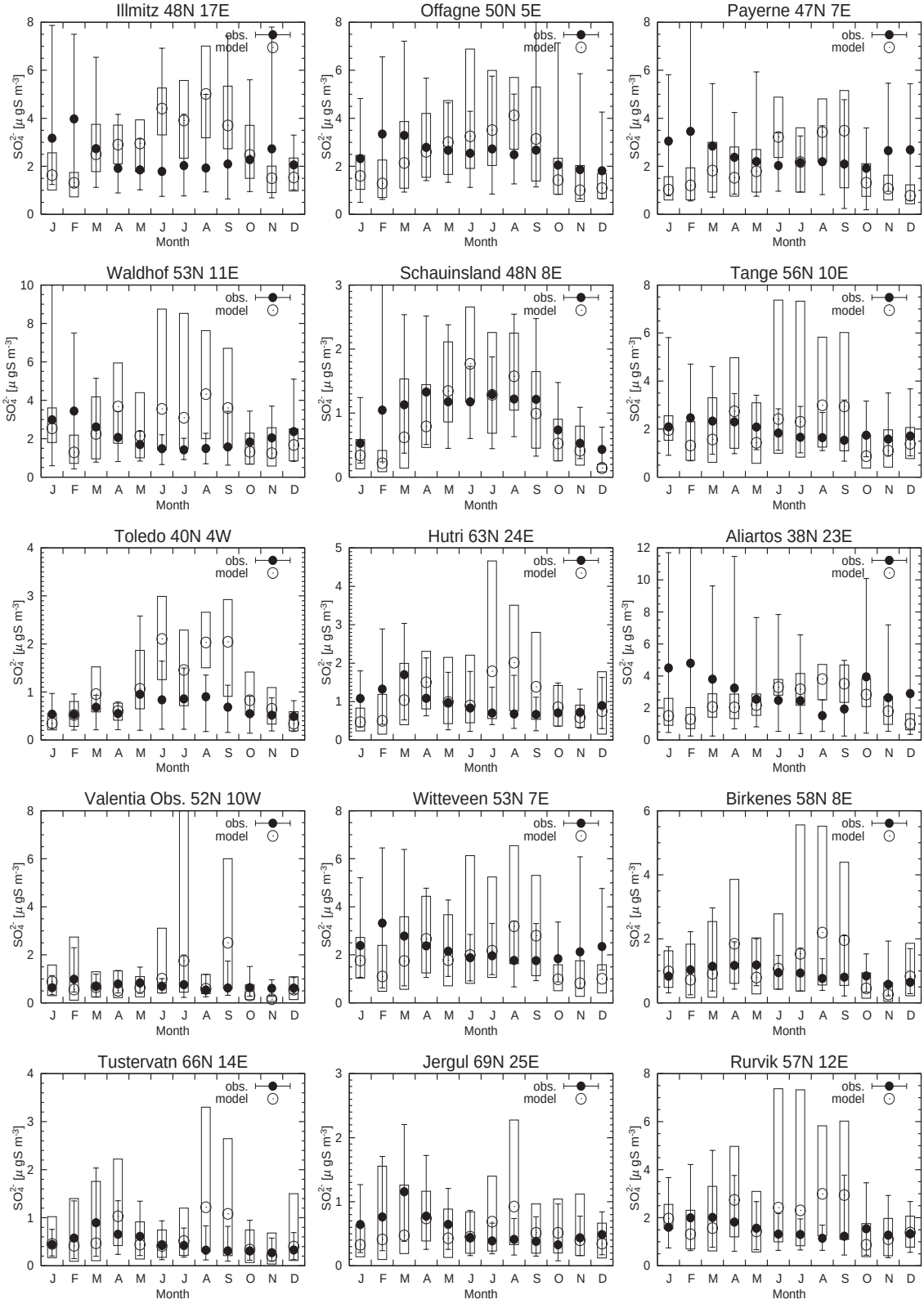

Figure 2.52. Same as Figure 2.51 but for sulfate (SO_4^{2-}).

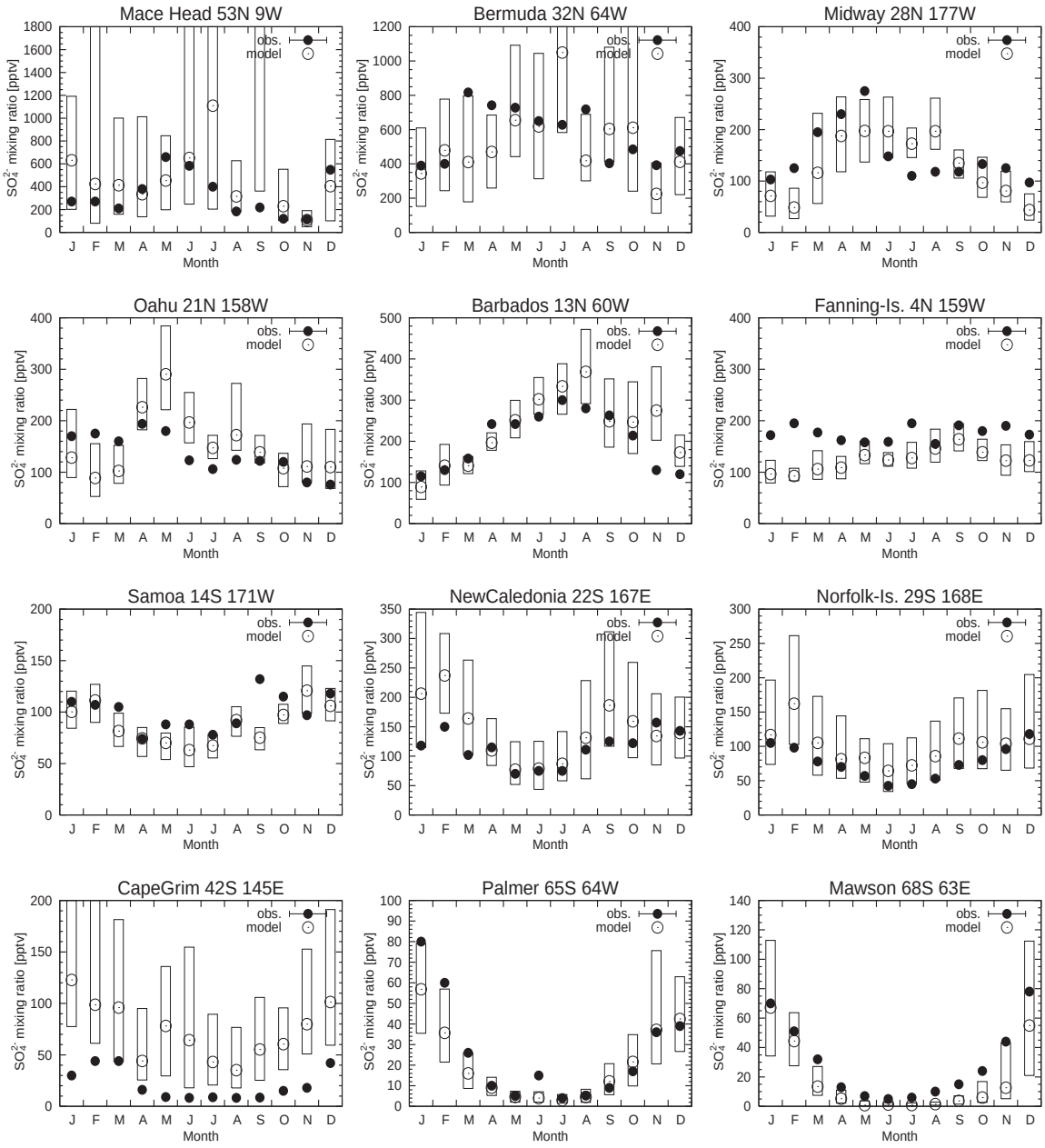

Figure 2.53. Sulfate (SO_4^{2-}) mixing ratios (pptv) observed (solid circles) and calculated (open circles) at several remote locations. Boxes indicate the range of day-to-day calculations.

The model, however, tends to overestimate the upper tropospheric SO_2, possibly implying an underestimation of liquid water content in the upper troposphere over those regions. The same kind of SO_2 overestimation by the model is found in the tropical upper troposphere during PEM-Tropics-B (not shown). The underestimation of sulfate in the free troposphere in the Japan region may suggest inconsistent wet deposition of sulfate (see section 2.2.3 for detailed description of the adopted

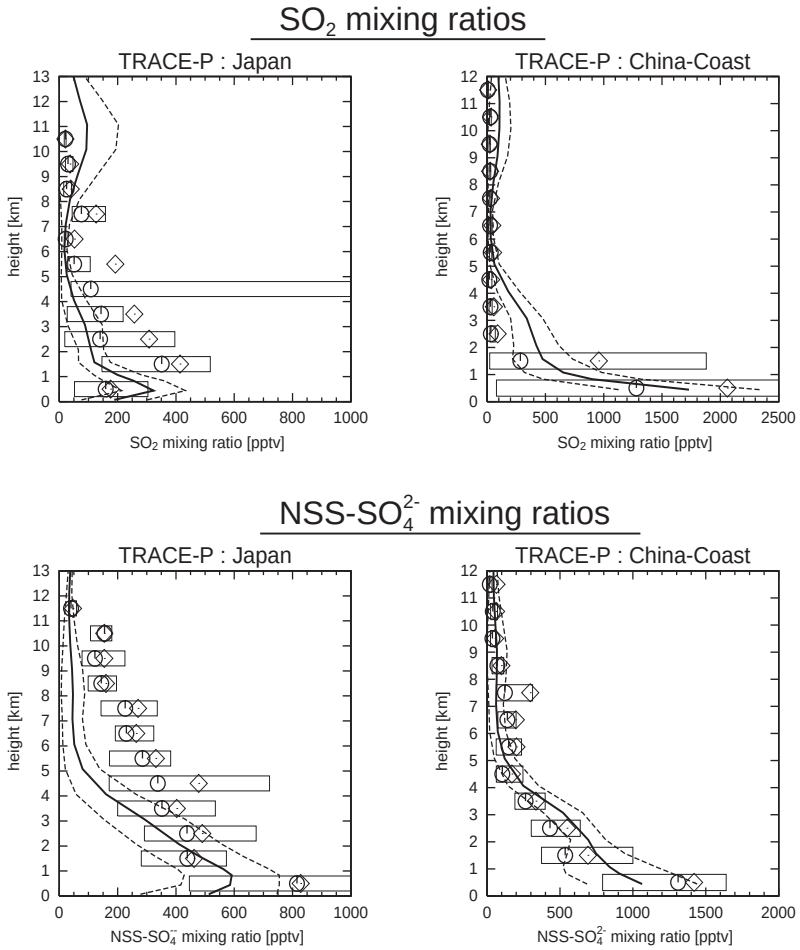

Figure 2.54. SO_2 and SO_4 (sulfate) vertical profiles observed and calculated over the regions of GTE campaigns (listed in Table 2.5). Solid lines and dashed lines show temporal mean and $\pm 1\sigma$ of the model calculation, respectively. The observations show mean (diamonds), median (circles), and inner 50% of the data (boxes).

Table 2.11. Global Budget of Sulfate Aerosol Calculated by CHASER[a]

	Global	NH	SH
Source(chemical prod.)	50.34	40.26	10.08
SO_2 + OH (gas-phase)	14.24	11.94	2.30
$S(IV)$ + O_3 (liq.-phase)	10.80	8.82	1.98
$S(IV)$ + H_2O_2 (liq.-phase)	25.30	19.50	5.80
Sink	−50.52	−40.54	−9.98
Dry deposition	−4.40	−3.53	−0.87
Wet deposition	−46.12	−37.01	−9.11
Burden(TgS)	0.56	0.43	0.13

[a]Budgets are calculated in TgS/yr

deposition scheme and evaluation of sulfate wet deposition flux around Europe).

The global budget of sulfate in this simulation is presented in Table 2.11. About 70% of the total sulfate formation occurs in liquid phase. As the reactions with aqueous-phase O_3 decline with the pH values in cloud drops, the model calculates higher contribution by the reaction with aqueous-phase H_2O_2 (70% of the liquid-phase formation). The model calculates sulfate formation predominantly in the northern hemisphere ($\sim$80%) as a result of intense SO_2 emissions from industry in the northern midlatitudes. The calculated global sulfate formation is balanced mainly with wet deposition (90%), and with dry deposition (10%). Reflecting predominant abundance of sulfate in the northern hemisphere (77% of 0.56 TgS), 80% of the total sulfate wet deposition is calculated in the northern hemisphere, leading to acid rain as illustrated in Figure 2.9. The sulfate budget calculated here are generally consistent with the simulation with the CCSR/NIES aerosol model [*Takemura et al.*, 2000]. This study, however, calculates a larger sulfate formation from the liquid-phase reactions with O_3 and H_2O_2, with a larger (by 10-20%) sulfate burden relative to the simulation of *Takemura et al.* [2000]. This appears to come from the difference in the schemes for liquid-phase oxidation of SO_2 between this work and *Takemura et al.* [2000]. The study of *Takemura et al.* [2000] simulates SO_2 liquid-phase oxidation using the monthly averaged H_2O_2 and O_3 distributions calculated by the previous version of CHASER, whereas this study uses H_2O_2 and O_3 distributions computed on-line in the model.

2.4 Conclusions

This chapter has described and evaluated a global chemical model of the troposphere, named CHASER (CHemical AGCM for Study of atmospheric Environment and Radiative forcing). The CHASER model, developed in the framework of Center for Climate System Research/National Institute for Environment Studies (CCSR/NIES) atmospheric general circulation model (AGCM) [*Numaguti*, 1993; *Numaguti et al.*, 1995], is aimed to study the tropospheric photochemistry and its influences on climate. CHASER is basically driven on-line by climatological meteorology generated by the AGCM to account for interactions between meteorological fields and tropospheric chemistry. The model includes a detailed simulation of tropospheric O_3-HO_x-NO_x-CH_4-CO, NMHCs, and sulfur chemistry calculating the concentrations of 54 chemical species with 139 reactions (gas/liquid phase and heterogeneous) in this study. The sulfate (SO_4^{2-}) formation process is simulated in this study using concentrations of H_2O_2, O_3, and OH computed on-line in the model. Detailed schemes for the dry/wet deposition and emission processes are also implemented in the model. The wet deposition scheme in the previous version of CHASER [*Sudo et al.*, 2002a] has been improved to simulate the deposition process on ice cloud (cirrus) particles and reversible below-cloud scavenging process in this study (section 2.2.3). With the improved wet deposition scheme, the model is capable to simulate the liquid/ice-phase concentrations of individual species dissolved in precipitation. Also, the heterogeneous reactions of N_2O_5 and peroxyradicals (RO_2) (from unsaturated hydrocar-

bons), not considered in the previous CHASER version [*Sudo et al.*, 2002a], are newly included in this study. The model considers emission sources for NO_x (44.3 TgN/yr including lightning NO_x of 5 TgN/yr), CO (1267 TgCO/yr), and NMHCs (including isoprene, 400 TgC/yr and terpenes, 102 TgC/yr). In CHASER, NO_x emissions from lightning are parameterized in the CCSR/AGCM convection, based on *Price and Rind* [1992] and *Price et al.* [1997]. SO_2 and DMS emissions (79.4 and 15 TgS/yr, respectively) are also included for the sulfate simulation in the model. Seasonal variation of biomass burning emissions is simulated using the satellite derived hot-spot data (from ATSR and AVHRR). The sulfate simulation is reflected on-line on the heterogeneous reaction process in the model, but is not coupled with the AGCM radiation component for now. For this study, the T42 horizontal resolution ($\sim 2.8^\circ \times 2.8^\circ$) is chosen with 32 vertical layers from the surface to about 40 km altitude. The basic time step for the dynamical and physical processes in the model is 20 min. The chemistry component (chemical reaction) is evaluated with a constant time step of 10 min in this study.

In the detailed evaluation of the model results (section 2.3), the CHASER calculations show excellent agreement with observations in most cases for important trace gases such as CO, NMHCs, NO_y species, HO_x and related species (formaldehyde, acetone, and peroxides) as well as for ozone. The model computes a CO source of 1514 TgCO/yr from oxidation of methane and NMHCs, larger than the surface emissions (1267 TgCO/yr) considered in this study. The calculated chemical production of CO is most significant in the tropical rainforests, resulting from the NMHCs oxidation process. The model tends to overestimate CO and C_2H_6 in the central Pacific, suggesting too large transport from the United States and the biomass burning regions in South America. The CO and NMHCs distributions observed in the biomass burning related regions (South America, Atlantic, and Africa, during TRACE-A of the NASA GTE) are well reproduced by the model, but appear to be underestimated in the upper troposphere over South America (Brazil) compared also to the previous version of CHASER [*Sudo et al.*, 2002b]. This is attributed probably to the differences in the meteorological fields (particularly convection) generated by the AGCM between this work and the previous [*Sudo et al.*, 2002b]. In the evaluation of the modeled nitrogen species (NO_y), the model appears to simulate well NO_x, HNO_3, and PAN distributions as observed. Simulation of HNO_3 is improved relative to the previous version [*Sudo et al.*, 2002b] with the new wet deposition scheme in this study. The model generally well reproduces the observed PAN distributions, but tends to overestimate middle-upper tropospheric PAN abundances in remote regions as the central Pacific. Though the model in this study includes heterogeneous reactions of unsaturated peroxy radicals (RO_2) which are suggested for a possible cause of PAN overestimation by *Sudo et al.* [2002b], those heterogeneous reactions do not seem to reduce such PAN overestimation in this study. Further investigation, however appears to be needed to check the sensitivity to such heterogeneous RO_2 reactions. In addition, the simplified reaction scheme for NMHCs oxidation adopted in the model must be also evaluated. In this study, the simulated HO_x species ($= OH + HO_2$) are also

evaluated in detail. The model appears to calculate OH and HO_2 distributions much close to the observations during the PEM-Tropics-B and TRACE-P expeditions. The global methane lifetime against the tropospheric OH reaction, an useful measure for OH abundance in the troposphere, is estimated at 9.4 years in this study (the IPCC estimate is 9.6 years). The simulated distributions of important HO_x related species such as formaldehyde, acetone, and peroxides (H_2O_2 and CH_3OOH) are quite consistent with observations. Since peroxides are strongly coupled with HO_x, the agreement between the calculated and the observed peroxides in this study appears to mean successful simulation of HO_x. The ozone distributions simulated in this study are generally in excellent agreement with a number of observations, well capturing the seasonal variation of ozone in both polluted and remote locations. The observed ozone enhancements associated with biomass burning are well simulated by the model. The model, however, tends to overestimate upper tropospheric ozone in the midlatitudes in both hemisphere, which implies overestimation of stratospheric influx of ozone in the midlatitudes. This study also compares the simulated ozone production rates with those derived from observations (Figure 2.49). The model well simulates ozone production as derived from observations, capturing the contrast between the free troposphere and the boundary layer. The calculated global budget of tropospheric ozone shows a chemical production of 4746 TgO_3/yr (with a net production of 367 TgO_3/yr), well within the range suggested by the previous works (3206 TgO_3/yr, *Roelofs and Lelieveld* [1995] to 5258 TgO_3/yr, *Horowitz et al.* [2002]). The simulation shows much more efficient ozone production in the free troposphere, calculating a global net ozone production of 357 TgO_3/yr in the free troposphere with 10 TgO_3/yr in the boundary layer. The estimated net stratospheric O_3 influx is 531.4 TgO_3/yr, consistent with the previous studies (300-800 TgO_3/yr). However, this estimated value (531.4 TgO_3/yr) may be overestimated, since the model in this study tends to overestimate upper tropospheric O_3 in the midlatitudes as described above. Further development of transport scheme is necessary to improve the representation of cross-tropopause transport of ozone in CHASER. In the evaluation of the sulfate simulation by CHASER, the model appears to simulate SO_2 and sulfate distributions generally well, but tends to overestimate surface SO_2 and sulfate levels observed in European sites especially during summer, probably indicating the need of considering seasonal variation of residential SO_2 emissions in the model. The calculated global sulfate burden is 0.56 TgS in this simulation, $\sim$10% larger than the simulation of *Takemura et al.* [2000]. This study also calculates the contribution by sulfate wet deposition to precipitation pH together with nitrates wet deposition (Figure 2.9, page 30). The simulated sulfate and nitrates wet deposition fluxes in Europe show good agreements with the observation from the EMEP network (Figure 2.10 to 2.13). In this study, the model consider oceanic DMS emission in a much simple way ignoring the distributions of planktonic bacteria. DMS oxidation mechanism is also simplified in this study. Future version of CHASER will include detailed reaction mechanism of DMS [e.g., *Lucus and Prinn*, 2002] for a better simulation of sulfate.

As a consequence, this study suggests that the present version of CHASER, newly developed in

this study, is well capable to simulate tropospheric chemistry involving ozone with detailed schemes for chemical and physical processes. Future model development will be focused on improvement of the transport scheme in the model. Also, more detailed aqueous-phase chemistry will be included in future versions of CHASER.

Appendix 2A: Evaluation of transport and deposition processes

Evaluation: Transport process

Transport is one of the most important processes to simulate the atmospheric photochemistry. Emitted or chemically produced species undergo advection by large-scale wind field and subgrid vertical transport by diffusion and moist convection. In CHASER, advective transport is simulated by a 4th order flux-form advection scheme of the monotonic van Leer [*van Leer*, 1977], except for the vicinity of the poles (the flux-form semi-Lagrangian scheme of *Lin and Rood* [1996] is used for a simulation of advection around the poles), with vertical transport associated with moist convection (updrafts and downdrafts) simulated by the cumulus convection scheme in the CCSR/NIES AGCM.

It is necessary to validate the model capability for simulations of transport. For this purpose, we have conducted a simple simulation of the distribution of atmospheric radon (^{222}Rn). Radon is emitted from the earth's surface (mainly from land surface) and decays radioactively with a lifetime of 5.5 days. Surface emission of radon considered here is generally based on *Jacob et al.* [1997]. In *Jacob et al.* [1997], radon emission from land surface is set 1.0 atoms cm^{-2} s^{-1} uniformally. Some simulation studies based on this radon emission scenario, however, show an underestimation of the simulated radon concentrations at Mauna Loa by a factor of 2-3 compared to observations, with showing relatively good agreement of simulations with observations at other sites [*Jacob et al.*, 1997; *Brasseur et al.*, 1998]. Although there is a possibility that an insufficient transport in the simulations causes this discrepancy on one side, it can be attributed to a higher emission rate of radon in eastern Asia as suggested by *Mahowald et al.* [1997]. To take this into account, emission rate in eastern Asia (10°S-55°N, 100°E-160°E) is tentatively increased by a factor of 2 in this simulation.

Figure 2A.1 shows the simulated radon distributions for June-July-August (JJA). As can be seen in zonal mean distribution (upper panel), radon is vertically transported from the surface up to the tropopause height associated with convective activities in the northern hemisphere. Horizontal distribution of radon in the upper troposphere can be seen in the lower panel of Figure 2A.1. Outstanding high concentrations over eastern Asia are due to the doubled emission rate in this region. Transport of radon from northern America and Africa to over the Atlantic is seen. Moreover, long range transport of radon from eastern Asia appears to reach the eastern Pacific region including western America. Figure 2A.2 compares the simulated and the observed radon vertical profiles in western America (California) for June and JJA conditions. The model appears to reproduce the observed radon vertical distribution in the middle-upper troposphere well. The radon maximum